1-1-2010

Molecular Modeling Of Energetic Materials And Chemical Warfare Agents

Nandhini Sokkalingam
Wayne State University

MOLECULAR MODELING OF ENERGETIC MATERIALS AND CHEMICAL WARFARE AGENTS

by

NANDHINI SOKKALINGAM

DISSERTATION

Submitted to the Graduate School

of Wayne State University,

Detroit, Michigan

in partial fulfillment of the requirements

for the degree of

DOCTOR OF PHILOSOPHY

2010

MAJOR: CHEMICAL ENGINEERING

Approved by:

Advisor Date

DEDICATION

To my family

ACKNOWLEDGEMENTS

First, I would like to thank my advisor, Dr.Jeffrey J.Potoff for guiding me through my research. His valuable ideas and assistance helped me learn a great deal during my years as a graduate student. I acknowledge Dr.Charles Manke, Dr. Sando da Rocha and Dr. H. Bernard Schlegel for being a part of my faculty committee. I thank the Department of Chemical and Materials Science Engineering for all the resources and travel funds. I would also like to acknowledge the Wayne State Computing Department for part of the computing time and resources used in this work. I am thankful to the ERDC/CERL for providing the funding during my graduate study. I also thank my fellow labmates who helped me in my research and my friends for their wishes and constant help. Finally, I would like to thank my parents, sister and husband for their motivation and support.

PREFACE

The research presented in this thesis comprises of two different studies, one with energetic materials and the other with chemical warfare agents. The first study involving energetic materials was conducted for the Enviromental Processes Branch of Engineering Research Development Center/Construction Engineering Research Laboratory (ERDC/CERL) under contract number W9132T-06-2-0027. The second study with the chemical warfare agents was conducted for the National Science Foundation (NSF) as part of a research grant.

Table of Contents

List of Tables

List of Figures

Chapter 1

Introduction and Overview

Contamination of military sites including soil and groundwater by energetic materials and chemical warfare agents is a growing problem [1–8]. To avoid health hazards associated with these compounds, it is necessary to remediate the contaminated sites. Effective remediation requires knowledge about environmental fate and impact of the contaminants. While the fate of chemical warfare agents are well studied [6–8], the impact of certain energetic materials in the environment is relatively unknown. So the current focus is determining environmental fate of energetic materials and developing detection and filtration schemes for chemical warfare agents.

In the last few decades, the field of energetic materials witnessed major advancements in terms of development of new energetic materials that cause little or no damage to the people handling it from involuntary triggering of the munitions while maintaining the explosive performance of their predecessors [9]. The enormous volume of damages inflicted upon both personnel and equipment by unintended detonation of munitions for several years motivated this development. As a result, munitions called as Low Vulnerability Ammunitions (LOVA) or Insensitive Munitions (IM) that possessed excellent mechanical properties to resist external damage such as low shock sensitivity and high thermal stability emerged [10]. Concurrent with the development of IM compounds, a growing emphasis has been placed on "green" munitions, i.e. energetic materials with significantly reduced potential for environmental damage. Explosives such as trinitrotoluene (TNT), cyclotrimethylenetrinitramine (RDX) and sym-cyclotetramethylene-tetramitramine (HMX) have been found in groundwater and soil due to their extensive usage and costs of remediation are estimated in the

billions of dollars [11]. It is hoped that new energetic materials may be developed with low toxicity and persistence, thereby minimizing risks to public health and reducing or eliminating the need for costly remediation.

The fate of an energetic material in soil, water or atmosphere can be determined by studying the interaction between the compound and the target medium. These interactions are described in part by partitioning of the compound of interest between two different mediums which is represented by various partition or the distribution coefficients. Two key partition coefficients used to assess a compound's impact in air, water and organic mediums are octanol-water partition coefficients ($\log K_{ow}$) and Henry's law constants ($\log H$). For dilute aqueous solutions, the Henry's law constant is the ratio of the solute's partial pressure and its aqueous concentration. The octanol-water partition coefficient is the ratio of the concentration of a neutral chemical species in octanol and in water at equilibrium and is a measure of hydrophobicity/lipophilicity or hydrophilicity of a compound. It is also related to bioaccumulation and bioavailability and has been a key parameter in drug design for decades [12, 13].

Given the importance of $\log K_{ow}$ and $\log H$ as predictors of activity in biological and environmental sciences, numerous experimental [12] and theoretical methods exist for predicting them. The need for synthesis of each compound of interest so that its physicochemical properties may be measured by experiment is time consuming and costly. Most of the theoretical methods available for predicting partition coefficients are based on fragment/group or bond contribution methodology [14–21]. Other methods include Quantitative Structure-Activity Relationship (QSAR) and Quantitative Structure-Property Relationship (QSPR) models [22–28], which relate molecular structures to biological activ-

ity (QSAR), or a particular physical property (QSPR). These activities or properties are expressed as a function of the partition coefficients. QSAR/QSPR use molecular descriptors (topological, topographical and quantum chemical) derived from a training set of compounds. Training sets may contain anywhere from a few hundred to tens of thousands of molecules and in general, the larger the training set, the better the predictive capability.

Overall, most QSPR do an excellent job of predicting physical properties for molecules with similar molecular structure as those in the training set. However, for molecules that differ significantly from those used in the optimization of the QSPR, which includes most energetic materials, there is a concern that the predictions of QSPR may not be representative of experimental data [29, 30]. Other theoretical methods that offer promise are continuum solvent methods such as COSMO, SM (Solvation Model), GB/SA (Generalized Born/Surface Area) models [31–36] and molecular modeling or simulation methods coupled with Free Energy Perturbation (FEP) [37, 38]. Continuum solvent methods have a few drawbacks over molecular simulation which are illustrated by Jorgensen *et al.* [39]. So, molecular simulation emerges as the most accurate theoretical method to predict physicochemical properties for energetic materials of interest.

Nerve agents are a certain group of toxic chemical warfare agents that are organophosphates. Exposure to large amounts of nerve agent results in death within 10 to 15 minutes. Nerve agents act by disrupting the nervous system [40]. They rapidly react with a serine hydroxyl group in the active site of acetylcholinesterase (AChE), an enzyme that relaxes the activity of the neurotransmitter, acetylcholine, and form a phosphate or phosphonate ester [40]. The resulting phosphylated enzyme regenerates very slowly, making the enzyme inaccessible for acetylcholine [41]. The chiralty around the phosphorous atom also has an

impact in determining the extent of toxicity of the nerve agent [41, 42]. Due to the acute and chronic toxicity of nerve agents and the increased threat of chemical weapon attack by terrorist groups, there has been considerable focus in the development of detection schemes for the nerve agents.

Promising technologies of detection include, molecularly imprinted polymers [43, 44] or polymer composites [45], electrochemical bio-sensors [46] and metal oxide thin films and nanowires [47–51]. In addition to sensing applications, metals [52] and metal oxides [53–56] have been studied extensively as potential catalysts for the decomposition of chemical agents into non-toxic substances. Although metal oxide based sensors exhibit high sensitivity, they suffer from poor selectivity, leading to false positives triggered by relatively innocuous materials, such as methanol. Prefiltering and concentration schemes involving physical adsorption on nanoporous silica and carbon pores have been proposed as a means of improving detection selectivity for chemical warfare agents [57–59]. While the chemical adsorption of organophosphates on metals and metal oxides is known to occur through a common mechanism of oxygen binding to the surface, much less is known about specific substrate-adsorbate interactions during physical adsorption.

Carbon related adsorbents are promising candidates to accomplish separations in terms of framework, stability and efficiency. Carbon adsorbents represent a major class of adsorbents that range from simple graphitic pores to carbon nanotubes. The selectivity of each class of adsorbents depends on the nature of solid-fluid and fluid-fluid interactions, structure of the pore and system conditions such as temperature and pressure. The adsorption behavior of the nerve agents in carbon substrates have to be determined as a preliminary step to the sensing process. Molecular modeling is well suited for studying chemical warfare

agents due to the hazardous nature of these compounds.

The research presented in this thesis is an effort to use molecular simulation as a theoretical tool to address the environmental issues emerging from energetic materials and nerve agents. The field of molecular simulation has seen rapid growth due to advances in computer hardware resources. Given only a molecular structure, atomistic computer simulations may be used to calculate nearly any physical property associated with that molecule. After a series of advancements in algorithms [60–65], simulations have been used extensively for the prediction of various thermophysical properties. In this era of supercomputing, many complex materials and processes may be simulated in less time with high precision and accuracy across a parallel platform of multiple processors. Also, simulations offer valuable molecular-level insights into the nature of specific interactions and help in better understanding the chemical systems and processes.

The key to accurate predictions of thermophysical properties is the force field or molecular model. A force field is a set of parameters used to represent the intramolecular and intermolecular interactions. In this research, force fields have been developed for two class of compounds: energetic materials and nerve agents to predict various thermophysical properties. For energetic materials, atomistic molecular dynamics simulations are used to predict physical properties with the developed force fields that may be used to predict the environmental fate of these compounds. In this context, octanol-water partition coefficients and Henry's law constants are determined. Besides partition coefficients, critical parameters, vapor pressure, boiling point, acentric factor, heats of vaporization, lattice parameters, crystal density and melting point are also predicted. For nerve agents, the developed forcefields are used to determine their vapor-liquid coexistence curves, vapor

pressures, critical points, heats of vaporization and second virial coefficients through atomistic Monte Carlo simulations. In addition to the bulk condensed phase properties, pure and water-organophosphate mixture isotherms over carbon slit pore were determined using atomistic Monte Carlo simulations.

1.1 Research Outline

This dissertation presents research that involves predicting thermophysical properties of some hazardous chemicals such as explosives and chemical warfare agents through atomistic molecular simulation by building new molecular force fields. The thermophysical properties of interest are partition coefficients, boiling points, critical points, vapor pressure, vapor-liquid equilibria, crystal density, lattice parameters, melting point and adsorption isotherms.

In Chapter 2, all the existing force fields and the methodology for building the new force field are discussed. The potentials for non-bonded and bonded interactions are presented. Non-bonded interactions include the Lennard-Jones and the coulombic contribution while the bonded interactions include bond stretching, bond angle bending and torsional potentials.

In Chapter 3, description of simulation methods employed in this research are presented. The statistical thermodynamics background associated with each method is also discussed.

In Chapter 4, *ab initio* studies conducted on the energetic materials are presented. Impact sensitivity correlations, equilibrium structures and calculation of rotational barriers are presented.

In Chapter 5, newly developed force fields for energetic materials are presented. Also, the computational methodologies and simulation details for prediction of condensed phase properties such as partition coefficients, vapor-liquid equilibria, vapor pressure, critical

points, boiling points are discussed. This chapter ends with a results and discussion section, where the predicted thermophysical properties are presented.

In Chapter 6, force fields and calculations for predicting solid phase properties of energetic materials of interest such as lattice parameters, crystal density and melting point are presented. Also, different melting point methods used for predicting melting points are also discussed. The predicted solid phase properties are used to validate the developed force fields.

In Chapter 7, force fields developed for the nerve agents are presented followed by a description of the simulation methodologies. The predicted boiling points, critical points, heats of vaporization, vapor pressure, vapor liquid equilibria and adsorption isotherms are presented.

In Chapter 8, the conclusion for the dissertation is presented followed by future work associated with this research.

Chapter 2

Force Field Development

2.1 Introduction

The accuracy of molecular simulation is dependent entirely on the force fields used to describe the interactions of atoms with each other. Force fields can be conveniently split into two types of interactions: bonded and non-bonded. Bonded interactions account for the conformational structure of the molecule and include bond stretching, bond bending and torsion around the various bonds. Non-bonded interactions describe the energetics of atom-atom interactions and are described by an atom-atom pair interaction potential. Because of the importance of force fields, numerous generalized force field development efforts were undertaken. These include OPLS [66–75], AMBER [76–78], CHARMM [79–83] and Gromacs [84] in the biological sciences and OPPE [85] and TraPPE (Transferable Potentials for Phase Equilibria) [86–96, 98] in engineering and physical sciences.

While each of the aforementioned force fields is based on the idea of "transferable" potential parameters, i.e., parameters for atoms or functional groups that are independent of bonding environment, the philosophies of parametrization differ. Force fields in the biological sciences are typically fit to reproduce properties of the condensed phase at room temperature, such as heat of vaporization and liquid density and may also be fit to reproduce *ab initio* derived potential energy surfaces of the target molecule with various probe atoms [110]. The parameters for force fields developed for the prediction of phase behavior and other physical properties, on the other hand, are optimized to reproduce pure component, and sometimes mixture [97, 98] vapor-liquid equilibria over the entire phase diagram

from the boiling to critical point. The result is improved predictive capability with respect to physical properties and phase behavior when used in mixture calculations [97–99]. In this work, force fields are developed for energetic materials and warfare agents based on the TraPPE force field.

2.2 Model

In the TraPPE force field, the overall energy of the system is given by a collection of pair-wise additive potentials summed over all interaction sites of all molecules in the system

$$U = \sum_{i=1}^{nmolec} \sum_{j}^{nsite} U_{ij} \tag{2.1}$$

This energy can be further decomposed into inter- and intra-molecular interactions

$$U = U_{intra} + U_{inter} \tag{2.2}$$

The quantities U_{intra} and U_{inter} are commonly referred to as bonded and non-bonded interactions, respectively.

2.2.1 Bonded

Bonded interactions included bond vibrations, angle bending and rotation around dihedral angles. For small molecules, it is possible to achieve accurate results by neglecting vibrational modes and treating the entire molecule as a single rigid body. However, for larger molecules, or those where the vibrational modes are not as constrained, it is important to model vibrational degrees of freedom so that phase space is sampled correctly during the simulation. Bond stretching and bond angle bending are both controlled by a harmonic

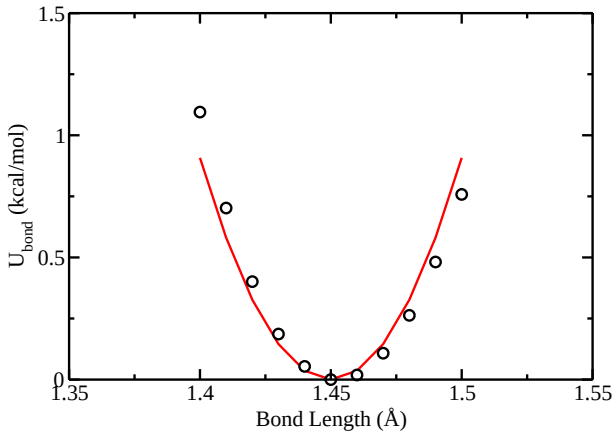

Figure 2.1: *Ab initio* prediction of barriers to N-C bond stretching in DNAN. Symbols correspond to HF/6-31+g(d,p) calculations while line is a fit of harmonic potentials to the *ab initio* data.

potential. The bond stretching potential is

$$U_{bond} = \frac{k_b}{2}(r - r_0)^2 \tag{2.3}$$

where r is the measured bond length, r_0 is the equilibrium bond length and k_b is the force constant. Bond angle bending potential is given by

$$U_{bend} = \frac{k_\theta}{2}(\theta - \theta_0)^2 \tag{2.4}$$

where θ is the measured bond angle, θ_0 is the equilibrium bond angle and k_θ is the force constant. Representative *ab initio* data used for the parametrization of bond stretching and bending constants for the NO_2 group are shown in Figure 2.1 and Figure 2.2 for N-C bond stretching and bond angle bending for O-N-O in the energetic material, 2,4-dinitroanisole (DNAN).

Interactions between atoms that are three bond lengths apart are governed through a

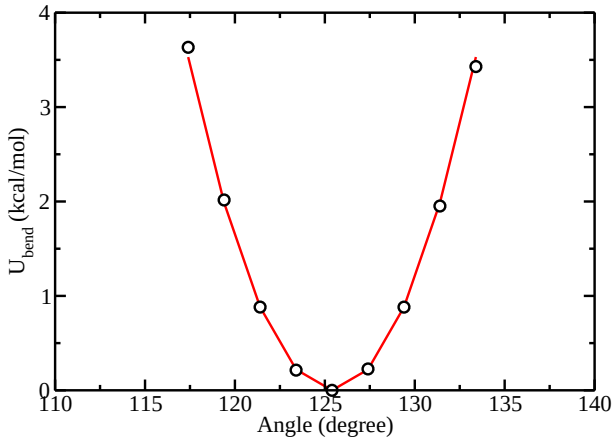

Figure 2.2: *Ab initio* prediction of barriers to O-N-O bond bending in DNAN. Symbols correspond to HF/6-31+g(d,p) calculations while line is a fit of harmonic potentials to the *ab initio* data.

torsional potential in the form of a cosine series

$$U_{tors} = \Sigma k_{\phi}[1 + cos(n\phi - f)] \tag{2.5}$$

where ϕ is the dihedral angle, n is the multiplicity, f is the phase angle and k_{ϕ} is the force constant. The inclusion of a phase angle is required in cases where barriers to dihedral rotation are not symmetric around 180°. Representative data are presented for barriers to dihedral rotation about the C-N bond connecting the -NO_2 group to the aromatic ring in DNAN in Figure 2.3.

Equilibrium bond lengths and angles were determined from ab initio HF/6-31g+(d,p) calculations. All the force constants were determined by running relaxed potential energy scans in Gaussian at the same level of theory and basis set and fitting to the scan data, the corresponding potential for vibration, angle bending and torsion. The scans were relaxed in nature: fixing the dihedral angle of interest in the optimized structure at each level of theory and reoptimizing all other internal coordinates at the same level of theory to minimize the

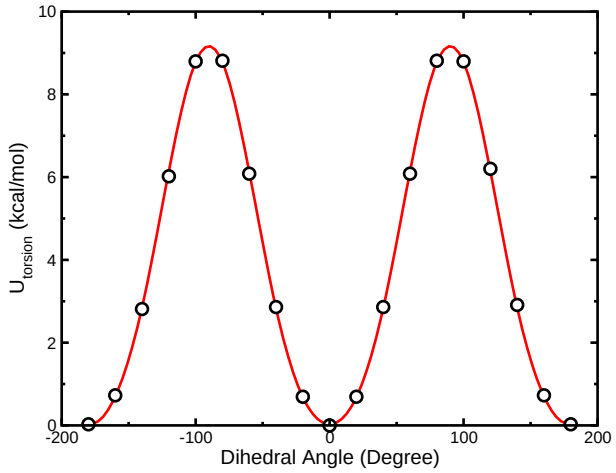

Figure 2.3: *Ab initio* prediction of barriers to dihedral rotation about the C-N bond (para position) in DNAN. Symbols correspond to HF/6-31+g(d,p) calculations while line is a fit of the cosine series to the *ab initio* data.

total energy.

2.2.2 Non-Bonded

Non-bonded interactions between atoms in each molecule are represented with a standard 12-6 Lennard-Jones potential with a coulombic term for partial charges.

$$U(r_{ij}) = 4\varepsilon_{ij}\left[\left(\frac{\sigma_{ij}}{r_{ij}}\right)^{12} - \left(\frac{\sigma_{ij}}{r_{ij}}\right)^{6}\right] + \frac{q_i q_j}{4\pi\varepsilon_0 r_{ij}} \tag{2.6}$$

where r_{ij}, ε_{ij}, σ_{ij}, q_i, and q_j are the separation, LJ well depth, pseudo-atom diameter and partial charges, respectively, for the pair of interaction sites i and j and ε_0 is the permittivity of vacuum. This approach treats all interactions as effective interactions, i.e., the Lennard-Jones r^{-6} term implicitly includes many-body dispersive interactions and the additional contributions arising from instantaneous dipole-quadrupole r^{-8} and quadrupole-quadrupole r^{-10} interactions. In a similar way, the partial charges mimic both the first-order electrostatic and second-order induction forces. Therfore it is not possible to accurately determine,

for example, σ_{ii} from experimentally determined atom diameters and instead, the parameters ϵ_{ii}, σ_{ii} and q_i in this equation are derived from a combination of quantum chemical calculations, and empirical fitting to experimental data. The cross interaction parameters for unlike atoms were determined through Lorentz-Berthelot combining rules [100, 101].

$$\sigma_{ij} = (\sigma_{ii} + \sigma_{jj})/2 \tag{2.7}$$

$$\varepsilon_{ij} = \sqrt{\varepsilon_{ii}\varepsilon_{jj}} \tag{2.8}$$

Determination of Partial Charges

The determination of partial charges is complicated by the fact that they are not a quantum mechanical observable, hence the values of the partial charges derived from quantum chemical data are highly dependent on the modeling scheme, and to a lesser extent the choice of quantum mechanical (QM) theory and basis set. Some of the more common schemes for extracting partial charges from QM data are Mulliken [102] and natural population analysis [103]. However, partial charges derived from Mulliken analysis have been shown to depend strongly on basis set [104]. An alternative scheme for determining partial charges used in this work, and in the development of other force fields, such as CHARMM and AMBER, is to calculate partial charges by fitting to reproduce electrostatic potential energy surfaces (ESP), which are observable directly from quantum mechanics. There are a number of schemes for doing this, including Merz-Kollman [105], CHELP [106], CHELPG [107] and PQDP [108].

In this work, partial charges were determined using the CHELPG (Charges from Electrostatic Potentials using a Grid based method) methodology in Gaussian [109]. The partial

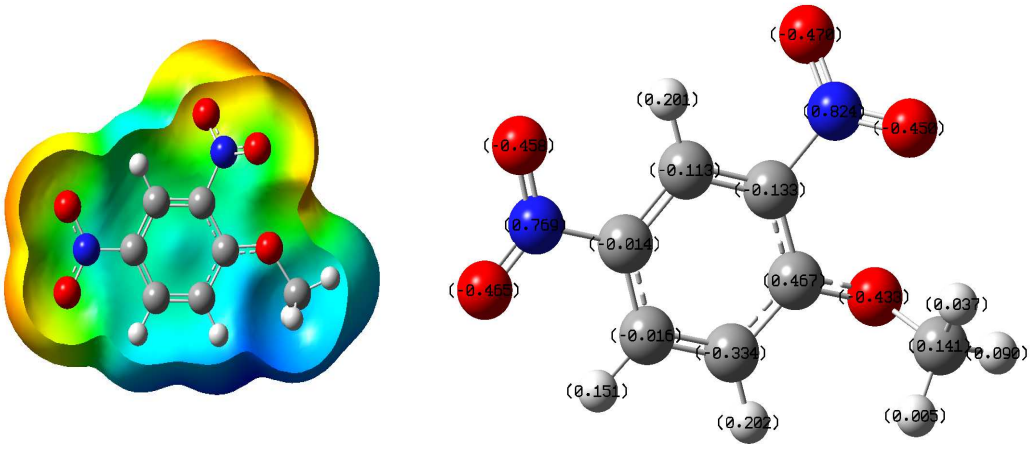

Figure 2.4: Electrostatic potential energy surface for DNAN from CHELPG scheme (left); Structure of DNAN with the charges on each atom site (right).

charges from CHELPG scheme were tuned whenever necessary to reproduce certain thermophysical properties. A schematic of the electrostatic potential surface generated from gaussian using CHELPG methodology is presented in Figure 2.4. Structures for the compounds of interest were optimized using Hartree-Fock theory and the 6-31+(d,p) basis set. Geometry optimizations were performed from multiple initial configurations to confirm the optimized structure was the true lowest energy state. The combination of Hartree-Fock theory and 6-31+g(d,p) basis set were chosen based on past work by our group and others, which show that this relatively low level calculation provides the best estimate of partial charges for use with the empirical potential models of interest here [110, 111]. The electrostatic potential energy surfaces (ESP) were determined for the optimized structures and partial charges determined by fitting to reproduce the ESP.

Determination of Lennard-Jones Parameters

The TraPPE force field was developed for high accuracy predictions of vapor-liquid coexistence of complex multi-component mixtures. Typically, Lennard-Jones parameters are optimized to reproduce experimental vapor-liquid coexistence curves to within 1% of

experimental data. New molecules are parametrized in a stepwise fashion in an effort to minimize the total number of parameters and constrain the optimization effort so that only one new parameter is being optimized at a time. For example, the TraPPE United-Atom force field for normal alkanes uses four unique parameters to describe the entire alkane homologous series. These are the Lennard-Jones ϵ and σ for the CH_2 and CH_3 groups. Parameters for the CH_3 group were optimized from the simulations of ethane. The CH_2 parameters were optimized from simulations of n-hexane, using the CH_3 group parameters previously optimized in simulations of ethane. This same CH_3 group was later used in the development of force fields for ketones, aldehydes, ethers, alcohols and nitro compounds, demonstrating perhaps the most important facet of force field parametrization: transferability. The idea of transferable force field parameters is at the heart of the methodology used in this work. In essence, parameters for various functional groups are said to be independent of bonding environment, allowing for the construction of new molecules from a library of existing parameters. Using the idea of transferability, a molecule was split into funtional groups and the parameters for each of them were taken from similar groups of other compounds for which TraPPE force field has already been developed.

Chapter 3

Computer Simulation and Statistical Thermodynamics

3.1 Introduction

Computer simulation yields information about the microscopic properties and statistical mechanics is required to translate those into macroscopic terms. An experimentally observable macroscopic property is given by [112],

$$A_{obs} =< A >_{ens} \tag{3.1}$$

where $< A >_{ens}$ is the ensemble average of A. The ensemble average is obtained by calculating A in every possible state of the system and taking a weighted average of A from all possible states. Four types of ensembles that are commonly used are: the microcanonical (NVE), canonical (constant NVT), the isothermal-isobaric (constant NPT), the grand canonical ensemble (constant μVT). Simulations can be classified into two types : Monte Carlo (MC) and molecular dynamics simulation (MD). While Monte carlo scheme calculates the static properties of a system, molecular dynamics computes both the static and the dynamic or time dependent properties. In the following sections, details of different MC and MD techniques relevant to this work are presented.

3.2 Simulation Techniques

In this section, various simulation techniques used in this research and the statistical mechanics behind each technique is discussed in detail. The octanol-water partition coef-

ficients and the Henry's law constants of the energetic materials were determined by Free Energy Perturbation (FEP) technique using NPT ensemble molecular dynamics method. The vapor-liquid equilibria of EM compounds were simulated with Gibbs-Duhem Integration while Grand Canonical Histogram Reweighting Monte Carlo (GCHRMC) technique was used for chemical warfare agents. The solid phase properties of energetic materials were simulated using NPT MD method. Finally, the adsorption of CWAs in carbon slit pores were modeled using Grand Canonical Monte Carlo (GCMC) and Gibbs Ensemble Monte Carlo (GEMC) methods. All the Monte Carlo methods used a coupled-decoupled configurational-bias Monte Carlo (CBMC) technique [113] for insertion of molecules into a dense phase.

3.2.1 Free Energy Calculations

Free energy is critical in calculating the partition coefficients. Free energy calculations via molecular simulation can be performed by three different methods [37, 38]: free energy perturbation [114], thermodynamic integration [115] and slow growth [116]. Each method differs in how the free energy change is calculated. In the first method, free energy difference between two states a and b is represented by,

$$\Delta A = -k_b T ln < e^{-\Delta \hat{H}/RT} >_a \tag{3.2}$$

where $\Delta H = \hat{H}_b - \hat{H}_a$, ΔA is the Helmholtz free energy and $<>_a$ is the ensemble average over a system at state a. If the difference between the initial and final states is large, accurate ensemble average can be calculated using a multistep perturbation simulation. In a mutistep simulation, transformation between states a and b is performed in several intermediate steps involving non-physical states along a pathway that connects a to b. This

pathway is represented by a variable called "coupling parameter" λ, that makes the free energy a continuous function of it between the initial and the final states. The hybrid Hamiltonian of the system as a function of the coupling parameter λ is represented as,

$$\hat{H}(\lambda) = \lambda \hat{H}_b + (1 - \lambda)\hat{H}_a \tag{3.3}$$

where $\hat{H}_a$ and $\hat{H}_b$ are Hamiltonian of initial and final states respectively. λ varies from 0 ($\hat{H} = \hat{H}_a$) to 1 ($\hat{H} = \hat{H}_b$). In the thermodynamic integration method, the free energy difference between two system a and b is represented by,

$$\Delta A = \int_{\lambda=0}^{\lambda=1} < \frac{\partial \hat{H}}{\partial \lambda} >_\lambda d\lambda \tag{3.4}$$

The ensemble average of the derivative of the Hamiltonian wih respect to λ is computed at different values of λ followed by numerical integration to obtain the free energy difference. In the last method which is the slow growth technique, the Hamiltonian is changed by an infinitesimal amount over each λ value resulting in the following equation,

$$\Delta A = \sum_{\lambda=0}^{\lambda=1} (\hat{H}_{\lambda+1} - \hat{H}_\lambda) \tag{3.5}$$

where $\hat{H}_\lambda$ is the Hamiltonian for a given λ and $\hat{H}_{\lambda+1}$ is the Hamiltonian for the next larger λ. This equation is a result of an assumption that free energy difference is small and so $\partial \hat{H}/\partial \lambda = \Delta \hat{H}/\Delta \lambda$. The free energy perturbation is discussed in detail in the following section.

Free Energy Perturbation

The fundamental equation for calculating the free energy difference between two different states by FEP is given by,

$$\Delta A_{a\rightarrow b} = -k_b T \ln < exp[-\frac{\hat{H}_b(r,p) - \hat{H}_a(r,p)}{k_b T}] >_a \tag{3.6}$$

where k_b is the Boltzmann constant, T is the temperature and $\hat{H}_a(r,p)$ and $\hat{H}_b(r,p)$ are the Hamiltionians which describes the interactions between particles in states a and b in terms of coordinates r and conjugate momenta p of the particles. The modified form of the free energy difference equation with the coupling parameter incorporated is given by,

$$\Delta A_{a\rightarrow b} = -k_B T \sum_{k=1}^{N} \ln < exp[-\frac{\hat{H}_b(r,p;\lambda_{k+1}) - \hat{H}_a(r,p;\lambda_k)}{k_B T}] >_k \tag{3.7}$$

where N is the number of intermediate states between a and b. Ensembles in free energy perturbation technique can be generated using either MC or MD simulation. In this research, MD simulation will be used for FEP calculations where the ensemble average is the time average of exp(-$\Delta\hat{H}/k_bT$) where,

$$\Delta\hat{H} = \hat{H}_b - \hat{H}_a \tag{3.8}$$

There are two different approaches to perform a free energy perturbation calculation in terms of the molecular topology: single and the dual topology. In the single topology method, the molecular topology of just one state (either a or b) is used and transformed to another during the course of the simulation. In contrast, the double topology paradigm

uses two independent topologies each for the initial and the final state simultaneously. In this kind of topology, three groups of atoms exist: atoms describing the initial state a of the system, atoms describing the final state b and those atoms that do not change during the simulation which is the environment. The atoms that correspond to initial state a do not interact with atoms that belong to the final state b throughout the entire simulation.

3.2.2 Gibbs Duhem Integration

Gibbs-Duhem integration [62] was used to determine the vapor-liquid coexistence curves and the vapor pressures for the energetic materials. With the knowledge of an initial coexistence point, the Clapeyron equation can be integrated to provide an estimate of coexistence points at other temperatures. The Clapeyron equation is given by,

$$\left[\frac{d\ln P}{d\beta}\right]_{\sigma} = -\frac{\Delta h}{\beta P \Delta \nu} \tag{3.9}$$

where P is the pressure, $\beta = 1/kT$, Δh is the difference in molar enthalpies of the coexisting phases, Δv is the difference in molar volumes and σ indicates that the derivative is taken along the saturation line. The method allows for the prediction of the saturation pressure at a temperature ΔT away from the known coexistence point as well. The first coexistence simulation was carried out by integrating the Clapeyron equation with trapezoidal rule predictor-corrector method, followed by two simulations with mid-point predictor-corrector method. All subsequent simulations used the higher order Adams predictor-corrector integration scheme which produced accurate results. The following equations represent the predictor-corrector methods.

Trapezoid :

$$y_{i+1} = y_i + hf_i \tag{3.10}$$

$$y_{i+1} = y_i + \frac{h}{2}(f_{i+1} + f_i) \tag{3.11}$$

Midpoint :

$$y_{i+1} = y_{i-1} + 2hf_i \tag{3.12}$$

$$y_{i+1} = y_{i-1} + \frac{h}{3}(f_{i+1} + 4f_i + f_{i-1}) \tag{3.13}$$

Adams :

$$y_{i+1} = y_i + \frac{h}{24}(55f_i - 59f_{i-1} + 37f_{i-2} - 9f_{i-3}) \tag{3.14}$$

$$y_{i+1} = y_i + \frac{h}{24}(9f_{i+1} + 19f_i - 5f_{i-1} + f_{i-2}) \tag{3.15}$$

where y is $\ln P$, h is the difference in reciprocal temperature β, f is the integrand ($d\ln P/d\beta$) and subscript $i+1$ refers to the current simulation. The first equation in each method refers to the predictor formula and the second one is the corrector formula. The pressure is specified using the predictor formula,

$$P = P_0 \exp[f_0 h] \tag{3.16}$$

where P_0 is the initial pressure and f_0 corresponds to the initial coexistence data. This pressure is then updated using the corrector formula after a simultaneous liquid and gas simulation at P_0

$$P = P_0 \exp[h(f_0 + f_1)/2] \tag{3.17}$$

where f_1 is the estimate from the simulation in progress and it continues with the new pressure.

3.2.3 Grand Canonical Monte Carlo-Histrogram Reweighting

Grand Canonical Histogram Reweighting Monte Carlo (GCHRMC) method was used to determine phase coexistence properties of the chemical warfare agents. In GCMC, the system is coupled to a reservoir and the chemical potential, temperature and the volume are fixed and the number of particles allowed to fluctuate. Equilibrium is reached when the chemical potential and temperature of the system and reservoir are equal. In the histogram reweighting technique, multiple histograms containing the number of particles and the energy are collected. The probability of observing a configuration with given number of particles and configuration energy E is

$$P(N,E) = \Omega(N,V,E)\exp(\beta\mu N)\exp(-\beta E)/\Xi(\mu,V,T) \tag{3.18}$$

where $\Omega(N,V,E)$, is the microcanonical density of states, μ is the chemical potential, $\beta = 1/k_bT$ and $\Xi(\mu,V,T)$ is the grand canonical partition function given by

$$\Xi(\mu,V,T) = \sum_N \frac{1}{N!}\frac{1}{\Lambda^{3N}}\exp(\beta\mu N)\int d\vec{r}\,d\vec{p}\exp(-\beta H(\vec{r},\vec{p})) \tag{3.19}$$

where $\Lambda = \sqrt{h^2/2\pi m k_b T}$ is the de Broglie wavelength of the particles and $E(N)$ is the configurational energy of the system with coordinates r^N. Multiple simulations are run to collect multiple histograms (one histogram for each simulation) to cover all thermodynamic states of interest. Histograms starting from the vapor phase to the dense liquid phase are collected by running simulations at different chemical potential and temperature. Between the vapor phase and the liquid phase, a bridge phase histogram is obtained by running the simulation close to the critical point. The bridge phase essentially connects the vapor and

the liquid phase. Additional simulations are performed at lower temperatures in both the liquid and vapor phases to cover the entire coexistence curve.

A plot of histograms collected as a function of number of molecules for sarin is shown in Figure 3.1. The neighboring histograms should have reasonable overlap for determination of accurate phase coexistence points. The histograms are patched according to the method of Ferrenberg and Swendsen [64, 117]. The distribution by patching R histograms together is given by

$$P(N,E) = \frac{\sum_{n=1}^{R} P_n(N,E)\exp[\beta(\mu N - E)]}{\sum_{m=1}^{R} k_m \exp[\beta_m(\mu_m N - E - f_m)]} \tag{3.20}$$

where k_m is the total number of observations for the run m and f_n is given by

$$\exp(f_m) = \sum_{N,E} P(N,E) \tag{3.21}$$

The values of f_m are found self-consistently by iterating equations 3.20 and 3.21. The coexistence densities are determined by taking the weighted average under each peak of the distribution. The pressure in the grand canonical ensemble is given by,

$$\beta P = \frac{\ln[\Xi(\mu,V,T) + C]}{V} \tag{3.22}$$

where C is an additive constant. C is determined by computing the partition function Ξ at low densities and extrapolating to the limit of ρ approaching zero. The pressure of each phase is calculated by choosing the equilibrium chemical potential and integrating the area under each peak of the resultant probability distribution.

Three types of moves are performed in GCMC simulation: particle displacement or

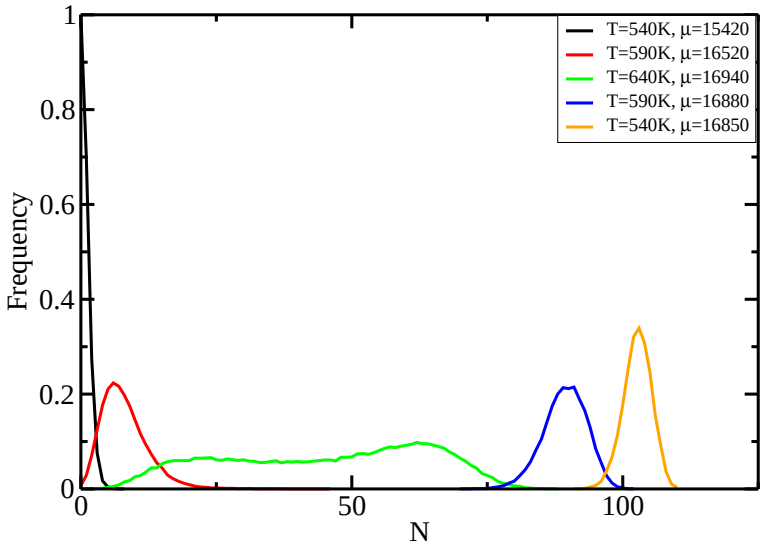

Figure 3.1: Histograms from the simulation of phase coexistence for sarin. Run conditions for each histogram are listed in the legend (T is the temperature and μ is the chemical potential).

rotation, insertion and deletion.

1. *Particle displacements:* A particle is randomly chosen in the simulation box, then it is given a random move and displaced to a new position represented by the following expression:

$$r_{new} = r_{old} + (2.0\,\xi - 1.0)\mathrm{disp}_{max} \tag{3.23}$$

r_{new} and r_{old} are new and old x, y, z coordinates, respectively. The maximum displacement (disp_{max}) is varied during the course of the simulation to maintain a 50% probability for the success of an attempted displacement move. ξ is a random number generated uniformly between [0,1]. Displacement moves are accepted with a probability

$$P = \min\{1, \exp(-\Delta U/k_b T)\} \tag{3.24}$$

where $\Delta U = U_{new} - U_{old}$ and k_b is the Boltzmann constant.

2. *Particle rotations:* A particle is chosen at random and rotated about its center of mass in the x, y and z directions. The angular displacement is chosen at random

$$\theta = (2.0\xi - 1.0)\text{rmrot} \tag{3.25}$$

where "rmrot" is the maximum angular displacement about the x, y, or z axis. Rotations are accepted with a probability:

$$P = \min\{1, \exp(-\Delta U/k_b T)\} \tag{3.26}$$

where ΔU is the same as defined above.

3. *Particle insertion:* Particles are inserted in the simulation box by choosing a position and orientation at random. The acceptance probability for particle creations is

$$P = \min\{1, \frac{V\exp(\mu/k_b T)}{\Lambda^3(N+1)}\exp(-\Delta U/k_b T)\} \tag{3.27}$$

where V is the volume of the simulation box and N is the total number of particles. The de Broglie wavelength is given by $\Lambda = \sqrt{\frac{2\pi h}{k_b T m}}$, while μ is the chemical potential.

4. *Particle deletion:* Particles are removed from the simulation box by choosing one at random and removing it from the system. The probability of accepting this move is

$$P = \min\{1, \frac{\Lambda^3 N}{V\exp(\mu/k_b T)}\exp(-\Delta U/k_b T)\} \tag{3.28}$$

3.2.4 NPT Molecular Dynamics

Unlike MC simulation, molecular dynamics technique computes the time dependant behavior of a system. The principle behind any MD simulation is integration of Newton's equations of motion. A system is initialized by assigning atoms with random positions and velocities followed by computation of forces between the atoms. With the knowledge of the force and the initial positions and velocities, the equation of motion can be numerically integrated to calculate a trajectory which describes the positions, velocities and accelerations of the atoms with respect to time. From this trajectory, time average of any property A can be calculated by,

$$< A >= \frac{1}{M} \sum_{i=1}^{M} A_i \tag{3.29}$$

where M is the number of configurations in the molecular dynamics trajectory generated through time and A_i is the value of the property of interest at each configuration. The force between the particles is calculated by

$$f_x(r) = -\frac{x}{r} \left(\frac{\partial u(r)}{\partial x} \right) \tag{3.30}$$

where $f_x(r)$ is the x-component of force and $u(r)$ is the potential energy. The most common Verlet integration algorithm calculates new positions at time t using positions from time t and $t - dt$ by,

$$r(t + \delta t) = 2r(t) - r(t - \delta t) + a(t)\delta t^2 \tag{3.31}$$

where $a(t)$ are the accelerations and $r(t-\delta t)$ are the positions from the previous step. The velocities used to compute kinetic energy are obtained from

$$v(t) = \frac{r(t+\delta t) - r(t-\delta t)}{2\delta t} \tag{3.32}$$

In the isothermal isobaric ensemble (NPT), number of particles, pressure and temperature of the system are constant. Usually, a thermostat and a barostat are used to accomplish temperature and pressure control repectively in a molecular dynamics simulation. The NPT molecular dynamics simulations were carried out using the simulation software NAMD [118]. In NAMD, the equations of motion for the NPT ensemble are generated by modified Nosé Hoover method [119]. The temperature control is established using Langevin dynamics [120]. An additional degree of freedom in the form of piston with an arbitrary mass W was introduced that corresponds to the volume of the simulation box and self adjusts to maintain equality between the internal and the applied pressure. In the Langevin piston method, partial damping of piston is allowed and controlled through a Langevin equation presented below. The equations of motion for this Nosé Hoover and Langevin dynamics algorithm are,

$$\dot{r}_i = \frac{p_i}{m_i} + \frac{p_\epsilon}{W} r_i \tag{3.33}$$

$$\dot{p}_i = f_i - (1 + \frac{3}{N_f})\frac{p_\epsilon}{W} p_i \tag{3.34}$$

$$\dot{V} = \frac{3V p_\epsilon}{W} \tag{3.35}$$

$$\ddot{V} = \frac{1}{W}[P(t) - P_{ext}] - \gamma \dot{V} + R(t) \tag{3.36}$$

where r_i, p_i are the position and the momentum of the ith particle, V is the volume of the

simulation box, p_ϵ is the barostat momentum, W is the piston mass, N_f is the number of degrees of freedom, $P(t)$ is the instantaneous pressure, P_{ext} is the applied pressure, γ is the collision frequency of the piston and $R(t)$ is a random force having a gaussian distribution with zero mean and variance given by,

$$< R(0)R(t) >= \frac{2\gamma k_b T \delta(t)}{W} \tag{3.37}$$

where k_b is the Boltzmann's constant.

3.2.5 Adsorption

Adsorption is carried out with two simulation methods: Grand Canonical Monte Carlo Simulation (GCMC) and Gibbs Ensemble Monte Carlo Simulation (GEMC). GCMC simulation is used for obtaining pure component adsorption isotherms while GEMC is used for mixture adsorption isotherms. In GCMC simulation, the temperature, volume and chemical potential of the pore is fixed. At equilibrium, the temperature and the chemical potential of the fluid in the pore and the bulk phase are equal. A separate bulk simulation is used to calculate the pressure with the same temperature and chemical potential as the pore simulation. The pressure is computed via virial theorem using a pairwise sum given by,

$$P = \rho k_b T + \frac{1}{3V} \sum_i \sum_{j>1} r_{ij}.f_{ij} \tag{3.38}$$

where ρ is the density and V is the volume of the simulation box, i, j are interaction sites, r_{ij} is the separation and f_{ij} is the force on atom i due to atom j.

The probability density of having N molecules in the pore is

$$P(N,T) = \frac{\exp(N\beta\mu)}{\Xi(\mu,V,T)} Q(N,V,T) \tag{3.39}$$

where $\beta = 1/k_\beta T$, μ is the chemical potential, $Q(N,V,T)$ and $\Xi(\mu,V,T)$ are the canonical and grand canonical partition functions of the system respectively. The partition functions are given by,

$$Q(N,V,T) = \frac{1}{N!\lambda^{3N}} \int \exp[-\beta\Phi(r^N)] dr^N \tag{3.40}$$

where λ is the thermal wavelength of the molecules, $\Phi(r^N)$ is the potential energy of the system and r^N represents the position of all N molecules.

$$\Xi(\mu,V,T) = \sum_N \exp(\mu N/k_\beta T) Q(N,V,T) \tag{3.41}$$

The probability of a trial move being accepted in a GCMC simulation were already discussed in the GCHRMC section.

In the GEMC method [121, 122], constant pressure simulations are used to conduct adsorption. In a typical constant pressure GEMC simulation, there are two simulation boxes, one representing the pore and the other representing the coexisting bulk fluid. The conditions of equilibrium for the fluid inside the pore and the bulk phase is

$$T_1 = T_2 \tag{3.42}$$

$$\mu_1 = \mu_2 \tag{3.43}$$

where subscripts 1 and 2 represent the pore and bulk phases respectively. The condition

for mechanical equilibrium is automatically satisfied by the equality in chemical potential unlike the fluid phase equilibria. The number of particles N, the temperature of the system T, volume of the pore V_p and the pressure of the bulk fluid are fixed. Although the number of particles in the pore N_p and the bulk N_b are allowed to vary, the total number N is constant. Three types of moves are used in an adsorption simulation: particle displacement, volume change of bulk fluid and transfer move. A schematic of moves applied in the Gibbs ensemble simulation of adsorption are shown in Figure 3.2. Acceptance citeria for the displacement move is discussed in the GCMC simulation. Rest of the moves are accepted with a probability of

1. *Volume Change:*

$$P(V_{bo} \rightarrow V_{bn}) = \min\{1, \exp(-\beta[\Delta U_b + P(V_{bn} - V_{bo}) - N_b kT \ln(V_{bn}/V_{bo})])\} \quad (3.44)$$

where ΔU_b is the change in the configurational energy of the bulk, P is the pressure, V_{bo} and V_{bn} are the volume of the bulk before and after the move.

2. *Bulk to pore transfer:*

$$P(N_p \rightarrow N_p + 1) = \min\{1, \exp(-\beta[\Delta U_p + \Delta U_b])\frac{N_b V_p}{(N_p + 1)V_b}\} \quad (3.45)$$

where ΔU_p is the change in the configurational energy of the pore, ΔU_b is the change in the configurational energy of the bulk, N_b is the number of particles in the bulk, N_p is the number of particles in the pore, V_p is the volume of the pore and V_b is the volume of the bulk.

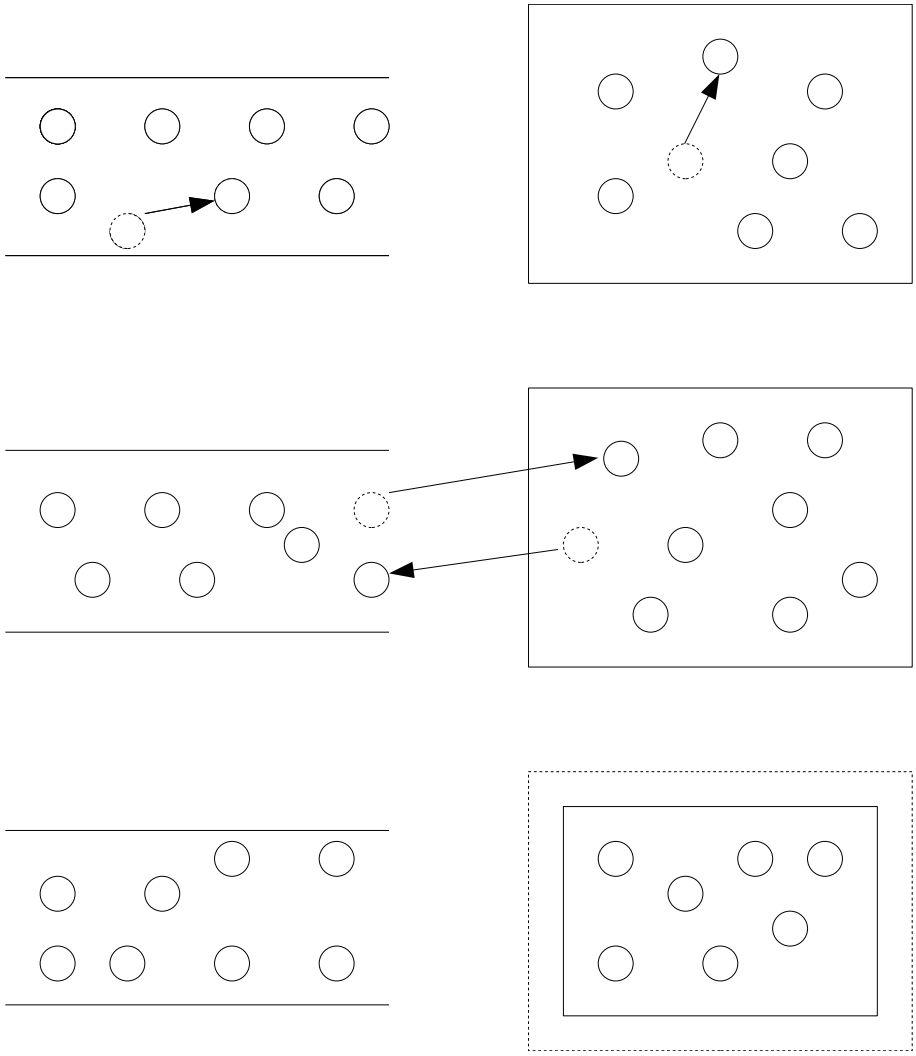

Figure 3.2: Types of moves attempted in the pore (left) and the bulk (right) of a GEMC adsorption simulation. Displacement move (top); Pore to bulk and bulk to pore transfer move (middle); Volume move of the bulk (bottom)

3. *Pore to bulk transfer:*

$$P(N_p \rightarrow N_p - 1) = \min\{1, \exp(-\beta[\Delta U_p + \Delta U_b]) \frac{N_p V_b}{(N_b + 1)V_p}\} \tag{3.46}$$

3.2.6 Coupled-Decoupled Configurational-Bias Monte Carlo

Coupled-decoupled CBMC technique [113] was developed as one of the trial moves for MC simulation to insert branched chain molecules that have strong intramolecular interactions into a dense phase. The basic concept behind the CBMC move is that the molecules are grown atom by atom into low energy positions using Rosenbluth sampling in a dense fluid to avoid poor acceptance rate for molecule insertion. The growing mechanism introduces a bias which is removed in the acceptance rule. This considerably increases the acceptance rate for insertion of long chain molecules.

In the coupled-decoupled method, the flexible bond angles are decoupled from the torsions and the latter is coupled to the non-bonded terms. First, in the coupled section, the bond angles are generated with a bias solely based on the bond angle energies and phase space terms. Once the bond angle distribution is chosen, it is used as an input to the subsequent decoupled section where the torsion and the non-bonded energies are computed. This process has the advantage that a large number of trial sites can be sampled for the less expensive bond-angle selection and the expensive non-bonded term is computed only for a few trial sites. In the decoupled biased growth, the probability of generating a given configuration is given by,

$$P = \prod_{n=1}^{nstep} \left[\frac{\exp(-\beta u_{nb}(i))}{W_{nb}(n)}\right] \left[\frac{\exp(-\beta u_t(j))}{W_t(n)}\right] \left[\frac{\exp(-\beta u_b(j))}{W_b(n)}\right] \tag{3.47}$$

where n is the growth step, n_{step} is the total number of growth steps, $\beta = 1/k_bT$, u_{nb}, u_t and u_b are the non-bonded, torsional and bond angle energies respectively and i, j and k

are the trial numbers. The Rosenbluth weights are given by,

$$W_{nb}(n) = \sum_{i=1}^{n_{nb}} \exp(-\beta u_{nb}(i)) \tag{3.48}$$

$$W_t(n) = \sum_{j=1}^{n_t} \exp(-\beta u_t(j)) \tag{3.49}$$

$$W_b(n) = \sum_{k=1}^{n_b} \exp(-\beta u_b(k)) \tag{3.50}$$

where n_{nb}, n_t and n_b are the number of trial sites for the non-bonded, torsional and bond bending interactions respectively. The growth move is accepted with a probability

$$P_{acc} = \min\left[1, \frac{\prod_{n=1}^{nstep} W_{nb}(n)_n W_t(n)_n W_b(n)_n}{\prod_{n=1}^{nstep} W_{nb}(n)_o W_t(n)_o W_b(n)_o}\right] \tag{3.51}$$

In the coupled biased growth, the probability of generating a given configuration is given by,

$$P = \prod_{n=1}^{nstep} \left[\frac{\exp(-\beta u_{nb}(i)) W_t(i)}{W_{nb}(n)}\right] \left[\frac{\exp(-\beta u_t(j)) W_b(j)}{W_t(n)}\right] \left[\frac{\exp(-\beta u_b(j))}{W_b(n)}\right] \tag{3.52}$$

where the Rosenbluth weights are given by,

$$W_{nb}(n) = \sum_{i=1}^{n_{nb}} \exp(-\beta u_{nb}(i)) W_t(i) \tag{3.53}$$

$$W_t(i) = \sum_{j=1}^{n_t} \exp(-\beta u_t(j)) W_b(j) \tag{3.54}$$

$$W_b(j) = \sum_{k=1}^{n_b} \exp(-\beta u_b(k)) \tag{3.55}$$

The growth move is accepted with a probability

$$P_{acc} = \min\left[1, \frac{\prod_{n=1}^{nstep} W_{nb}(n)_n}{\prod_{n=1}^{nstep} W_{nb}(n)_o}\right] \tag{3.56}$$

A combination of the decoupled and coupled biased growth constitutes the couple-decoupled CBMC which is a very effective way of simulating flexible molecules.

3.3 Computation of Interactions

In addition to the general simulation techniques, it is also important to know how the interactions, i.e., the potential energies are treated and computed in a typical simulation. In this regard, details about potential truncation and ewald summation for electrostatics are presented.

3.3.1 Potential Truncation

Since the Lennard-Jones Potential has an infinite range, it is necessary to truncate the potential to make it finite. Two types of methods are used to truncate potentials: simple truncation, truncation and shift. Simple truncations ignore the interactions beyond a certain distance called the spherical cut-off radius. The potential for this type is,

$$u(r) = \begin{cases} u^{lj}(r) & \text{if } r \leq r_c \\ u(r) = 0 & \text{if } r > r_c \end{cases}$$

where u^{lj} is the Lennard Jones potential. In the second method, the potential looks like,

$$u(r) = \begin{cases} u^{lj}(r) - u^{lj}(r_c) & \text{if } r \leq r_c \\ u(r) = 0 & \text{if } r > r_c \end{cases}$$

The penalty of applying potential truncations can be eliminated by implementing long

range corrections to account for the long range nature of the potential. The long range part of the potential is calculated by,

$$u_{tail} = \frac{8}{3}\pi\rho\varepsilon\sigma^3\left[\left(\frac{\sigma}{r_c}\right)^9 - \left(\frac{\sigma}{r_c}\right)^3\right] \tag{3.57}$$

where ρ is the average number density and r_c is the cut-off radius. For all the Monte Carlo simulations with the CWA, a truncated potential with long range corrections was used. For the Monte Carlo and molecular dynamics simulations of the energetic materials, a truncated and shifted potential was used.

3.4 Ewald Summation

Coulombic interaction between molecules is a long range potential given by,

$$U_{coulomb} = \frac{1}{2}\sum_{i=1}^{N}\sum_{i=1}^{N}\frac{q_i q_j}{r_{ij}} \tag{3.58}$$

where N is the number of particles, q_i, q_j are partial charges on particles i and j respectively and r_{ij} is the separation between them. This potential is computationally expensive to calculate and a spherical truncation would result in inaccurate results. Ewald summation [123] is the most accurate way of computing long range electrostatic interactions between molecules themselves and their periodic images in a simulation. In this method, the coulombic interaction potential is separated into three terms given by,

$$U_{coulomb} = U_{real} + U_{imag} + U_{corr} \tag{3.59}$$

where U_{real} is the short range real space sum, U_{imag} is the long range imaginary sum and U_{corr} is the correction term. The short range and the long range part sum quickly in the real space and the Fourier space respectively. In Ewald summation, for real space sum, each point charge q_i is assumed to be surrounded by a Gaussian charge cloud of equal magnitude and opposite sign with a charge density,

$$\rho_i(r) = q_i\alpha^3 exp(-\alpha^2 r^2)/\sqrt{\pi^3} \tag{3.60}$$

where r is the position relative to the center of the charge distribution, α is a parameter that determines the width of the gaussian distribution. The inclusion of the charge cloud limits the real space sum to short range by screening the interaction between neighboring point-charges. For the Fourier sum, a similar second charge cloud with same charge and sign as the original cloud is added for each point charge and the resulting Poisson's equation is solved using Fourier transform. The resultant equation for real space and Fourier space sums are,

$$U_{real} = \frac{1}{2}\sum_{i,j}^{N} \frac{q_i q_j \,\mathrm{erfc}(\alpha r_{ij})}{r_{ij}} \tag{3.61}$$

where $\mathrm{erfc}(x) = 1 - \mathrm{erf}(x)$ and is a rapidly decaying function and

$$U_{imag} = \frac{1}{2\pi V}\sum_{i,j}^{N}\sum_{k\neq 0} \frac{\exp(-(\pi k/\alpha)^2 + 2\pi i k.(r_i - r_j))}{k^2} \tag{3.62}$$

where V is the volume of the simulation box, k is the Fourier transform variable, r_i and r_j are the positions of particles i and j. A schematic of Ewald summation is shown in Figure 3.3. The effect of inclusion of additional charge clouds are nullified by adding the

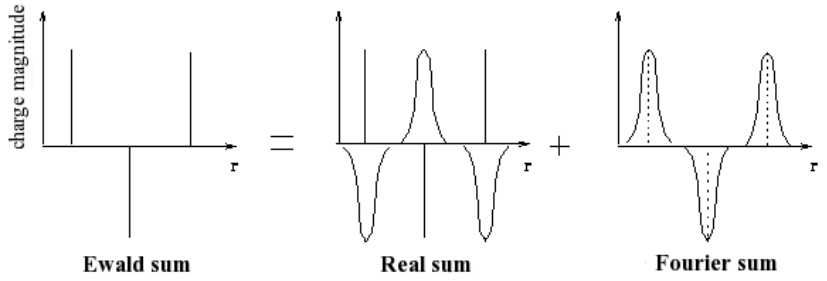

Figure 3.3: Schematic [124] of ewald summation

correction term in Eq. 3.59 which is given by,

$$U_{corr} = \frac{-\alpha}{\sqrt{\pi}} \sum_{i=1}^{N} q_i^2 \tag{3.63}$$

In all the Monte Carlo simulations runs, Ewald summation was used to compute long range electrostatic potential. Despite its efficiency, Ewald summation scales as $O(N^2)$ which makes it inapplicable to larger systems. An alternative to the Ewald summation algorithm is the Particle Mesh Ewald (PME) method [125] which scales as $O(N)$. All the Molecular Dynamics simulation in this work used PME method to compute Coulombic potential. In this technique, the Fourier sum is approximated by multidimensional piecewise interpolation. The basic steps that constitute the PME algoritm are

1. A finely-spaced mesh is added to the simulation box

2. Charges are assigned to the mesh points to approximate the charge density.

3. The electrostatic potential due to the charge distribution on the mesh which is represented as Poisson's equation is computed using fast Fourier transform technique.

4. The field at each mesh point is calculated by differentiating the potential and the force on each particle is calculated by interpolation from the mesh field.

Chapter 4

Conformational Behavior of Energetic Materials

4.1 Introduction

The explosives derive most of their characteristics from the nitro and the amino functional groups. So, it is necessary to determine accurate rotational barriers for the development of atomistic force fields for use in molecular dynamics simulations. The prediction of rotational barriers of the nitro and the amino group also offers valuable insight into the intramolecular interactions such as resonance, steric effects and hydrogen bonding. With *ab initio* calculations of energetic materials, it is also possible to correlate impact sensitivity which is a characteristic of energetic materials to a few molecular properties such as structure and partial charges.

To date, very few computational or experimental studies on the internal rotation around the C-N bond and the C-O bond in the energetic materials of interest have been published. Experimental work on the internal rotation around the C-NH bond in MNA (N-methyl-p-nitroaniline) has been published [126]. Manaa *et.al* [147] reported *ab initio* calculations for nitro and amino group rotational barriers for another IM (Insensitive Munition) compound, 1,3,5-triamino-2,4,6-trinitrobenzene (TATB), to determine the conjugate effect between the amine and nitro groups and the phenyl ring. Theoretical studies have been reported for rotation of the functional groups of interest as part of other molecules, such as the -OCH_3 group in anisole [127], -NO_2 group in nitrobenzene [128], -$HNCH_3$ group in triazine [129] and para-substituted anisoles [130]. Similar experimental NMR, resonance fluorescence, infrared

and microwave spectroscopy studies were also reported for determination of structures and gas phase rotational barriers in substituted benzenes [131–141]. NMR spectra was applied to a variety of ortho substituted anisoles to measure the chemical shifts and proton deshielding, providing information about resonance interactions [142–145]. X-ray scattering performed on single crystal 2-methoxy-3,5-dinitropyridine, which has a structure similar to DNAN (one ring carbon replaced by nitrogen), was used to identify various resonance, conjugation and steric effects [146]. In this chapter, rotational barriers are predicted for DNAN, MNA, DNP and NTO around the C-N and C-O bond (DNAN) and a sensitivity analysis of the energetic materials is presented.

4.2 Sensitivity Analysis

The primary property that makes IM compounds desirable are their reduced sensitivity to shock or impact. In an effort to understand the factors that affect sensitivity, sensitivity correlations that aid in relating molecular structures or electrostatic potential to sensitivity have been proposed [148–152]. In case of nitroaromatics, the C-NO_2 bond is the trigger linkage and scission of these bonds acts as the initial step in the thermal decomposition of energetic materials [153–158]. As a result, the sensitivity depends on the strength and stability of the C-NO_2 bond. So there has been considerable focus on relating sensitivity with the properties of the C-NO_2 bond. One quantity that directly influences the C-NO_2 bond is the electrostatic potential at the midpoint of the C-NO_2 bond, V_{mid} [149], which is given by,

$$V_{mid} = \frac{Q_C}{0.5R} + \frac{Q_N}{0.5R} \tag{4.1}$$

where Q_C and Q_N are the the charges on carbon and nitrogen atoms respectively and R is the longest bond length corresponding to the C-NO_2 bond. Higher the value of V_{mid},

Table 4.1: Sensitivity parameters for the energetic materials

Molecule	Q_C	Q_N	R	V_{mid}
DNAN	-0.13	0.82	1.46	0.95
MNA	-0.08	0.76	1.45	0.94
DNP	0.38	0.75	1.44	1.56
NTO	0.43	0.77	1.44	1.67
MTNI	-0.21	0.91	1.45	0.97
TATB	-0.75	1.09	1.43	0.47

higher is the impact sensitivity of the molecule. The presence of strong resonance donors such as NH_2, OH, OCH_3 in a molecule strengthen the C-NO_2 by donating electrons thereby decreasing the positive charges of the carbon and nitrogen atoms and decreasing V_{mid}. The parameters Q_C, Q_N, R and V_{mid} predicted at the HF/6-31G+(d,p) level of theory and basis set are listed in Table 4.1. The charges listed in the Table are from the CHELPG scheme in Gaussian [109]. As seen from the table, TATB is the most insensitive of all with the lowest V_{mid} which agrees with the experimental finding [159]. The presence of amine groups and extensive intramolecular hydrogen bonding in TATB [147] have increased the NO_2 rotational barrier. So accidental detonation is least possible in TATB since one of the first events to occur in TATB initiation is C-NO_2 homolysis [153]. Unless there is any proper initiation, the energetic materials of interest will not detonate automatically. The sensitivity correlation explained here is generally limited to nitroaromatics. Few concerns with any sensitivity correlation method are that the initiation of detonation depends on a complex interplay of various molecular, crystal and physical factors. As a result, V_{mid} may not be the only property that governs the detonation of the energetic materials. However, these relationships may be used as a preliminary method of testing a compound's sensitivity.

4.3 DNAN & MNA

4.3.1 Computational Methodology

The optimization of the structures and the dihedral scans were performed with Gaussian 03 using Hatree-Fock(HF), Møller Plesset(MP2) and density functional theory (B3LYP) with the 6-31G+(d,p) basis set. Optimizations were started from a number of initial conformations to confirm the predicted structures were true minimum energy conformers. Barriers to rotation for the various substituent groups were determined from relaxed potential energy scans, where the dihedral angle of interest was fixed and the remaining degrees of freedom were optimized.

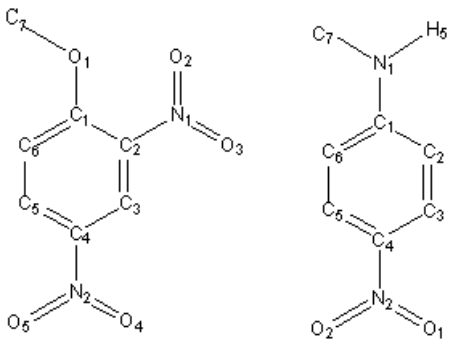

Figure 4.1: Molecular structure of DNAN (left) and MNA (right)

Each scan involved a sweep of dihedral angles from -180° to 180° in 20° increments. The conformational behavior of DNAN and MNA are analyzed with Hartree-Fock (HF), Moller Plesset (MP2) and density functional theory using the hybrid B3LYP functional to check for other stable conformers. A schematic of DNAN and MNA structures are shown in Figure 4.1.

4.3.2 Equilibrium Structure

For DNAN, HF, MP2 and B3LYP calculations predicted a co-planar structure with the methoxy and the p-nitro groups in plane with the aromatic ring, while the ortho-nitro group was tilted out of plane. The methoxy group was observed lying anti to the o-nitro group, avoiding steric overlap. Equilibrium parameters for DNAN optimized at HF, MP2 and B3LYP theories are presented in Table 4.2 with the experimental values [160] for comparison. The bond lengths and angles predicted from Gaussian are in good agreement with the experiment. In general, the nitro group always stays in plane with the aromatic ring but in DNAN, it is forced out of the plane and distorted by the methoxy group in all levels of theories due to steric and packing effects. NMR studies on substituted anisoles [142] reveal the presence of steric hindrance between the methoxy and the ortho nitro group.

Tilting of the C-O bond is observed for all three levels of theories. The repulsion between the methyl group and the hydrogen attached to C_6 governs the tilting of the C-O bond. The C-C-C angles vary from 118 to 122° due to the internal rearrangements that the molecule undergoes to relieve steric compression from the substituent groups. The length of the C-O bond predicted by *ab initio*, DFT calculations and experimental data (1.33-1.35 Å) was less than the C-O bond length in anisole (1.37 Å) [161]. The shortening of the C-O bond length indicates the presence of some double bond character due to the resonance of the methoxy group with the p-nitro group. The electron release by the oxygen atom to the aromatic ring results in an increase in electron density at the para position. This phenomena was observed experimentally and explained by Buchanan *et al.* [142]. A schematic of the resonance effect found in DNAN is shown in Figure 4.2. Weak intramolecular hydrogen bonding, where the oxygen from the p-nitro group interacts with the adjacent hydrogen atoms, was predicted

Table 4.2: Molecular parameters for DNAN

Parameter	HF	B3LYP	MP2	Exp (A) [160]
Bond Lengths (Å)				
C1-C2	1.403	1.417	1.406	1.402
C2-C3	1.375	1.386	1.384	1.361
C3-C4	1.382	1.391	1.393	1.388
C4-C5	1.383	1.394	1.390	1.369
C5-C6	1.381	1.389	1.396	1.372
C6-C1	1.397	1.408	1.402	1.377
C1-O1	1.318	1.339	1.354	1.333
O1-C7	1.412	1.431	1.434	1.436
C2-N1	1.459	1.472	1.462	1.475
N1-O2	1.189	1.227	1.243	1.188
N1-O3	1.196	1.232	1.245	1.190
C4-N2	1.452	1.466	1.469	1.468
N2-O4	1.194	1.231	1.244	1.211
N2-O5	1.195	1.232	1.243	1.212
Angle(Degree)				
C1-C2-C3	122.0	121.7	122.9	123.8
C2-C3-C4	118.6	118.7	117.3	116.7
C3-C4-C5	121.1	121.2	122.0	121.9
C4-C5-C6	119.8	119.5	119.2	119.6
C5-C6-C1	120.7	120.8	120.6	121.3
C6-C1-C2	117.7	117.7	117.7	116.8
O1-C1-C2	118.2	118.0	116.5	118.9
O1-C1-C6	124.0	124.1	125.7	124.3
C7-O1-C1	121.3	119.7	117.2	118.5
N1-C2-C1	121.2	121.2	118.9	120.2
N1-C2-C3	116.8	116.9	118.1	116.0
O2-N1-C2	118.0	117.9	116.9	119.0
O3-N1-C2	116.6	116.7	116.8	117.2
O2-N1-O3	125.4	125.2	126.2	123.8
N2-C4-C3	119.2	119.1	118.6	118.4
N2-C4-C5	119.6	119.5	119.2	119.7
O4-N2-C4	117.6	117.7	117.4	119.0
O5-N2-C4	117.4	117.5	117.4	117.2
O4-N2-O5	125.0	124.7	125.1	123.8

by all theory levels.

For MNA, both *ab initio* and DFT methods predicted a planar structure. The equilibrium parameters, listed in Table 4.3, agree well with the experimental solid structure [162].

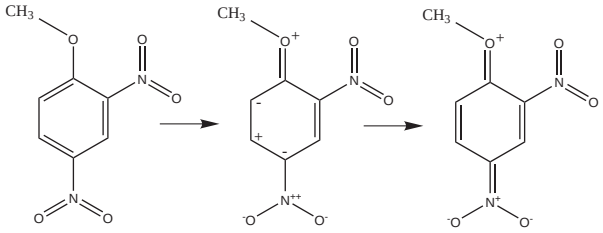

Figure 4.2: Resonance structures for DNAN

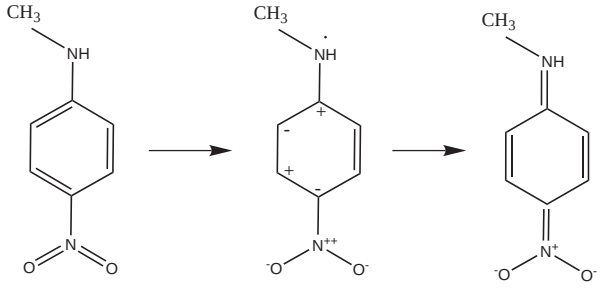

Figure 4.3: Resonance structures for MNA

Although experimental [163–165] and theoretical [166] studies predict a pyramidal nitrogen for aniline, the substitution of a methyl group in place of a hydrogen in the amine group, and conjugate effects among the strong electron-donor amine group and the phenyl ring caused a decrease in pyramidalisation [167, 168]. As observed from the data in Table 4.3, HF, B3LYP, and MP2 results agree well with the experimental bond lengths and angles. The equilibrium C-NH bond length was shorter than the typical equilibrium C-N single bond of 1.45 Å. The reason for shortening of the C-NH bond is due to the presence of some double bond characteristics, which are caused by conjugate effects between the ring and the amino and nitro groups. Although C-NO_2 has a bond length of 1.43 Å, which is close to the length of a single bond, it exhibits some double bond character due to the NH-electron donor and the NO_2 acceptor interaction, as shown in Figure 4.3. Similar to DNAN, weak intramolecular hydogen bonding is observed in MNA.

Table 4.3: Molecular parameters for MNA

Parameter	HF	B3LYP	MP2	Experiment [162]
Bond Lengths(Å)				
C1-C2	1.408	1.418	1.412	1.387
C2-C3	1.371	1.382	1.387	1.368
C3-C4	1.391	1.401	1.397	1.396
C4-C5	1.383	1.396	1.392	1.372
C5-C6	1.380	1.388	1.393	1.373
C6-C1	1.403	1.415	1.410	1.417
C1-N1	1.359	1.368	1.373	1.358
N1-H5	0.991	1.007	1.006	0.890
N1-C7	1.441	1.449	1.446	1.439
C4-N2	1.444	1.452	1.460	1.434
N2-O1	1.197	1.237	1.246	1.226
N2-O2	1.197	1.237	1.246	1.243
Angle(Degree)				
C1-C2-C3	120.86	120.95	121.22	122.0
C2-C3-C4	119.59	119.51	118.92	118.7
C3-C4-C5	120.64	120.70	121.40	120.9
C4-C5-C6	119.99	119.87	119.31	120.5
C5-C6-C1	120.39	120.49	120.73	119.8
C6-C1-C2	118.50	118.44	118.38	118.3
N1-C1-C2	119.59	119.79	120.06	120.4
N1-C1-C6	121.89	121.75	121.54	121.3
H5-N1-C1	117.36	117.35	117.82	112.0
C7-N1-C1	124.79	124.71	123.62	124.8
H5-N1-C7	117.84	117.93	118.54	123.0
N2-C4-C3	119.64	119.60	119.25	118.3
N2-C4-C5	119.70	119.68	119.33	120.8
O1-N2-C4	117.88	118.04	117.79	120.0
O2-N2-C4	117.98	118.14	117.90	118.0
O1-N2-O2	124.13	123.81	124.30	122.0

4.3.3 Torsional Barriers

Torsional barriers for the methoxy, ortho- and para- nitro groups in DNAN are shown in Figures 4.4, 4.5 and 4.6, respectively. The predicted barriers to rotation in DNAN and MNA are presented in Table 4.4. For rotational barrier, B3LYP and HF predict peaks about 2-3 kcal/mol higher than the corresponding results from MP2 calculations. This is due to

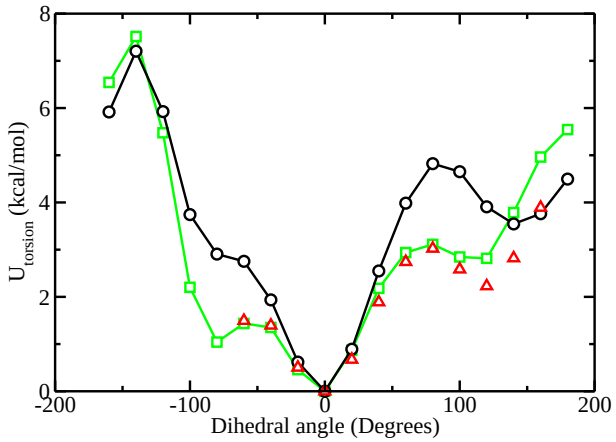

Figure 4.4: Torsional barrier for methoxy group (C-O-C-C dihedral) in DNAN. Prediction of HF/6-31G+(d,p)(green), B3LYP/6-31G+(d,p) calculations(black), and MP2/6-31G+(d,p)(red).

the electron correlation effects, which are significant in these molecules. Although the magnitude of the NO_2 barriers were different for MP2, HF and B3LYP theories, the location of maxima and minima were similar. The barrier to rotation of the para-nitro group predicted by MP2 theory is 4.2 kcal/mol, which is in good agreement with experimental results of 4.07 kcal/mol [169] and 4.54 kcal/mol [170] and prior *ab initio* calculations performed on nitrobenzene [128]. DFT and HF predicted a barrier of about 7 kcal/mol which is about 60% larger than experiment. For the ortho-nitro group rotation, all theories predict a barrier to rotation ranging from 1-1.75 kcal/mol, which is almost 50% lower than the p-nitro group barriers. Such low barriers, which occur at a nearly orthogonal conformation (100°) of the o-nitro group are due to the fact that there are no neighboring groups to cause steric hinderance or intramolecular hydrogen bonding interactions. For rotation of the methoxy group, the O_2-N_1-C_2-C_1 dihedral and the H-C_7-O_1-C_1 dihedral where H is the nearest hydrogen to the ortho hydrogen at C_6 are fixed to avoid steric crowding effects between the methoxy and bulky ortho substituent(nitro) group. B3LYP and HF calculations predicted a barrier of 7.2 and 7.5 kcal/mol respectively.

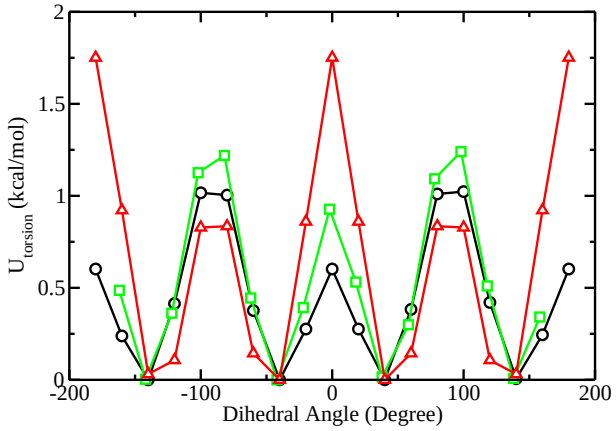

Figure 4.5: Torsional barrier for o-nitro group (O-N-C-C dihedral) in DNAN. Prediction of HF/6-31G+(d,p)(green), B3LYP/6-31G+(d,p) calculations(black), and MP2/6-31G+(d,p)(red).

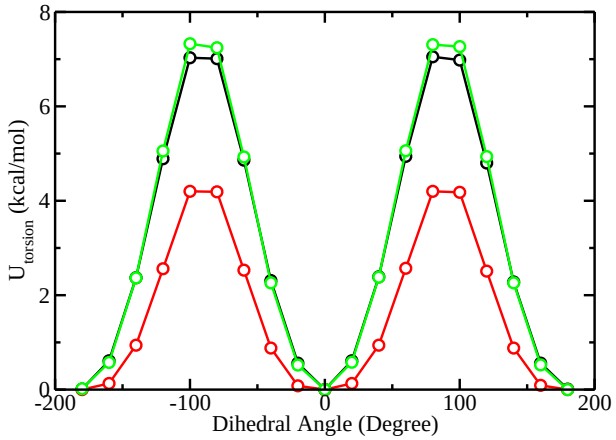

Figure 4.6: Torsional barrier for p-nitro group (O-N-C-C dihedral) in DNAN. Prediction of HF/6-31G+(d,p)(green), B3LYP/6-31G+(d,p) calculations(black), and MP2/6-31G+(d,p)(red).

Table 4.4: Rotational barriers in kcal/mol for DNAN and MNA at 6-31G+(d,p) basis set.

Functional Group	HF	B3LYP	MP2
DNAN			
Methoxy	7.5	7.2	-
O-Nitro	1.2	1.0	1.7
P-Nitro	7.2	7.0	4.2
MNA			
Methylamine	6.9	9.9	6.1
P-Nitro	8.8	8.6	4.6

Table 4.5: Optimized Molecular parameters for methoxy rotation in DNAN

Parameter	HF			B3LYP			MP2		
	0	40	80	0	40	80	0	40	80
C1-C2	1.40	1.39	1.39	1.41	1.41	1.40	1.40	1.40	1.40
C1-O1	1.31	1.32	1.33	1.33	1.34	1.35	1.35	1.36	1.36
O1-C7	1.41	1.41	1.41	1.43	1.43	1.43	1.43	1.44	1.44
C2-N1	1.45	1.45	1.46	1.47	1.47	1.47	1.46	1.46	1.46
N1-O2	1.18	1.18	1.18	1.22	1.22	1.22	1.24	1.24	1.24
C4-N2	1.45	1.45	1.45	1.46	1.46	1.47	1.46	1.47	1.47
N2-O4	1.19	1.19	1.19	1.23	1.23	1.23	1.24	1.24	1.24
C6-C1-C2	117.69	117.84	118.17	117.75	117.81	118.11	177.71	117.82	117.99
C2-C1-O1	118.22	119.42	121.98	118.08	119.25	121.71	116.54	117.50	120.11
C1-C2-N1	121.19	121.22	121.62	121.28	121.25	121.37	118.87	118.70	119.05
C3-C4-N2	119.23	119.11	118.90	119.18	119.05	118.82	118.67	118.55	118.36
O4-N2-O5	124.97	125.04	125.11	124.75	124.81	124.93	125.13	125.18	125.30
C5-C6-C1-C2	0.08	0.82	-0.25	-0.04	1.13	-0.10	-0.04	-3.14	-0.25

The optimized geometries resulting from the internal rotation around the C-O bond at dihedral angles 0°, 40° and 80° are presented in Table 4.5 and C-N bond in Table 4.6 and 4.7. Some significant observations can be made from these parameters. Tilting of the C-O bond is observed for both the methoxy and the o-nitro group rotation, which is evident from the C_2-C_1-O_1 angle. Also, the double bond character of the C-O bond decreases when the methoxy group rotates out of plane. When the ortho nitro group rotates, there is enough repulsion between the oxygens of the nitro group and the methoxy oxygen to force a change of about 3-4° in the C_2-C_1-O_1 and C_2-C_1-N_1 angle. This finding further confirms the presence of steric effects between the methoxy and the ortho nitro group. Overall, the interaction between the methoxy and the nitro group at the ortho position governs their internal rotation. While the rotational barriers of o-nitro group are affected strongly by the neighboring presence of the methoxy group, the rotation of the p-nitro group has little effect on the methoxy and o-nitro rotational barriers.

Barriers to dihedral rotation for the amino and the nitro groups in MNA are presented in Figure 4.7 and 4.8, respectively. The methyl-amino group torsion evaluated at B3LYP

Table 4.6: Optimized Molecular parameters for o-nitro rotation in DNAN

Parameter	HF			B3LYP			MP2		
	0	40	80	0	40	80	0	40	80
C1-C2	1.41	1.40	1.39	1.42	1.41	1.40	1.41	1.40	1.40
C1-O1	1.31	1.31	1.32	1.33	1.33	1.34	1.35	1.35	1.35
O1-C7	1.41	1.41	1.41	1.43	1.43	1.43	1.43	1.43	1.43
C2-N1	1.46	1.45	1.46	1.47	1.47	1.47	1.47	1.46	1.46
N1-O2	1.18	1.18	1.18	1.23	1.23	1.22	1.24	1.24	1.24
C4-N2	1.45	1.45	1.45	1.46	1.46	1.46	1.46	1.46	1.46
N2-O4	1.19	1.19	1.19	1.23	1.23	1.23	1.24	1.24	1.24
C1-C2-C3	120.95	121.93	122.74	120.85	121.76	122.56	121.44	122.45	123.01
C2-C1-O1	119.83	118.21	116.25	119.60	118.00	116.32	119.47	117.57	115.60
C1-C2-N1	122.97	121.32	118.47	122.97	121.20	118.49	122.62	120.66	117.73
C2-N1-O2	119.00	118.07	116.96	116.86	116.75	116.97	118.36	117.50	116.55
O2-N1-O3	124.38	125.32	126.13	124.37	125.30	126.08	124.78	125.89	126.64
C3-C4-N2	119.38	119.28	119.01	119.28	119.16	118.90	118.85	118.82	118.61
O4-N2-O5	124.95	124.95	124.94	124.77	124.75	124.69	125.15	125.14	125.09
C5-C6-C1-C2	0.01	-0.06	-0.23	0.06	0.13	-0.13	-0.01	1.24	-0.57
C2-C1-O1-C7	179.9	179.7	-179.4	-179.9	178.7	-179.8	-179.9	177.0	-179.7
C3-C4-N2-O4	0.01	0.53	0.12	0.03	0.57	0.48	0.05	0.77	1.19

Table 4.7: Optimized Molecular parameters for p-nitro rotation in DNAN

Parameter	HF			B3LYP			MP2		
	0	40	80	0	40	80	0	40	80
C3-C4	1.37	1.37	1.37	1.39	1.39	1.38	1.39	1.39	1.39
C1-O1	1.33	1.33	1.33	1.33	1.34	1.34	1.35	1.35	1.35
O1-C7	1.42	1.42	1.42	1.43	1.43	1.42	1.43	1.43	1.43
C2-N1	1.45	1.45	1.45	1.47	1.47	1.47	1.46	1.46	1.46
N1-O2	1.19	1.19	1.19	1.22	1.22	1.22	1.24	1.24	1.24
C4-N2	1.45	1.45	1.46	1.46	1.46	1.47	1.46	1.46	1.46
N2-O4	1.19	1.19	1.19	1.23	1.23	1.22	1.24	1.24	1.24
C3-C4-C5	122.02	122.29	122.33	121.74	122.05	122.27	121.29	121.45	121.71
C2-C1-O1	116.56	116.44	116.51	121.41	121.47	121.72	118.05	118.08	118.33
C1-C2-N1	118.87	118.92	119.15	120.96	121.08	121.18	121.24	121.36	121.67
C2-N1-O2	116.90	116.91	117.00	117.72	117.77	117.83	117.91	117.97	118.13
O2-N1-O3	126.24	126.24	126.18	125.36	125.34	125.34	125.28	125.23	125.09
C3-C4-N2	118.67	118.68	118.53	118.91	118.67	118.95	119.16	119.13	118.96
O4-N2-O5	125.09	125.64	125.97	125.10	125.53	125.93	124.75	125.25	125.75
C3-C4-C5-C6	0.41	1.95	1.50	-0.07	-2.79	-1.54	-0.21	1.68	0.86
C2-C1-O1-C7	-178.6	-179.0	-179.0	105.5	105.6	104.4	-178.6	-178.8	-178.3
C1-C2-N1-O2	-61.71	-61.65	-60.11	-40.28	-39.12	-39.11	-39.30	-38.17	-35.33

level of theory is 9.9 kcal/mol, and is in good agreement with the experimental value of 11.1 kcal/mol [126]. MP2 and HF theories underpredict these rotational barriers by approximately 50%. The presence of the methyl substituent in the amine group and the

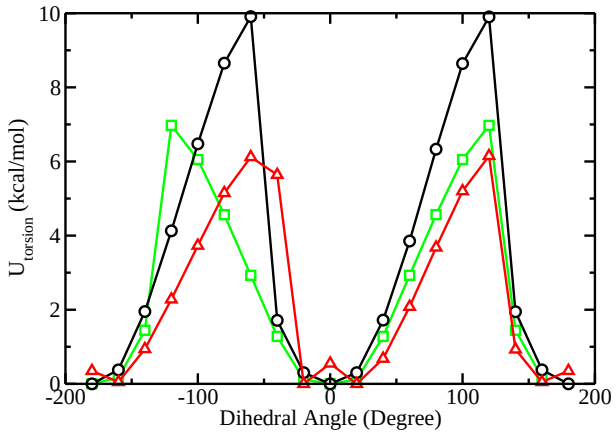

Figure 4.7: Torsional barrier for methyl-amine group (C-N-C-C dihedral) in MNA. Prediction of HF/6-31G+(d,p)(green), B3LYP/6-31G+(d,p) calculations(black), and MP2/6-31G+(d,p)(red).

para substituent (π electron acceptor) increases the rotational barrier around the C-N bond [126,129,171,172]. This explains the lower value for the barriers to rotation in aniline which is about 3.1 kcal/mol [166]. Internal rotation around the C-NH bond is more difficult compared to the C-NO_2 bond due to the partial double bond character of the C-N bond resulting in a difference of about 1.3-2 kcal/mol in their rotational barriers. Figure 4.7 shows discontinuities in the energy profile for all three plots. This behavior was also observed and explained for methylamine rotation by Birkett *et al* [129] in their work with substituted triazine rings. The discontinuous barrier to dihedral rotation is largely due to the ability of nitrogen in a substituted amine group to be both planar and pyramidal; when the pyramidal nature changes, there is a significant drop in energy.

As shown in Figure 4.7, MP2 predicts a minimum energy conformer for MNA with $HNCH_3$ rotated 10-20 degrees out of plane, while B3LYP and HF theories predict a flat $HNCH_3$, with both H and CH_3 groups in-plane with the aromatic ring. To further investigate this behavior, MP2 calculations were run with a double diffuse function (++) and larger basis set (6-311G+(d,p)), but both gave similar relative energies. Calculations per-

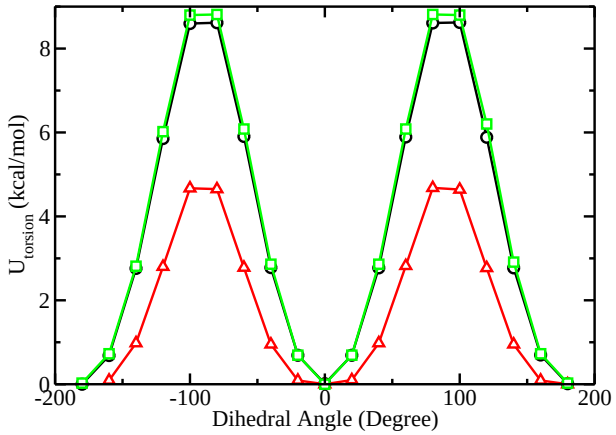

Figure 4.8: Torsional barrier for p-nitro group (O-N-C-C dihedral) in MNA. Prediction of HF/6-31G+(d,p)(green), B3LYP/6-31G+(d,p) calculations(black), and MP2/6-31G+(d,p)(red).

formed with QCISD theory and 3-21G basis set predict a C-N-C-C dihedral equal to 0° as the lowest energy conformer, in agreement with HF and B3LYP calculations. These results suggest that for molecules that have resonance structures, such as MNA, MP2 theory may give erroneous results for the lowest energy conformer.

For the nitro group in MNA, predicted barriers for rotation of the NO_2 group were 4.6 kcal/mol at MP2 level of theory, 8.6 kcal/mol at DFT and 8.8 kcal/mol at HF, which are slightly higher than the corresponding values for the para-nitro group in DNAN, inspite of the absence of adjacent groups. These larger rotational barriers are a manifestation of the partial double bond of the C-NO_2 bond. The optimized geometries for the internal rotation around the C-N bond at dihedral angles 0°, 40° and 80° are presented in Table 4.8 and 4.9. The internal rotation of the amine group significantly affects the C-NH_2 bond whereas the nitro group rotation does not have a pronounced effect on the C-NO_2 bond, which is evident from the C_1-N_1 and C_4-N_2 bond values from the Table.

The C-NH_2 bond loses its partial double bond character due to the decrease in the ring-amine group conjugative interaction when the geometry changes from planar to per-

Table 4.8: Optimized Molecular parameters for methylamine rotation in MNA

Parameter	HF			B3LYP			MP2		
	0	40	80	0	40	80	0	40	80
C1-C2	1.40	1.40	1.39	1.41	1.41	1.40	1.40	1.40	1.40
C1-N1	1.35	1.38	1.40	1.36	1.38	1.41	1.37	1.39	1.41
C4-N2	1.44	1.44	1.45	1.45	1.45	1.46	1.46	1.46	1.46
N2-O1	1.19	1.19	1.19	1.23	1.23	1.23	1.24	1.24	1.24
N1-C7	1.44	1.45	1.46	1.44	1.46	1.47	1.37	1.39	1.41
N1-H5	0.99	0.99	0.99	1.00	1.01	1.01	1.00	1.01	1.01
C6-C1-C2	118.45	118.43	118.84	118.45	118.41	118.91	118.50	118.61	119.10
C4-N2-O1	118.14	118.04	117.87	117.84	117.80	117.61	117.98	117.87	117.73
C2-C1-N1	121.75	121.38	119.23	121.85	121.04	118.81	121.89	121.35	119.10
C3-C4-N2	119.68	119.56	119.27	119.24	119.24	118.91	119.70	119.56	119.22
O1-N2-O2	123.81	123.95	124.18	124.37	124.44	124.72	124.13	124.28	124.49
C5-C6-C1-C2	0.0	-0.7	-1.34	1.26	-3.27	-2.33	0.0	-0.55	-0.67
C3-C4-N2-O1	0.0	-0.36	-1.03	-9.96	-4.46	-13.14	0.0	-0.32	-0.83

Table 4.9: Optimized Molecular parameters for nitro rotation in MNA

Parameter	HF			B3LYP			MP2		
	0	40	80	0	40	80	0	40	80
C1-C2	1.40	1.40	1.39	1.41	1.41	1.41	1.40	1.40	1.40
C1-N1	1.36	1.36	1.37	1.36	1.37	1.38	1.38	1.38	1.39
C4-N2	1.44	1.44	1.46	1.45	1.45	1.47	1.46	1.45	1.46
N2-O1	1.19	1.19	1.19	1.23	1.23	1.23	1.24	1.24	1.24
N1-C7	1.44	1.44	1.44	1.45	1.45	1.45	1.45	1.45	1.45
N1-H5	0.99	0.99	0.99	1.00	1.00	1.00	1.00	1.01	1.01
C6-C1-C2	118.52	118.56	118.46	118.45	118.46	118.36	118.42	118.62	118.65
C1-N1-H5	116.30	115.65	114.57	117.33	117.03	115.82	113.86	113.65	113.13
C1-N1-C7	123.97	123.35	122.34	124.68	124.38	123.19	120.72	120.50	120.00
C2-C1-N1	121.99	122.05	122.23	121.76	121.75	121.91	121.81	121.80	121.83
C3-C4-N2	119.68	119.26	119.45	119.66	119.54	119.13	119.25	119.16	118.86
O1-N2-O2	124.16	124.61	125.11	123.81	124.33	124.95	124.36	124.94	125.30
C5-C6-C1-C2	0.0	-0.3	0.0	0.0	-1.2	-0.8	-2.8	-0.7	-0.8

pendicular with respect to the methylamine group. Tilting of the C-N bond is also observed for the amine group, but not for the nitro group. The length of the N_1-C_7 bond increases on rotation from 0° to 90° to avoid steric interference of the methyl hydrogens with the ortho hydrogens of the benzene ring. Torsional barriers predicted with MP2 theory were generally lower than B3LYP and HF calculations, except for the o-nitro group where MP2 predicted the highest barrier. MP2 theory, however, was found to perform poorly in the

determination of the optimized conformation for MNA; a problem we attribute to the limitations of MP2 in dealing with molecules with significant resonance structure. These results show that electron correlation has a significant effect on the barriers to rotation in molecules with steric and conjugative interactions. The magnitude of the barriers are useful in understanding the strength of the intramolecular interactions and reaction mechanism for the decomposition of explosives.

4.4 DNP & NTO

4.4.1 Equilibrium Structures

Equilibrium parameters for NTO and DNP are listed in Table 4.10 and Table 4.11 respectively and a schematic of DNP and NTO is shown in Figure 4.9. The optimized structures of DNP and NTO at HF, B3LYP and MP2 levels of theories are all planar with respect to the nitro groups. All the structural parameters from the *ab initio* methods and the experiment [173] agree well with each other. No experimental structure exists for DNP to make a comparison.

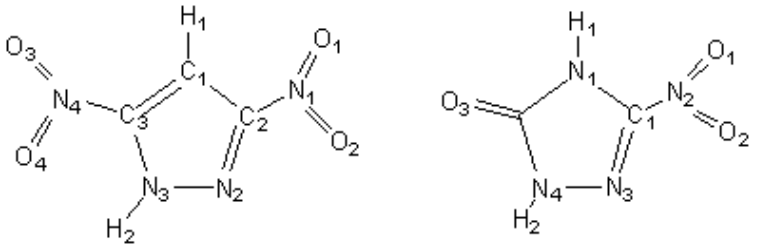

Figure 4.9: Molecular structure of DNP (left) and NTO (right)

4.4.2 Torsional barriers

The torsional barriers determined for the nitro groups in both the compounds are presented in Figures 4.10, 4.11 and 4.12. The predicted barriers to rotation around the C-N

Table 4.10: Molecular parameters for NTO

Parameter	B3LYP	MP2	HF	Exp [173]
Bond Lengths (Å)				
N1-C1	1.365	1.359	1.359	1.348
C1-N3	1.291	1.307	1.254	1.283
N3-N4	1.359	1.361	1.352	1.358
N4-C2	1.397	1.393	1.370	1.367
C2-N1	1.403	1.405	1.381	1.377
C2-O3	1.205	1.211	1.185	1.220
C1-N2	1.452	1.448	1.448	1.454
N2-O1	1.215	1.226	1.175	1.217
N2-O2	1.230	1.236	1.190	1.217
Angle(Degree)				
O1-N2-O2	126.8	127.1	127.2	126.5
O1-N2-C1	118.4	118.0	118.1	116.5
C1-N3-N4	103.4	102.3	103.8	102.7
N3-N4-C2	114.5	115.3	113.7	112.8
N4-C2-O3	129.5	129.9	129.3	128.8
N4-C2-N1	100.7	100.4	101.6	103.7
C2-N1-C1	107.7	108.0	106.8	105.5

bond in DNP and NTO are presented in Table 4.12.

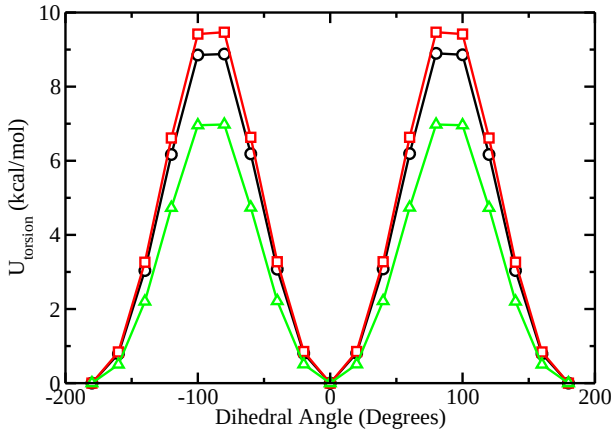

Figure 4.10: Torsional barrier for rotation around N4-C3 bond in DNP. Prediction of B3LYP/6-31G+(d,p) calculations(black), MP2/6-31G+(d,p)(green) and HF/6-31G+(d,p)(red).

Table 4.11: Molecular parameters for DNP

Parameter	B3LYP	MP2	HF
Bond Lengths(Å)			
C1-C2	1.376	1.388	1.355
C2-N2	1.360	1.353	1.343
N2-N3	1.326	1.340	1.303
N3-C3	1.329	1.343	1.297
C3-C1	1.405	1.402	1.405
C2-N1	1.442	1.444	1.435
N1-O1	1.219	1.229	1.180
N1-O2	1.229	1.234	1.190
C3-N4	1.462	1.458	1.449
N4-O3	1.226	1.233	1.189
N4-O4	1.216	1.227	1.179
Angle(Degree)			
C1-C2-N2	108.2	108.8	120.86
C2-N2-N3	112.2	111.5	119.59
N2-N3-C3	104.0	105.0	120.64
N3-C3-C1	113.7	113.5	119.99
C1-C2-N1	131.3	130.7	120.39
C2-N1-O1	117.4	117.1	118.50
C1-C3-N4	125.9	125.7	119.59
C3-N4-O3	115.4	115.3	121.89

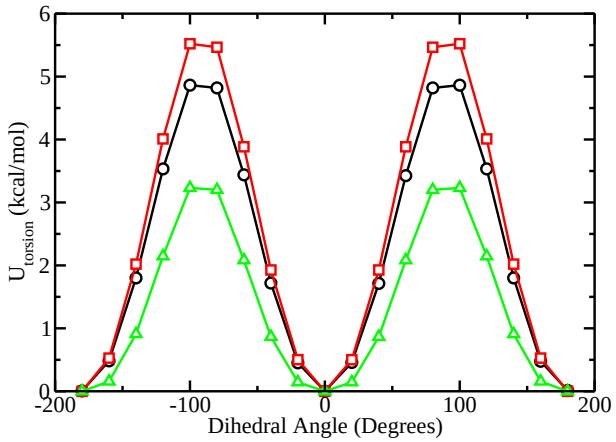

Figure 4.11: Torsional barrier for rotation around C2-N1 bond in DNP. Prediction of B3LYP/6-31G+(d,p) calculations(black), MP2/6-31G+(d,p)(green) and HF/6-31G+(d,p)(red).

For DNP, the predicted barrier to rotation around the N4-C3 bond is higher than the rotation around N1-C2 bond. This is due to the location of the nitro group in each case. The nitro group at C3 is located adjacent to the amide hydrogen and involves in hydrogen bonding whereas the nitro group at C2 has no amide hydrogens to bond.

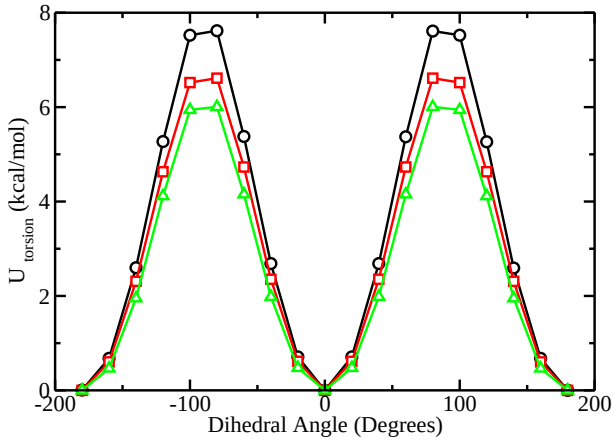

Figure 4.12: Torsional barrier for nitro group (O-N-C-N dihedral) in NTO. Prediction of B3LYP/6-31G+(d,p) calculations(black), MP2/6-31G+(d,p)(green) and HF/6-31G+(d,p)(red).

Table 4.12: Rotational barriers in kcal/mol for DNP and NTO at 6-31G+(d,p) basis set.

Functional Group	B3LYP	MP2	HF
DNP			
Nitro(N4-C3)	8.88	6.98	9.47
Nitro(N1-C2)	4.82	3.23	5.52
NTO			
Nitro	7.60	6.00	6.60

4.5 Conclusion

Optimized structures and barriers to rotation of various substituents for DNAN, MNA, DNP and NTO have been determined. Calculations were performed at the HF, B3LYP and MP2 levels of theory with the 6-31G+(d,p) basis set to identify the effects of electron

correlation. Torsional barriers predicted with MP2 theory were generally lower than B3LYP and HF calculations, except for the o-nitro group where MP2 predicted the highest barrier. MP2 theory, however, was found to perform poorly in the determination of the optimized conformation for MNA; a problem we attribute to the limitations of MP2 in dealing with molecules with significant resonance structure. The rotational barrier data are used for developing force fields for the energetic materials of interest.

Chapter 5

Energetic Materials: Condensed Phase Properties

5.1 Introduction

Energetic materials often include explosives, propellants and pyrotechnics. The six energetic compounds studied in this work are 2,4-dinitroanisole (DNAN), N-methyl-p-nitroaniline (MNA), Dinitropyrazole (DNP), Nitrotriazolone (NTO), 1-methyl-2,4,5-trinitroimidazole (MTNI) and 1,3,5-triamino-2,4,6-trinitrobenzene (TATB) whose structures are shown in Figure 5.1. As seen in the structures, each compound is a hydrocarbon that possesses atleast one nitro group which is a characteristic of high-energy compounds. NO_2-X are

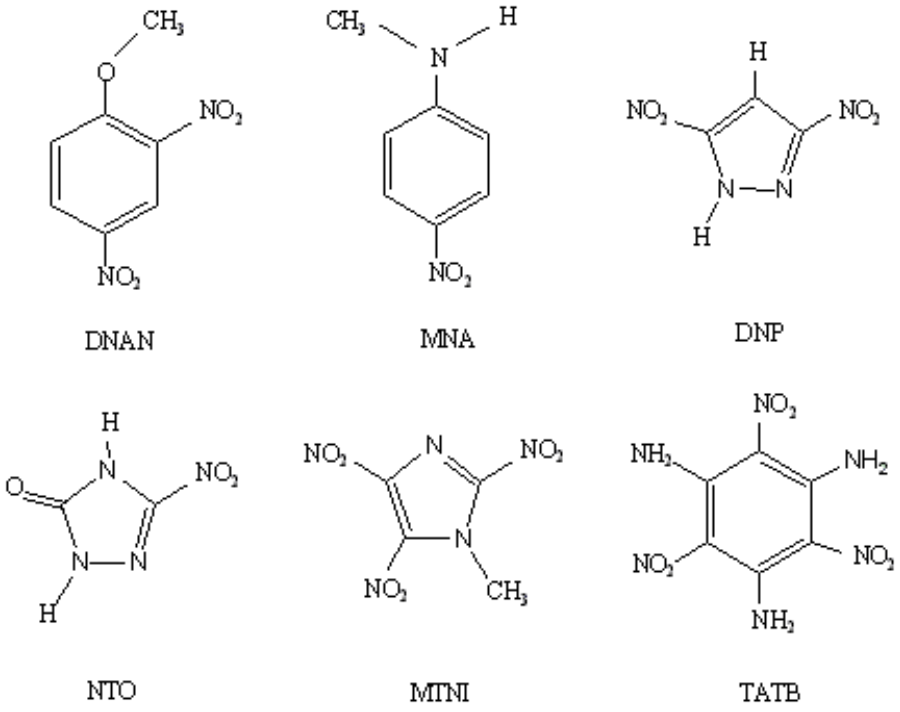

Figure 5.1: Molecular Structure of the energetic materials studied in this work

relatively easy to break resulting in nitrogen gas and oxygen that helps in oxidizing carbon and hydrogen to CO, CO_2 and H_2O.

Of all the compounds listed here, DNAN is one of the oldest IM compounds to be employed by the military community with its usage dating back to world war II [174, 175]. There was renewed interest in DNAN when Picatinny Arsenal explosive (PAX) formulations [176, 177] were designed in the mid 80's as first high performance insensitive munitions. MNA was used as an additive in these formulations to improve their mechanical and thermal properties. MNA is also used as a stabilizer to increase the sevice-life of smoke propellants [178]. TATB and NTO found use in modern polymer-bonded explosives (PBX) [179] where they are bound in a matrix of a synthetic polymer to make them more insensitive. TATB also finds use as a detonator in nuclear warheads. DNP and MTNI are relatively new insensitive energetic materials which are yet to be incorporated into munitions. All the compounds discussed here are reported to be less sensitive than RDX, HMX and TNT [180–183].

Common energetic materials such as trinitrotoluene (TNT), cyclotrimethylenetrinitramine (RDX), sym-cyclotetramethylene-tetramitramine (HMX) and hexanitrohexaazaisowurtzitane (CL-20) have been studied extensively and numerous physical property are available. For TNT, RDX, HMX and CL-20, aqueous solubility have been measured over a temperature range of 275-333K [184–186]. Critical temperatures for RDX and HMX [187] and vapor pressures for RDX, TNT and HMX [188–192] have been measured experimentally. Physicochemical properties such as octanol-water partition coefficients and Henry's law constant have also been reported for RDX, TNT, HMX and CL-20 [184, 193, 194].

In cases where multiple data sets exist for energetic materials, significant differences have

been observed between some of the data sets. For example, reported values of the aqueous solubility for TNT may vary by as much as a factor of 2 [195]. For the energetic materials of interest, very few properties measured from experiment are available. For DNAN and MNA, octanol-water partition coefficients, Henry's law constants and aqueous solubility have been reported [196, 197]. Aqueous solubility have been measured for NTO over the temperature range 284.65 to 367.55 K [198]. The lack of consistent physical property and the acute need for such data for new energetic materials that may be used to provide prediction of the environmental fate drives the development of force fields for the compounds of interest.

5.2 Force Field

Initial estimates of the partial charges for each molecule were determined through a CHELPG analysis by fitting to a electrostatic potential determined from *ab initio* calculations performed at the HF/6-31G+(d,p) level of theory and basis set with Gaussian 03. Four different models were derived for DNAN and MNA by scaling the initial charges by different factors to find the best set of partial charges that reproduced its octanol-water partition coefficient measured from experiment. The rescaling factors were 1(initial charges), 0.94 and 0.90 for IC, 6C and 10C models respectively. Once the best charge model was chosen, the same charge scheme was used for the rest of the compounds. The charges for each functional group in each charge scheme for DNAN and MNA are listed in Table 5.1 and 5.2 respectively.

For DNAN and MNA, united-atom (UA) force fields are developed where, all hydrogens bonded to carbon atoms are combined with carbon to form a single interaction site (a pseudo atom) centered on the nucleus of the carbon atom. For all other compounds, an explicit hydrogen force field was constructed. For the united atom force field, Lennard-Jones

Table 5.1: Partial charges for DNAN

Site	IC	6C	10C
CH-(aro)	0	0	0
C-(O)	0.160	0.150	0.144
O-(CH_3)	-0.430	-0.402	-0.387
CH_3	0.270	0.252	0.243
C-(NO_2)	0.120	0.112	0.108
N-(O)	0.820	0.768	0.738
O-(N)	-0.470	-0.440	-0.423

Table 5.2: Partial charges for MNA

Site	IC	6C	10C
CH-(aro)	0	0	0
C-(NH)	0.200	0.187	0.180
N-(CH_3)	-0.780	-0.730	-0.702
CH_3	0.250	0.234	0.225
C-(NO_2)	0.140	0.131	0.126
N-(O)	0.760	0.711	0.684
O-(N)	-0.480	-0.449	-0.432
H-(N)	0.390	0.365	0.351

parameters σ and ε for each interaction site were transferred from analogous compounds previously parametrized in the development of the TraPPE-UA force field [199–202].

In the explicit hydrogen version for DNP, NTO, MTNI and TATB, the Lennard-Jones parameters for the nitro group were transferred from the explicit model of nitrobenzene reported in the recent work by Siepmann *et al.* [203] and the rest from the TraPPE force field [204] for five-membered rings. The aromatic ring was modeled as explicit hydrogen wherever necessary. The parameters for the ring were transferred from explicit model of benzene [203]. The Lennard-Jones parameters and partial charges are listed in the Appendix. The non-bonded interactions were represented by the Lennard-Jones potential, the bond vibration and bond bending by a harmonic potential and the torsion by a fourier cosine series as described in Chapter 3.

5.3 Thermophysical Properties

5.3.1 Partition Coefficients

Octanol-water Partition Coefficient

The octonol-water partition coefficient ($\log K_{ow}$) is related to the free energy of transfer of the solute between water and water-saturated octanol phase by

$$\Delta G = -2.303 RT \log K_{ow} \tag{5.1}$$

The direct calculation of free energies of transfer between water and octanol phases is computationally difficult, but possible for small solutes using Gibbs ensemble Monte Carlo simulation [205]. For larger molecules, however, direct calculation of ΔG is not possible due to the vanishingly small probability of successfully transfering solutes between phases. Since the Gibbs free energy is a state function, the free energy difference is independent of the path and therefore ΔG can be computed via an alternate thermodynamic path as shown in Figure 5.2 where solute A is slowly transformed to solute B independently in water and water-saturated octanol phases. This path provides a means for calculating the relative Gibbs free energy of transfer, which is defined by

$$\Delta\Delta G = \Delta G_{Tr}B - \Delta G_{Tr}A = \Delta G_{Tr(oct)}(A \rightarrow B) - \Delta G_{Tr(w)}(A \rightarrow B) \tag{5.2}$$

where $\Delta G_{Tr(oct)}$ and $\Delta G_{Tr(w)}$ are the free energies associated with the transformation of solute A to solute B in the water-saturated 1-octanol solution and water respectively. The

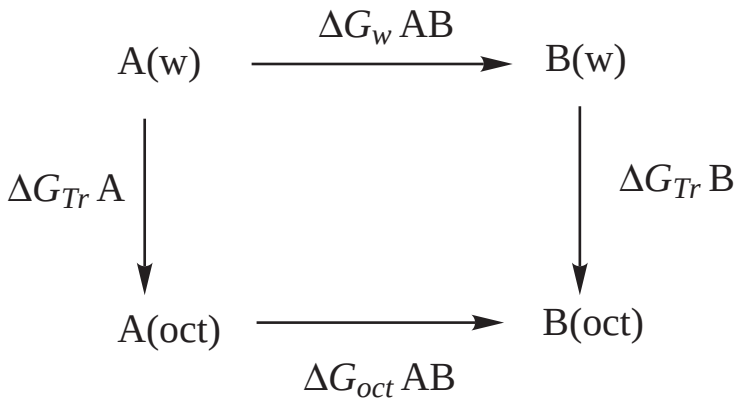

Figure 5.2: Thermodynamic path for octanol-water partition coefficient

relative partition coefficient is now expressed as

$$\Delta \log K_{ow} = \frac{-\Delta\Delta G_{Tr} AB}{2.303RT} \tag{5.3}$$

The most common method to calculate free energy differences is the Free Energy Perturbation (FEP) technique [37, 38]. The FEP method involves slowly transforming solute A to solute B (either A or B is the compound of interest) by scaling the interaction potential through

$$U(\lambda) = \lambda U_B + (1 - \lambda)U_A \tag{5.4}$$

where λ is the scaling parameter and has values between 0 an 1. The FEP method allows for the calculation of the relative Gibbs free energy of transfer $\Delta\Delta G$, from which the relative octanol-water partition coefficient ($\Delta \log K_{ow}$) is obtained. The absolute partition coefficient of target molecule B is then calculated from the reference molecule A by

$$\log K_{ow}(B) = \Delta \log K_{ow} + \log K_{ow}(A) \tag{5.5}$$

Henry's Law Constant

Henry's law constant expressed in terms of solvation energy of a solute in water as derived by Lin *et. al.* [206] is given by

$$\log_{10} H_i = \frac{\Delta G^{*sol}_{i/W}}{RT \ln 10} + \log_{10} \frac{RT\rho^0_w}{N_A} \tag{5.6}$$

where $\Delta G^{*sol}_{i/w}$ is the solvation free energy of species i in solvent water, ρ^w_0 is the number density of pure water and N_A is Avagadro's number. The solvation free energy of solute i in water or the hydration free energy is the free energy associated with the transfer of solute from vacuum to water. Similar to the octanol-water partition coefficient, a thermodynamic path is constructed, but the water-saturated octanol phase is replaced by the vacuum phase. Solute i is transformed to j in both water and vacuum phases. The relative Henry's law constant can be derived by using Eq. 5.6 and the equation for the Henry's law constant for solute j

$$\log_{10} H_j = \frac{\Delta G^{*sol}_{j/W}}{RT \ln 10} + \log_{10} \frac{RT\rho^0_w}{N_A} \tag{5.7}$$

Subtracting Eq. 5.6 from Eq. 5.7, we obtain an expression for relative Henry's law constant

$$\Delta \log_{10} H = \frac{\Delta G^{*sol}_{j/W} - \Delta G^{*sol}_{i/W}}{2.303RT} \tag{5.8}$$

The second term in both Eq 5.6 & 5.7 cancels out since the density of pure water is a constant at any specific temperature. Using a thermodynamic cycle similar to the one used

for the calculation of octanol-water partition coefficients, Equation 5.8 can be written as

$$\Delta \log_{10} H = \frac{\Delta G_{Tr(w)}(i \rightarrow j) - \Delta G_{Tr(vac)}(i \rightarrow j)}{2.303RT} \tag{5.9}$$

The absolute Henry's law constant of solute j is calculated from the knowledge of the Henry's law constant for the reference solute i

$$\log H(j) = \Delta \log H + \log H(i) \tag{5.10}$$

Simulation Methodology

The FEP technique as implemented in the NAMD simulation engine [118] was used in the NPT ensemble for computing the partition coefficients. NAMD uses a dual topology scheme [207,208], where both the initial and the final states are defined concurrently. Each FEP simulation involves transformation of a solute to the energetic material of interest or vice versa. The choice of initial solutes depends on structural similarity with the energetic material and availability of experimental partition coefficient data. The solutes used are listed in the results section. For each solute of interest, three FEP simulations were performed at 298 K and 1.013 bar; one for the water phase, one for the water-saturated 1-octanol solution and the last for the vacuum phase. The mole fraction of water in the octanol phase was set to the experimental value of 0.255 [209].

Simulations were also run at 308 and 318 K for DNAN and MNA to investigate the temperature dependence of the partition coefficients. Free energy perturbation was carried out over 20 windows, where the starting six and the ending six windows were unequally spaced with very small increments to improve convergence at the end points. This methodology is

known to avoid the end-point catastrophe [210,211] resulting from the appearing and vanishing atoms. λ was increased from 0 to 0.1 and 0.9 to 1 in the following increments: 10^{-6}, 10^{-5}, 10^{-4}, 10^{-3}, 0.01, 0.05 and 0.95, 0.99, 0.999, 0.9999, 0.99999. The windows between 0.1 to 0.9 were equally spaced at 0.1 increments. A non-bonded cutoff of 14 Å was used for all Lennard-Jones interactions, while the Particle Mesh Ewald (PME) technique [212] was used to calculate all coulombic interactions. The Langevin piston Nosé-Hoover method [119,120] was used to control pressure and temperature.

For calculations in vacuum, an isolated hybrid molecule was simulated without periodic boundary conditions, and a damping coefficient of 10 ps^{-1} for Langevin temperature control. The vacuum simulation was carried out for a total of 2.4 ns with 400 ps of equilibration and 2 ns of sampling. In water and octanol phases, FEP calculations were run for a total of 6 ns with 100 ps of equilibration and 100 ps of sampling for each window. Three iterations were performed in each phase and the values averaged for the net free energy of transfer which was used to calculate the partition coefficients. Both forward and reverse perturbations were run for each transformation to verify convergence of the FEP calculations. A double-wide sampling method [213] was used, where the free energy difference for each window, i.e., λ_i to λ_{i+1} (forward)and λ_{i+1} to λ_i (reverse) was monitored to test for self-consistency and hysteresis (difference in the free energy change resulting from forward and reverse perturbation) of each simulation.

5.3.2 Vapor Liquid Equilibria

Three methods were used to determine the vapor-liquid equilibria for DNAN and MNA: Gibbs ensemble Monte Carlo (GEMC) [214], Grand Canonical Histogram-Reweighting Monte Carlo (GCHRMC) [61, 64, 117] and Gibbs-Duhem integration [62]. GEMC was

selected initially because it provides a direct calculation of phase coexistence. However, the Gibbs ensemble methodology requires frequent particle removals from one phase and insertion into the other, also known as 'swaps'. Despite the use of state of the art configurational-bias methods [113], it was unable to achieve a more than a fraction of a percent of accepted swap moves. Additional calculations were performed with GCMC coupled with histogram reweighting technique [64]. With these calculations, it was possible to determine the vapor-liquid equilibria in the region near the critical point but this methodology also was problematic at lower temperatures due to the difficulty of molecule insertion in a dense liquid phase. The solution to the problematic particle insertion move was to use Gibbs-Duhem integration [62].

Simulation Methodology

The initial coexistence point in this work was determined by grand canonical histogram reweighting Monte Carlo simulations for DNAN and MNA and PVT calculations through NPT molecular dynamics simulation near the critical point for the rest of the compounds. The insertion of molecules in the GCMC simulations was enhanced with the application of the coupled-decoupled configurational-bias Monte Carlo method. The ratios of attempted moves were set to 60% particle insertions/deletions, 10% configurational-bias regrowths, 15% translations and 15% rotations. A non-bonded cutoff of 14 Å with no tail corrections was used. For PVT calculations, isotherms were generated at different pressures near the critical point and densities estimated. One isotherm, where liquid and gas coexists at a specific pressure is chosen as the initial coexistence (P,T) condition. Treating this coexistence point as the initial state, Gibbs-Duhem integration was performed with NPT MD simulations to generate the coexistence densities.

Given an estimate of the saturation pressure, NPT MD simulations are performed simultaneously starting from the initial coexistence point for both liquid and vapor phases to determine the coexistence densities and heat of vaporization. Averages of volume and energies are collected from gas and liquid simulations running at predictor pressure. The molar enthalpy of each phase is calculated from the average volume and energy using,

$$H =< U > +P < V > \tag{5.11}$$

where $< U >$ and $< V >$ represent the energy and volume average respectively and P is the pressure. The difference in molar enthalpy is then used to predict the integrand for Gibbs-Duhem integration which is given by,

$$f = -\Delta H/\beta P \Delta V \tag{5.12}$$

where β=1/T and ΔV is the difference in molar volumes of the gas and liquid phase.

The predictor-corrector formulas use the integrand to predict new pressure (corrected pressure) using the predictor-corrector formulas and the simulation continues with this new pressure. This pressure is the vapor pressure at a particular temperature and the volume averages from this new pressure simulation are used to estimate the coexistence densities. This process is repeated for different temperatures along the saturation line to estimate coexistence densities and vapor pressure. The Langevin piston Nosé-Hoover method was used for temperature and pressure control. A non-bonded cutoff of 14 Å was used for all the simulations. Subsequent gas and liquid simulations starting from the initial coexistence point were run at low temperatures with 300 molecules each for 1 ns each with 300 ps of

Table 5.3: Octanol-water partition coefficients for DNAN and MNA at 298 K

Model	DNAN	MNA
IC	0.53	0.90
6C	1.64	2.13
10C	1.94	2.52
Exp	1.61	2.10

equilibration and 700 ps of sampling.

5.4 Results and Discussion

5.4.1 Parameter Optimization

Preliminary free energy and vapor-liquid equilibria calculations were run for DNAN and MNA to find the best set of partial charges that reproduced the octanol-water partition coefficients and boiling point measured from experiment [196, 197, 215]. The octanol-water partition coefficients of DNAN and MNA were predicted for the IC, 6C and 10C models using anisole and aniline as the reference solutes at 298 K. The experimental octanol-water partition coefficients of anisole and aniline are 2.11 and 0.90 respectively [216]. The TraPPE force field [199–202] was used to represent anisole and aniline. The predicted partition coefficients for each model of DNAN and MNA along with the experimental value are shown in Table 5.3.

As seen from the table, the value of the octanol-water partition coefficients increase when the magnitude of the charges are scaled down. This is expected because reduction in the partial charges of oxygens of the nitro group reduces electrostatic interactions between them and the hydrogens of water molecules. This also decreases the solubility of the molecule in water while enhancing it in 1-octanol. So DNAN and MNA prefer partitioning into the water phase thereby decreasing the octanol-water partition coefficient. The 6C model

Table 5.4: Phase coexistence properties for DNAN and MNA at 298 K

	DNAN			MNA		
Properties	IC	6C	10C	IC	6C	10C
T_c(K)	942.25	885.42	881.45	832.41	770.75	757.69
ρ_c(kg/m^3)	408.35	410.20	376.93	346.42	324.50	386.72
P_c(bar)	43.29	37.36	39.14	48.67	37.70	39.62
T_{nb}(K)	663.16	620.82	613.70	556.94	522.76	515.11
T_b at 12mm Hg[a]	495	461.04	460	-	-	-

[a] Exp: 479 K

predicts octanol water partition coefficient within +0.03 log units from the experiment. So 6C model was the best charge scheme that reproduced the measured octanol-water partition coefficients.

The phase coexistence properties determined for all the models, IC, 6C and 10C of DNAN and MNA are listed in Table 5.4. The only experimental data with respect to phase coexistence is the boiling point of DNAN at 12 mm Hg [215]. The IC and 6C models predict boiling points about 3.5% higher and lower from the experiment respectively. Since both IC and 6C models of DNAN produced satisfactory results, the deciding factor was the predicted octanol-water partition coefficients. So the 6C model was chosen as the best charge scheme and this was adapted for other compounds too. All the calculations were then continued with the 6C model charge scheme, i.e., the initial *ab initio* charges were reduced by 6%.

5.4.2 Partition Coefficients

The reference solutes used to calculate the partition coefficients of the energetic materials are listed in Table 5.5 along with their octanol-water partition coefficients and Henry's law constants. Since no direct Henry's law constant has been reported in literature for pyrazole, Henry's law constant was calculated from experimental vapor pressure and solubility of

Table 5.5: Partition Coefficients for reference solutes from experiment at 298 K

Molecule	$\log K_{ow}$	$\log H$
Nitrobenzene[a]	1.85	-3.01
Pyrazole[b]	0.02	-7.12
Imidazole[c]	-0.08	-7.86

a [12, 219] *b* [220] *c* [221]

pyrazole at 298 K. Henry's law constant is given by

$$H = \frac{p}{S} \tag{5.13}$$

where p is the vapor pressure and S is the aqueous solubility. The vapor pressure of pyrazole at 298 K is 3.638 Pa [217] and solubility in water at 298 K is 19.4 mol/kg of water [218].

The net free energies associated with each transformation in water, water saturated octanol and vacuum are reported in Table 5.6. Plots for the computed free energies with respect to the scaling parameter λ in each phase for each transformation are shown in the Figure 5.3, 5.4, 5.5 and 5.6. The free energies in the plot are averages from three iterations. The results of the convergence calculations are shown in Table 5.7 and Table 5.8 for MNA and NTO respectively, where $i \rightarrow j$ denotes the forward perturbation and $j \rightarrow i$ the reverse perturbation. MNA and NTO convergence simulations are representative of other compounds too. The magnitude of the incremental free energies at each λ increment and the net free energy change for the forward and reverse FEP simulations agree well with each other indicating negligible hysteresis. The change in sign is due to the difference in the direction of simulation.

Octanol-water partition coefficients and Henry's law constants were calculated from the relative free energies determined from the molecular dynamics simulations, using exper-

Table 5.6: Free energies predicted in water, water-saturated octanol and vacuum. All ΔG are in kcal/mol.

Transformation(water)	$\Delta G^1_{Tr(w)}$	$\Delta G^2_{Tr(w)}$	$\Delta G^3_{Tr(w)}$	Average
Nitrobenzene - DNAN(1)	-16.68	-16.45	-16.66	-16.60±0.12
Nitrobenzene - MNA(2)	-1.60	-1.70	-1.82	-1.71±0.11
Pyrazole - DNP(3)	83.75	83.64	84.24	83.87±0.31
Pyrazole - NTO(4)	7.16	6.56	6.42	6.71±0.39
Imidazole - MTNI(5)	-84.14	-83.38	-83.97	-83.83±0.39
Nitrobenzene - TATB(6)	64.26	65.54	64.55	64.78±0.67
Water saturated 1-octanol	$\Delta G^1_{Tr(oct)}$	$\Delta G^2_{Tr(oct)}$	$\Delta G^3_{Tr(oct)}$	Average
1	-16.15	-16.75	-16.20	-16.37±0.33
2	-1.99	-1.91	-1.86	-1.92±0.06
3	85.16	85.62	84.91	85.23±0.36
4	9.07	9.56	9.62	9.41±0.30
5	-82.80	-83.10	-84.24	-83.38±0.75
6	61.19	61.63	62.63	61.89±0.65
Vacuum	$\Delta G^1_{Tr(vac)}$	$\Delta G^2_{Tr(vac)}$	$\Delta G^3_{Tr(vac)}$	Average
1	-11.46	-11.43	-11.41	-11.43±0.02
2	-0.52	-0.52	-0.52	-0.52±0
3	82.85	82.86	82.85	82.85±0
4	13.50	13.51	13.51	13.51±0
5	-81.97	-82.11	-81.74	-81.94±0.18
6	51.88	51.88	51.89	51.88±0.01

imental values of $\log K_{ow}$ and $\log H$ for the reference solutes. The partition coefficients predicted are presented in Table 5.9, with values predicted using COSMOtherm [222], EPI Suite [223] and experiment [196, 197] for comparison. The predicted Henry's law constants are listed in Table 5.10.

The EPI Suite program uses an atom/fragment contribution method for estimating the partition coefficients. The partition coefficients from simulation are calculated by averaging the forward perturbation results. The octanol-water partition coefficients predicted by FEP simulations are within ±0.1 log units of experiment for both DNAN and MNA. While the predictions of the EPI Suite for octanol-water partition coefficients are also in good agreement with the experiment, COSMOtherm predictions have unsigned errors of

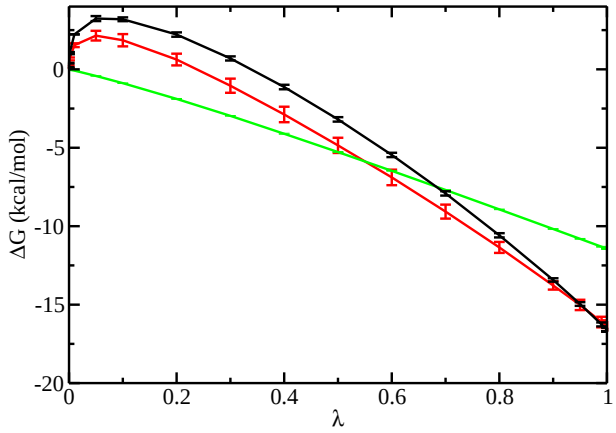

Figure 5.3: Free energy change for transformation of nitrobenzene to DNAN in water (black); octanol (red) and vacuum (green) at 298 K and 1.013 bar. Error bars indicate standard deviation of data.

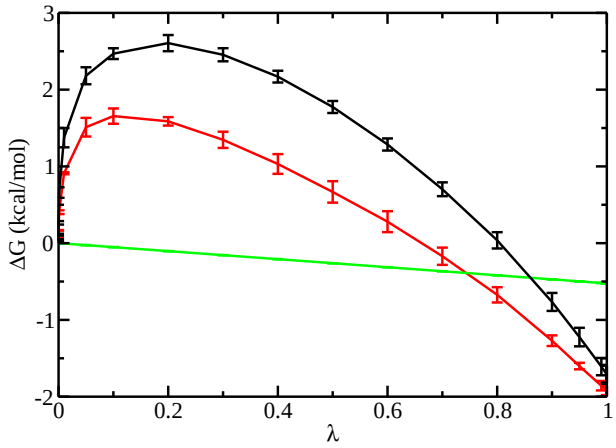

Figure 5.4: Free energy change for transformation of nitrobenzene to MNA in water (black); octanol (red) and vacuum (green) at 298 K and 1.013 bar. Error bars indicate standard deviation of data.

0.24 (DNAN) and 1.3 (MNA) log units when compared to experiment. Altough KOWWIN (octanol-water partition coefficient prediction module in EPI) was developed with a training set of about 2500 molecules and been tested on a dataset of 10200 compounds, it might give poor predictions for energetic materials since the training set does not include many explosive components. COSMOtherm predicts values that deviate significantly from predictions of both molecular simulations and the EPI Suite.

The Henry's law constant predicted from molecular dynamics simulations for MNA

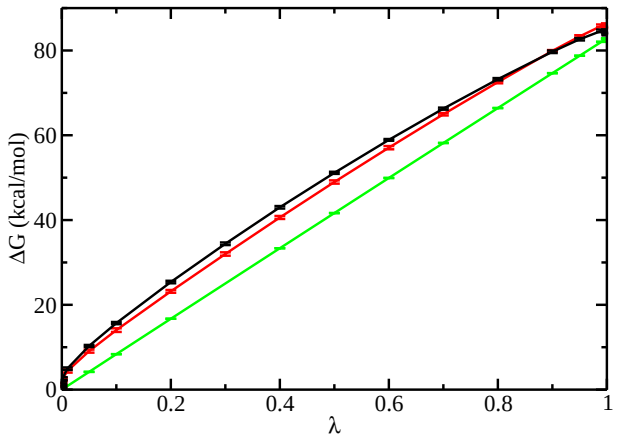

Figure 5.5: Free energy change for transformation of pyrazole to DNP in water (black); octanol (red) and vacuum (green). Error bars indicate standard deviation of data.

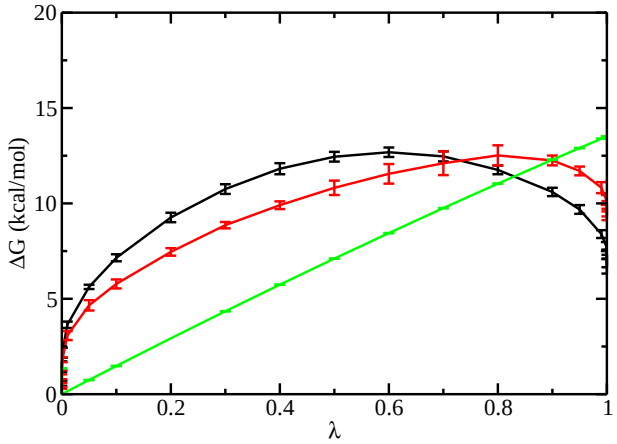

Figure 5.6: Free energy change for transformation of pyrazole to NTO in water (black); octanol (red) and vacuum (green). Error bars indicate standard deviation of data.

Table 5.7: Computed free energies (kcal/mol) from FEP simulations for MNA.

	Water		Octanol		Vacuum	
i,j	$i \to j$	$j \to i$	$i \to j$	$j \to i$	$i \to j$	$j \to i$
0,0.1	2.46	-2.11	1.59	-1.51	-0.05	0.05
0.1,0.2	0.13	-0.13	-0.04	0.05	-0.05	0.05
0.2,0.3	0.15	-0.15	-0.25	0.21	-0.05	0.05
0.3,0.4	0.28	-0.28	-0.33	0.32	-0.05	0.05
0.4,0.5	0.39	-0.38	-0.36	0.38	-0.05	0.05
0.5,0.6	0.48	-0.48	-0.38	0.44	-0.05	0.05
0.6,0.7	0.58	-0.57	-0.44	0.49	-0.05	0.05
0.7,0.8	0.66	-0.66	-0.50	0.52	-0.05	0.05
0.8,0.9	-0.80	0.77	-0.57	0.53	-0.05	0.05
0.9,1.0	-0.94	0.92	-0.65	0.68	-0.05	0.05

Table 5.8: Computed free energies (kcal/mol) from FEP simulations for NTO.

	Water	
i, j	$i \rightarrow j$	$j \rightarrow i$
0,0.1	6.93	-6.97
0.1,0.2	2.05	-2.00
0.2,0.3	1.48	-1.58
0.3,0.4	1.07	-1.15
0.4,0.5	0.65	-0.63
0.5,0.6	0.23	-0.22
0.6,0.7	-0.24	0.11
0.7,0.8	-0.68	0.57
0.8,0.9	-1.14	1.21
0.9,1.0	-3.80	4.46

Table 5.9: Octanol-water partition Coefficients predicted at 298 K by various methods

Molecule	Sim	Exp	Cosmo	EPI
DNAN	1.68	1.61	1.92	1.70
MNA	2.00	2.10	0.80	2.01
DNP	-0.97	-	0.37	-0.30
NTO	-1.99	-	-1.19	-1.56
MTNI	-0.40	-	1.64	0.05
TATB	-1.86	-	4.74	-1.28

Table 5.10: Henry's law constants predicted at 298 K by various methods

Molecule	Sim	Exp	EPI
DNAN	-6.80	-3.25	-4.91
MNA	-3.88	-3.60	-6.17
DNP	-6.37	-	-8.62
NTO	-11.99	-	-10.77
MTNI	-9.24	-	-9.69
TATB	-12.56	-	-14.45

agrees closely with the experiment while DNAN Henry's law constant is under-predicted significantly. For DNAN, the source of error is unclear, since the same model was used to successfully predict $\log K_{ow}$ and the boiling point to within 10% of experiment. Although the relative partitioning between octanol and water was predicted correctly, it is possible that the model over-predicts the solubility of DNAN in water, leading to a reduced value

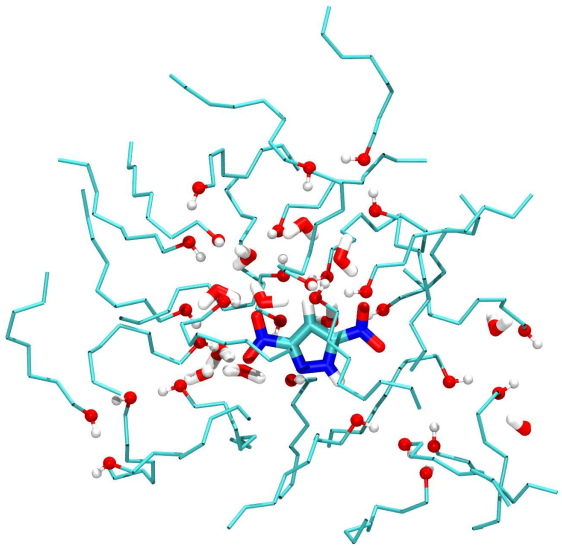

Figure 5.7: DNP inside a 10 Å solvation shell of water-saturated octanol

of the Henry's law constant. The EPI Suite underpredicts Henry's law constants of both DNAN and MNA. This is anticipated because HENRYWIN (Henry's law constant module of EPI) relies on a small calibration set of just 345 compounds [224], therefore the predictive capabilities of the EPI Suite in this respect are more limited.

The octanol-water partition coefficients for DNAN and MNA indicate these compounds are neither hydrophobic ($\log K_{ow} > 6$) nor hydrophilic ($\log K_{ow} < 0$) whereas other energetic compounds fall into the hydrophilic category. Molecular level insights into the local environment around DNP and NTO in water-saturated octanol phases also indicate their hydrophilicity or affinity towards water since octanol exhibits both hydrophilic (polar head group) and hydrophobic (hydrocarbon tail) character. Snapshots of a 10 Å solvation shell around DNP in water-saturated octanol is shown in Figure 5.7.

In the water-saturated octanol phase, DNP is located in a polar region comprising of

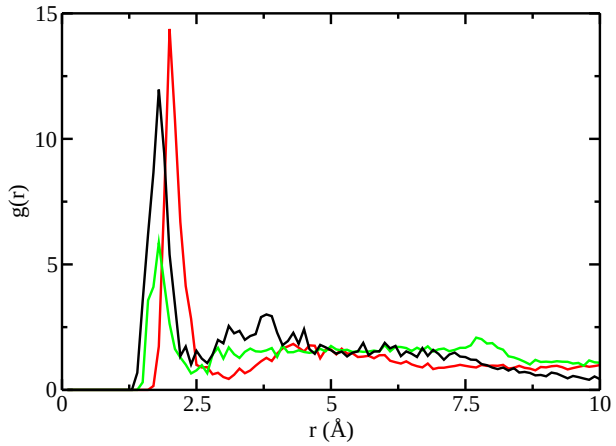

Figure 5.8: Radial distribution function for DNP in water-saturated octanol. DNP oxygen - water hydrogen (black); DNP hydrogen - octanol oxygen (red); DNP oxygen - octanol hydrogen (green).

water molecules and polar head group of octanol which is hydrophilic. Octanol molecules reorient themselves, so that the polar head group is facing the polar region. Extensive intermolecular hydrogen bonding of DNP with water and octanol (hydroxyl oxygen and hydrogen) was found in the water-saturated octanol solution. Amide hydrogens of DNP act as hydrogen donors and oxygens of the nitro group as hydrogen acceptors. Water and octanol act as both hydrogen donors and acceptors. Figure 5.8 shows instances of hydrogen bonding of DNP with water and octanol. Similar behavior was observed for NTO in the water-saturated octanol phase. The presence of hydrogen bonding indicates the strong affinity of DNP and NTO towards aqueous phase.

Compounds with Henry's law constant greater than 10^{-5} atm·m^3/mol ($\log H > -3.4$) are considered highly volatile [225]. Neither of the compounds fall into this category, and favor the aqueous phase. So they do not have any deleterious effect on the air or atmosphere. These findings are further illustrated by plotting the predicted partition coefficients in the multimedia-mobility plot, Figure 5.9 proposed by Gillett [226]. The predicted partition coefficients are located in the heavy concern area D, which is characterized by direct effects

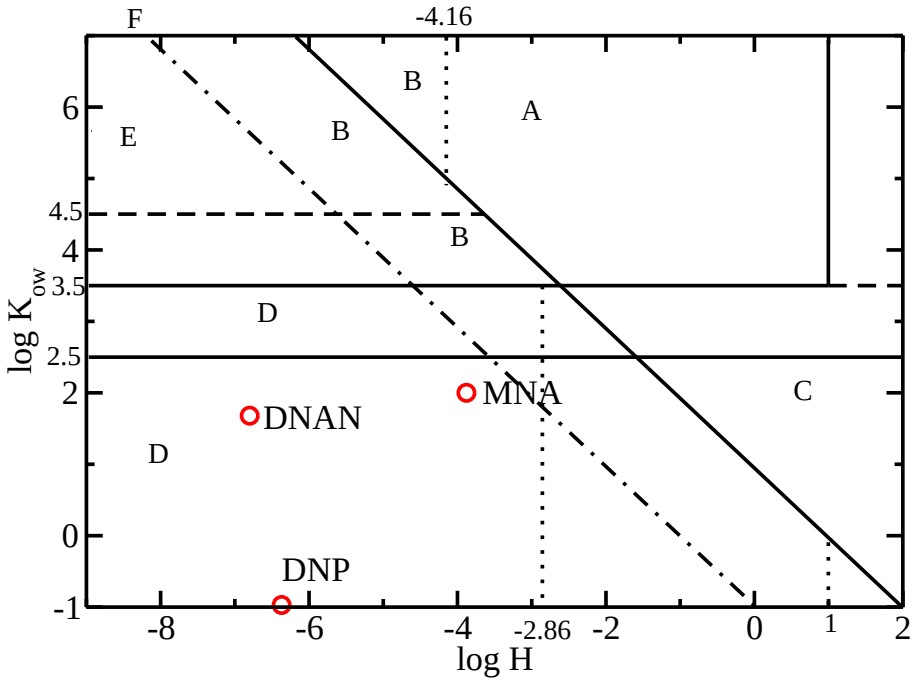

Figure 5.9: Mobility and mutimedia exposure chart [226]. Zone A has heavy multimedia-multispecies concerns and concerns regarding bioaccumulation; zone B has heavy concerns regarding bioaccumulation; zone C is of heavy concern regarding indirect atmospheric problems; zone D is of heavy concern for direct effects in water column; zones E and F are of low ecotoxicologic concern due to very low mobility.

in the water column: leaching to and flow through groundwater and plant root uptake. Although, NTO, MTNI and TATB are not plotted in the figure, they lie beyond the scale of the graph but still in zone D characterized by ground water contamination. The compounds are not predicted to bio-accumulate or induce any atmospheric problems.

5.4.3 Temperature Dependence of Partition Coefficients

The temperature dependence of the octanol-water partition coefficients and Henry's law constants was extracted from additional molecular dynamics simulations performed at 308 and 318 K. The octanol-water partition coefficients and Henry's law constants predicted at different temperatures for DNAN and MNA are listed in Table 5.11, and plotted vs. $1/T$ in Figures 5.10 and 5.11, respectively. The data were fit to the van't Hoff equation

Table 5.11: Temperature dependence of Partition Coefficients for DNAN & MNA.

	DNAN				MNA			
	$\log K_{ow}$		$\log H$		$\log K_{ow}$		$\log H$	
Temp	Sim	Exp [196]	Sim	Exp	Sim	Exp [197]	Sim	Exp
298	1.68	1.61	-6.80	-3.25	2.00	2.10	-3.88	-3.60
308	1.63	1.54	-6.56	-3.24	1.95	1.98	-3.83	-3.64
318	1.54	1.47	-6.47	-3.23	1.92	1.93	-3.80	-3.68

Table 5.12: Enthalpy and Entropy for water-octanol partitioning.

	DNAN		MNA	
Property	Sim	Exp [196]	Sim	Exp [197]
ΔG^{298}(kJ/mol)	-9.58	-9.22	-11.41	-11.95
ΔH(kJ/mol)	-12.65	-12.70	-7.27	-15.06
ΔS(J/mol/K)	-10.27	-11.68	13.83	-10.44

(isochore), which governs the variation of the equilibrium constant with temperature. As an equilibrium constant, $\log K_{ow}$ and $\log H$ can be expressed as,

$$\log X = \frac{-\Delta H}{2.303RT} + \frac{\Delta S}{2.303R} \tag{5.14}$$

where $X = K_{ow}$ or H; ΔH and ΔS are enthalpy and entropy of partitioning from the water to the octanol phase, and are constants over the temperature range studied. ΔH and ΔS are determined from the linear regression fit to the $\log K_{ow}$ vs 1/T plot. The Gibbs free energy of partitioning (ΔG) at a specific temperature is determined from Eq. 5.1. The enthalpies and entropies for partitioning of DNAN and MNA between octanol and water phases are listed in Table 5.12 along with the experimental values. The predicted octanol-water partition coefficients decrease with increasing temperature and are in good agreement with experiment. For both DNAN and MNA, transfer from water to octanol is exothermic which is evident from the negative values of ΔH. Henry's law constants, plotted as $\log H$

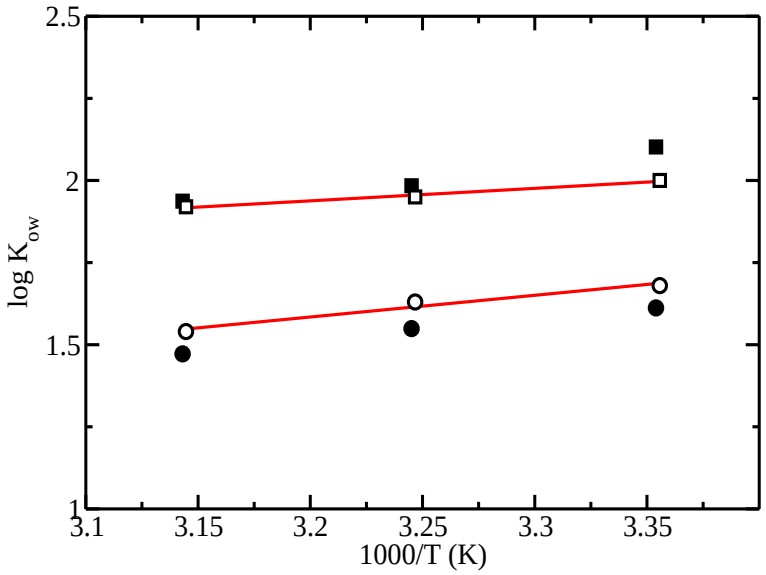

Figure 5.10: Octanol-water partition coefficient as a function of reciprocal temperature for DNAN (circle) and MNA (square). Solid line corresponds to the linear regression fit to simulation data. Filled symbols correspond to experimental values [196, 197].

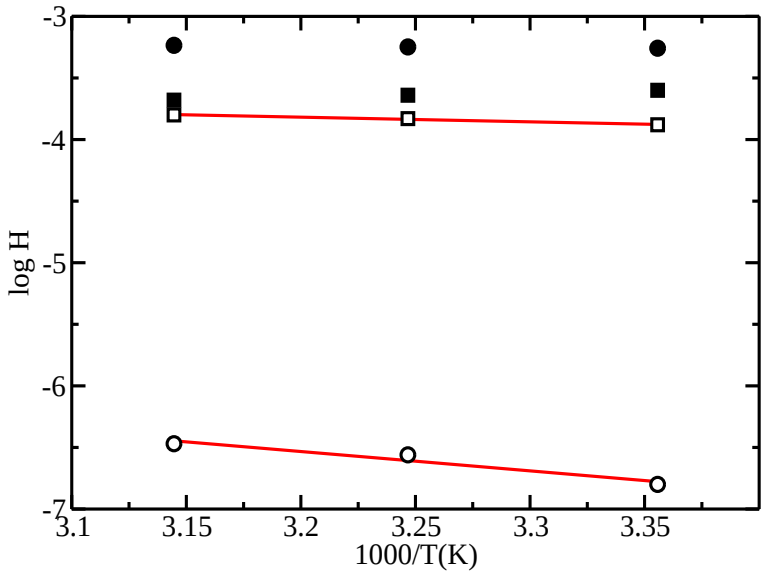

Figure 5.11: Henry's law constant as a function of reciprocal temperature for DNAN (circle) and MNA (square). Solid line corresponds to the linear regression fit to simulation data. Filled symbols correspond to experimental values [196, 197].

vs $1/T$ are shown in Figure 5.11. A linear regression was used to determine ΔH_v and ΔS_v, which are listed in Table 5.13 along with the experimental values [196, 197].

The predicted Henry's law constant increases with increasing temperature. A reverse

Table 5.13: Enthalpy and Entropy for water-air partitioning.

	DNAN		MNA	
Property	Sim	Exp [196]	Sim	Exp [197]
ΔH_v(kJ/mol)	30.06	2.15	3.15	-6.62
ΔS_v(J/mol/K)	-28.86	-55.18	-21.63	-91.30

trend was observed for MNA experimentally, where the Henry's law constant decreased with increasing temperature, although the decrease is small and the statistical error in the data is unknown. In general, experiments [227] have shown the same trend as the simulation data. Therefore it would be advisable to perform additional experiments to identify the source of the unique behavior for the MNA Henry's constant with respect to temperature. The positive enthalpy change indicates that transfer from water to gaseous state is an endothermic process. Negative entropy of transfer and a positive enthalpy term suggests that volatilization is neither enthalpy nor entropy driven (the process is not spontaneous) and the compounds have strong interactions in aqueous solution.

5.4.4 Vapor-Liquid Equilibria

The force field developed can also be used to compute other properties like critical parameters, boiling points, vapor pressure, heats of vaporization and acentric factor. The vapor-liquid coexistence curves and critical parameters are useful for the development and application of equation of state models for these and related compounds. Phase coexistence properties were determined by Gibbs-Duhem integration by running two simultaneous gas and liquid simulations. A plot of average total energy and volume with respect to timestep from a coexistence simulation of DNAN are shown in Figure 5.12 and 5.13 respectively. Vapor-liquid coexistence curves are presented in Figure 5.14 and 5.16 and vapor pressure plots in Figure 5.15 and 5.17. Phase coexistence properties were not determined for TATB

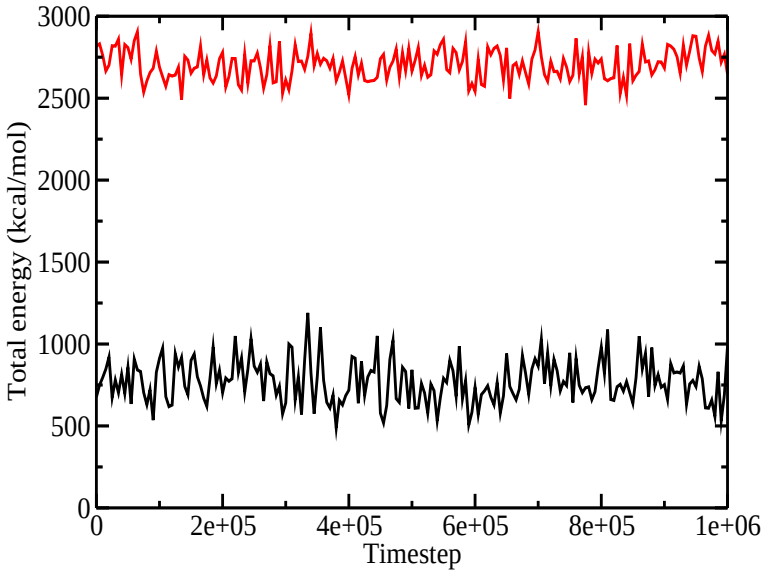

Figure 5.12: Average energy vs. timestep for the liquid (black) and gas (red) simulation at 726.49 K and 5.99 bar.

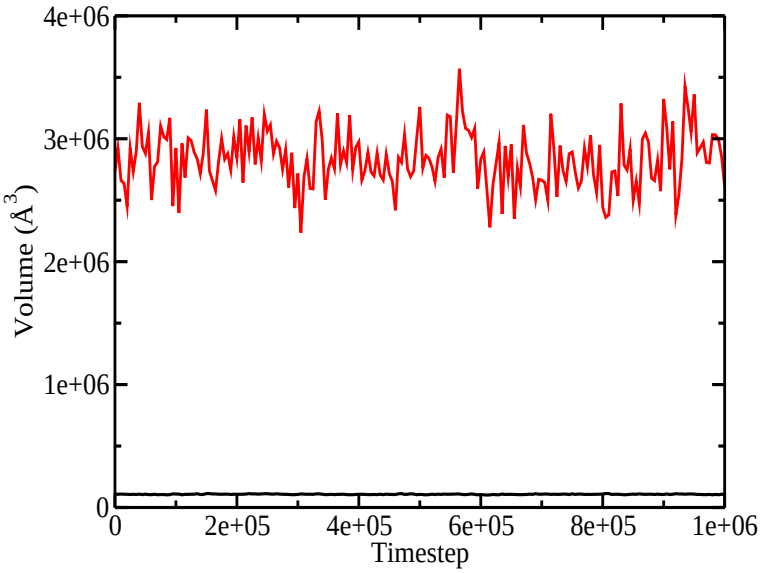

Figure 5.13: Average volume vs. timestep for the liquid (black) and gas (red) simulation at 726.49 K and 5.99 bar.

as it was difficult to simulate a stable gas or liquid phase near the critical temperature for the initial coexistence point. The phase diagrams should be considered hypothetical, since these compounds are known to decompose at temperatures near their normal boiling points.

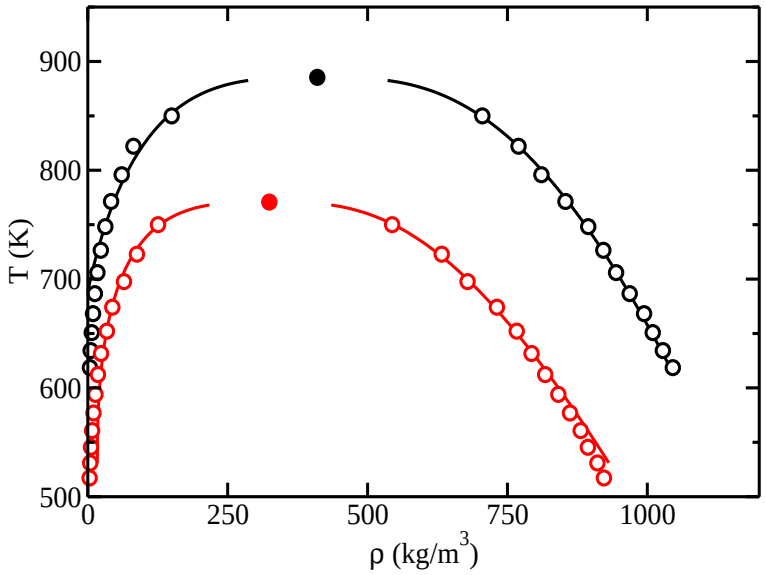

Figure 5.14: Vapor-liquid coexistence curves for DNAN (black) and MNA (red) predicted by molecular dynamics simulations. Line is a fit of simulation data to scaling laws. Filled symbols correspond to critical points derived from coexistence data.

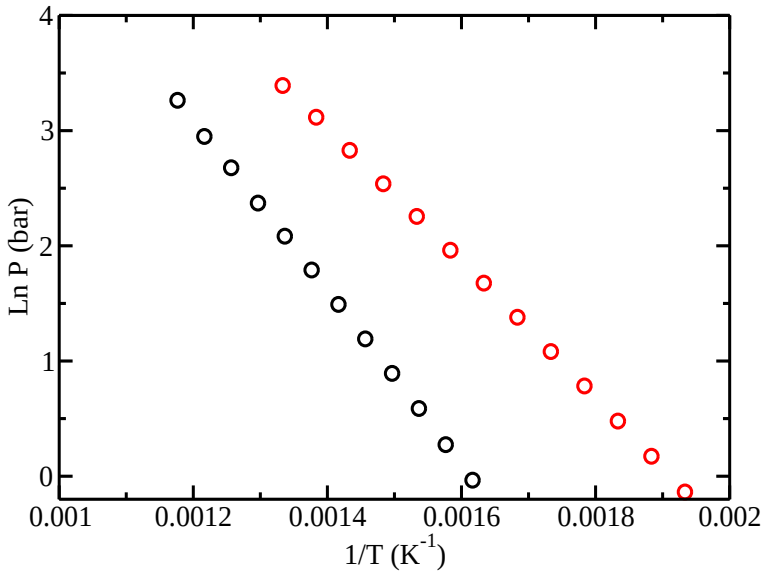

Figure 5.15: Clausius-Clapeyron plot for DNAN (black) and MNA (red).

Critical temperatures and densities were computed by fitting the saturated liquid and vapor densities to the density scaling law for critical temperature [228]

$$\rho_{liq} - \rho_{vap} = B(T - T_c)^{\beta} \tag{5.15}$$

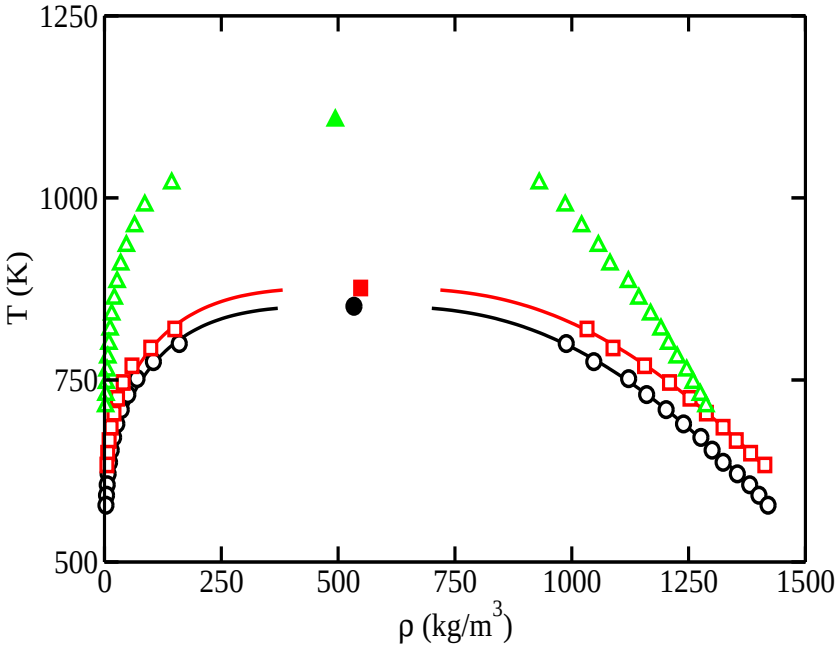

Figure 5.16: Vapor-liquid coexistence curves for DNP (black), MTNI (red) and NTO (green) predicted by molecular dynamics simulations. Line is a fit of simulation data to scaling laws. Filled symbols correspond to critical points derived from coexistence data.

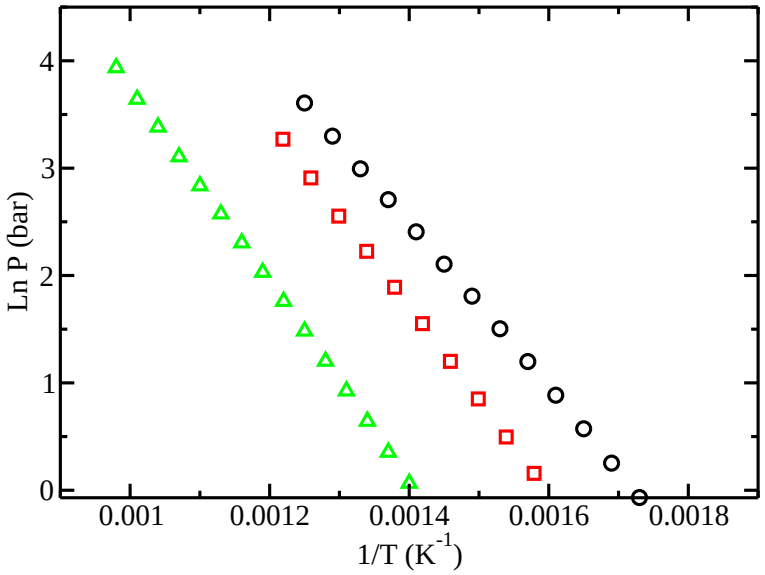

Figure 5.17: Clausius-Clapeyron plot for DNP (circle), MTNI (square) and NTO (triangle)

and the law of rectilinear diameters [229]

$$\frac{\rho_{liq} + \rho_{vap}}{2} = \rho_c + A(T - T_c) \tag{5.16}$$

where $\beta = 0.325$ is the critical exponent for Ising-type fluids in three dimensions [230] and A and B are constants fit to simulation data. The critical parameters, boiling point and acentric factor are listed in Table 5.14 along with values predicted through group contribution [222, 231].

Table 5.14: Critical Parameters and boiling point

Molecule	T_c [K]	ρ_c [kg/m^3]	P_c [bar]	T_{nb} [K]	ω
DNAN[a]	885.42	410.20	37.36	620.82	1.54
DNAN[b]	806	-	39.9	588	0.85
MNA[a]	770.75	324.50	37.70	522.76	1.41
MNA[b]	748	-	41.7	527	0.65
DNP[a]	851.21	533.80	66.06	580.27	0.67
DNP[b]	817	-	69.3	575	3.07
MTNI[a]	876.24	548.30	50.87	626.52	0.83
MTNI[b]	845	-	54.7	629	1.21
NTO[a]	1106.39	494	103.03	709.78	0.54
NTO[b]	829	-	86	568	0.79

[a] This work. [b] Group Contribution [231]

The difference between the values predicted by simulation and group contribution is more pronounced for DNAN and NTO than any other energetic material. The source of the difference is unknown although for DNAN, it may be due to the proximity of the ortho-nitro group and the methoxy group. These effects are taken into account by the proposed models via the quantum mechanically derived partial charge distributions. Group contribution methods, while accounting for bonding environment, do not include effects due to the proximity of other functional groups, limiting their predictive capability. The experimental boiling point of DNAN at 12 mm Hg is 479 K [215]. The vapor pressure data from simulation were extrapolated using the Clausius-Clayperon equation to 12 mm Hg (0.016 bar) and predicted a boiling point of 461.04 K which is about 3.7% lower than the experiment. Heats of vaporization were calculated as a function of temperature for each

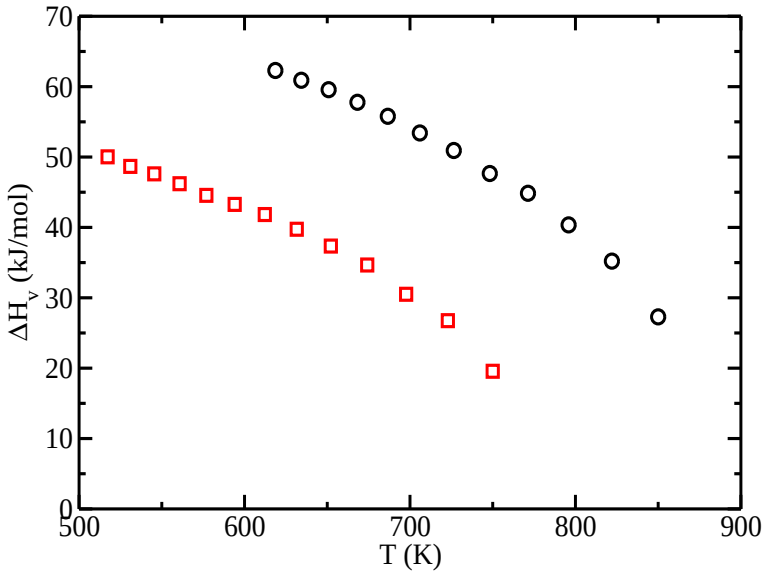

Figure 5.18: Heat of vaporization for DNAN (black) and MNA (red) predicted from NPT MD simulations

molecule using the data from NPT molecular dynamics simulations, and Equation 5.17

$$\Delta H_v = U_v - U_l + p(V_v - V_l) \tag{5.17}$$

where subscripts v and l refer to the vapor and liquid phases, respectively. U is the internal energy per mol and V is the molar volume. The results of these calculations are shown in Figure 5.18 and Figure 5.19. No experimental heat of vaporization data exists for any energetic compound of interest to make a comparison.

5.5 Conclusion

Force fields were developed for six energetic materials, DNAN, MNA, DNP, NTO, MTNI and TATB and the predicted thermo physical properties were found to be in close agreement (5-10% in most cases) with the scarce experimental data available. Based on the predicted octanol-water and Henry's law constants, all compounds studied in this work are predicted to be problematic with respect to groundwater contamination. In addition to the properties

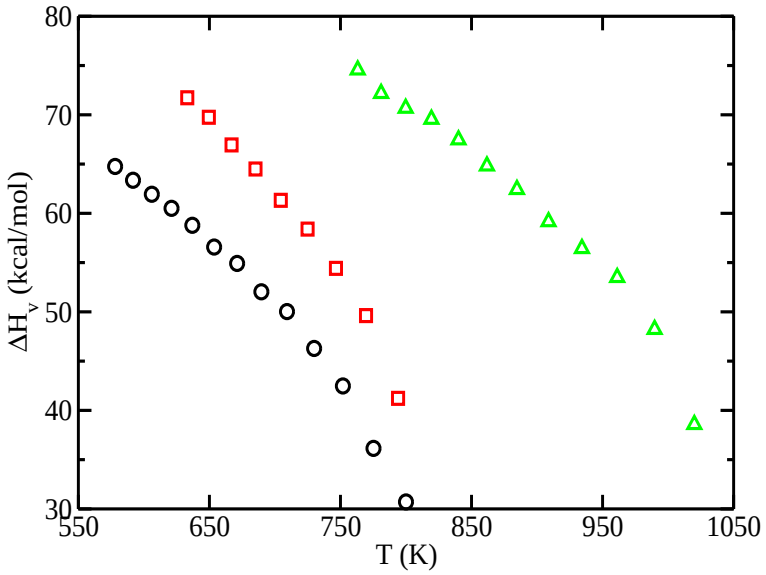

Figure 5.19: Heat of vaporization for DNP (black), MTNI (red) and NTO (green) predicted from NPT MD simulations

calculated in this report, the generalized transferable force fields for energetic materials presented here may be used to investigate the interactions of energetic materials in a wide variety of complex systems, including their diffusion and transport in the environment.

Chapter 6

Energetic Materials: Solid Phase Properties

6.1 Introduction

Solid phase properties of energetic materials are crucial because most of them exist as solids at room temperature. More solid phase properties have been measured for energetic materials than condensed phase properties. So there has been good progress in force field development to study crystal structure and melting point. Numerous force fields have been developed for predicting the solid properties of many energetic materials.

An intermolecular potential based on a combination of Buckingham exponential-6 potential and point charges was developed for the study of crystalline RDX [232]. This potential was transferable and was used to describe intermolecular interactions of similar energetic compounds like HMX and HNIW. An improvement to this force field was made by adding intramolecular interactions from the well-known AMBER force field [233] and making the molecule flexible. This was referred to as the SRT-AMBER force field [234]. NPT Monte Carlo (MC) and molecular dynamics (MD) were used to determine various solid properties using the parametrized force fields. Gee *et al.* [235] developed a model for 1,3,5-triamino-2,4,6-trinitrobenzene (TATB) by parametrizing it to solid properties of TATB. In the next section, force fields used to predict various solid phase properties are presented followed by simulation methodologies. In the results section, the predicted solid state properties such as crystal density, lattice parameters for the energetic materials are presented.

6.2 Force field

An explicit hydrogen (EH) force field was developed for DNAN and MNA for solid phase calculations. The EH force field for DNAN and MNA was motivated by the poor performance of the UA force field in the prediction of crystal lattice parameters and solid densities. In the explicit hydrogen force field, all hydrogens are modeled explicitly, with their interaction sites centered on respective atomic nuclei. In the explicit hydrogen version, the Lennard-Jones parameters for the nitro group and the amine group were transferred from the explicit model of nitrobenzene and aniline respectively reported by Siepmann *et al.* [203]. The parameters for the ring carbon and the hydrogen attached to it were also derived from Siepmann's force field for nitrobenzene or aniline. The parameters for the methyl group were obtained from force field for 1,1,1,2-tetrafluoroethane [236]. The parameters for the alkoxy oxygen and carbon atoms for DNAN were transferred from the united-atom force field for DNAN. For NTO, MTNI and TATB, the same force fields used for predicting condensed phase properties were used.

6.3 Methodologies

6.3.1 Crystal Density and Lattice Parameters

Force fields were validated by generating lattice parameters and crystal densities and comparing them to the experiment. These calculations require knowledge of the experimental crystal structures. The crystal structures determined from the experiment and their characteristics are listed in Table 6.1. There has been no crystal structure reported for DNP in the literature, so it is omitted from the following discussion. For the crystal density and lattice parameter calculations, initial crystal structures were taken from the

Table 6.1: Crystal structures

Compound	Structure	Lattice vectors	Interaxial Angles
DNAN & MNA[1,2]	Monoclinic	$a \neq b \neq c$	$\alpha, \gamma = 90°$; $\beta \neq 90°$
NTO & TATB[3,4]	Triclinic	$a \neq b \neq c$	$\alpha, \beta, \gamma \neq 90°$
MTNI[5]	Orthorhombic	$a \neq b \neq c$	$\alpha, \beta, \gamma = 90°$

[1,2] [160, 162] [3,4] [173, 238] [5] [239]

Cambridge Crystallographic Database [237] and replicated in i, j and k directions to create a supercell. The key for reproducing the lattice parameters and crystal density is the periodic boundary conditions. Incorrect representation of the periodic boundary may result in an unstable crystal structure. The vector matrix for any crystal lattice is given by,

$$V = \begin{pmatrix} ax & ay & az \\ bx & by & bz \\ cx & cy & cz \end{pmatrix}$$

where a, b, c are the unit cell dimensions and x, y, z are the corresponding vectors. The elements of the above matrix varies for each unique crystal structure. If a supercell is created by replicating the unitcell by i in x axis, j in y axis and k in z axis, then the vector matrix for the supercell for each crystal structure is given by,

Orthorhombic:

$$V = \begin{pmatrix} ia & 0 & 0 \\ 0 & jb & 0 \\ 0 & 0 & kc \end{pmatrix}$$

Monoclinic:

$$V = \begin{pmatrix} ia & 0 & 0 \\ 0 & jb & 0 \\ kc.\cos(\beta) & 0 & kc.\sin(\beta) \end{pmatrix}$$

Triclinic:

$$V = \begin{pmatrix} ia & 0 & 0 \\ jb.\cos(\gamma) & jb.\sin(\gamma) & 0 \\ kc.\cos(\beta) & kc.(\cos(\alpha) - (\cos(\beta).\cos(\gamma)))/\sin(\gamma) & kc.(((\sin(\beta))^2 - ((\cos(\alpha) - \\ & & (\cos(\beta).\cos(\gamma)))/\sin(\gamma)))^2) \end{pmatrix}$$

where, α, β and γ are the interaxial angle, i.e., α is the angle between y and z vectors; β is the angle between x and z vectors; γ is the angle between x and y vectors. Using these definitions, the vector matrix is generated for each crystal structure for the simulation. NPT molecular dynamics simulations were run at zero pressure and 298 K. The system was initially heated from 5 K to the target temperature of 298 K using a simulated annealing technique. The temperature and pressure control methodology is the same as MD simulations discussed in prior sections. The system was equilibrated for 1 ns, where first 250 ps was used for equilibration, followed by 750 ps of time averaging for the cell volume. Electrostatic interactions were computed using the Particle Mesh Ewald method. The average volume was then used to calculate the crystal density.

6.3.2 Melting Point

The most direct theoretical way of computing the thermodynamic melting point is by a single NPT MD simulation of the solid. However, the free energy barrier associated with

the formation of solid-liquid interface induces superheating effects and hysteresis in the solid-liquid transition. This makes the theoretical prediction of melting point tedious. The commonly used melting point methods [240] are the thermodynamic integration method, void-nucleated melting method and the solid-liquid interface method. Another method which was proposed recently by Luo *et al.* [241] is the hysteresis method which computes the melting point with the knowledge of the superheating and the supercooling temperature using equation

$$T_{mp} = T_+ + T_- - \sqrt{(T_+ T_-)} \tag{6.1}$$

where T_+ and T_- are the superheating and supercooling temperatures respectively. The superheating temperature is the temperature at which the solid structure melts. This temperature is always elevated than the true melting point due to the superheating caused by the free energy barrier. The supercooling temperature is equivalent to the glass transition temperature since it is nearly impossible to establish crystallization of liquid to solid in a simulation. The temperature where, the liquid transforms to an amorphous solid is the glass transition temperature. The thermodynamic integration method [242–244] is based on the equality of Gibbs free energy of the solid and liquid at the melting point

$$g_s(P, T_m) = g_l(P, T_m) \tag{6.2}$$

where $g(P, T)$ is the Gibbs free energy with subscripts s and l referring to the solid and liquid phases respectively, P is the pressure and T_m refers to the melting point. Although this can be carried out using Gibbs-Duhem integration, a starting solid-liquid coexistence point is required to start the integration from.

In the second method [245–247], voids are introduced in the supercell to eliminate the free energy barrier. The voids aid in creating nucleation sites that results in formation of solid-liquid interfaces which remove the free energy barrier. Generally, the melting temperature calculated from a single NPT MD simulation of the crystal without voids is always higher than the true thermodynamic melting point due to the superheating effects. But the presence of voids reduces the melting point of the compound until a plateau region is reached where the melting point is independent of the voids. The temperature corresponding to this plateau region is the thermodynamic melting point. The drawbacks of this method are that

1. It requires lot of computation time to determine the accurate melting point

2. The plateau region is sometimes narrow and unclear

3. The calculations are sensitive to the number of voids introduced. In case of less number of voids, not enough solid-liquid interfaces are generated to eliminate superheating and on the contrary, too many voids results in the collapse of the solid structure. The solid-liquid interface method is a promising alternative to the thermodynamic integration and the void nucleation method. Although the method requires large simulation cells and longer sampling times, recent advancements in computational resources allows calculation of accurate melting points even for complex materials like the explosives.

The last method, the solid-liquid interface method [248, 249] is in principle similar to the void nucleation method since both aid in reducing the free energy barrier. In the solid-liquid interface method, this is accomplished by having an explicit interface between the solid and

liquid configuration. Both the phases evolve in the NVE ensemble (constant number of particles, volume and energy) towards the thermodynamic melting point. In this research, solid-liquid interface method was used to determine the melting point.

6.4 Results & Discussion

6.4.1 Explicit vs United Atom

Initially, solid phase calculations were run for united atom models of DNAN and MNA which were used for the prediction of other thermophysical properties. But there were significant deviation between the predicted lattice parameters and the experimental values. So all the hydrogens in the CH and CH_3 groups are treated explicitly. But having explicit hydrogens was not sufficient to improve the predictions from the simulations. So, the Lennard-Jones parameters of the nitro and the amine group were transferred from explicit models of nitrobenzene and aniline [203]. The model with these parameters improved the predictions of the united atom force field significantly. Similar behavior was observed for NTO and MTNI. Although the structures of NTO and MTNI do not have any hydrogens attached to the ring carbon, the original TraPPE-UA parameters for the nitro and the amino groups were replaced by the parameters from the explicit nitrobenzene and aniline.

Table 6.2: Crystal parameters and density for MNA

Parameters	United atom	Explicit (ring)	Explicit (nitro & amine)	Exp
a (Å)	9.28	10.18	9.78	10.07
b (Å)	6.35	7.17	7.02	6.93
c (Å)	14.05	11.51	11.07	10.81
α	90	90	90	90
β	98.46	101.34	101.32	101.95
γ	90	90	90	90
ρ [g/cm^3]	1.22	1.22	1.36	1.36

Table 6.3: Crystal parameters and density for NTO

Parameters	United atom	Explicit (nitro & amine)	Experiment
a (Å)	5.20	5.21	5.12
b (Å)	10.17	10.50	10.30
c (Å)	20.21	18.32	17.90
α	104.55	106.58	106.70
β	97.06	97.79	97.70
γ	90.04	90.11	90.20
ρ [g/cm^3]	1.67	1.81	1.92

Table 6.4: Crystal parameters and density for MTNI

Parameters	United atom	Explicit (nitro & amine)	Experiment
a (Å)	8.76	8.51	8.61
b (Å)	18.58	17.70	17.71
c (Å)	11.07	9.89	10.68
α	90	90	90
β	90	90	90
γ	90	90	90
ρ [g/cm^3]	1.59	1.92	1.76

A comparison between the explicit and united atom model parameters for MNA, NTO and MTNI are presented in Tables 6.2, 6.3 and 6.4 respectively along with the experimental values. As seen from the tables, the explicit models with explicit hydrogens and new nitro and amino parameters show significant improvement in the predictions of the unit cell dimensions, interaxial angle and crystal density of the solid. The effect of including hydrogens in the force field is significant and alters the solid phase properties unlike the condensed phase properties. Also the Lennard Jones parameters have to be consistent i.e., the LJ parameters of the entire molecule should be derived from either an explicit or the united atom force field. Mixing of explicit and united atom parameters in a molecules will yield unreliable or inaccurate predictions.

6.4.2 Lattice Parameters & Crystal Density

The lattice parameters and density estimated from molecular simulation for explicit model of DNAN and MNA are presented in Tables 6.5. The solid paramaters predicted for NTO, MTNI and TATB are listed in Table 6.6. The lattice parameters and crystal density predicted by simulation for DNAN, MNA, NTO and TATB are in good agreement with the experiment. For MTNI, simulation under predicts the c dimension and slightly over predicts the crystal density. Snapshots of the initial crystal structure and the final structure after the NPT simulation for all the energetic materials are shown in the Figure 6.1, 6.2, 6.3, 6.4 and 6.5. As seen from the figures, all energetic materials remain stable without any unlikely displacement after the NPT MD simulationa at 298 K and zero pressure.

Table 6.5: Crystal parameters and density for DNAN & MNA

	DNAN		MNA	
Method	Sim	Exp	Sim	Exp
a (Å)	9.15	8.77	9.78	10.07
b (Å)	12.23	12.64	7.02	6.93
c (Å)	15.63	15.42	11.07	10.81
α	90	90	90	90
β	81.64	81.89	101.32	101.95
γ	90	90	90	90
ρ [g/cm^3]	1.52	1.56	1.36	1.36

Table 6.6: Crystal parameters and density for NTO, MTNI & TATB

	NTO		MTNI		TATB	
Method	Sim	Exp	Sim	Exp	Sim	Exp
a (Å)	5.21	5.12	8.51	8.61	8.89	9.01
b (Å)	10.50	10.30	17.70	17.71	8.91	9.02
c (Å)	18.32	17.90	9.89	10.68	6.64	6.81
α	106.58	106.70	90	90	108.77	108.59
β	97.79	97.70	90	90	91.82	91.82
γ	90.11	90.20	90	90	119.95	119.97
ρ [g/cm^3]	1.81	1.92	1.92	1.76	2.03	1.93

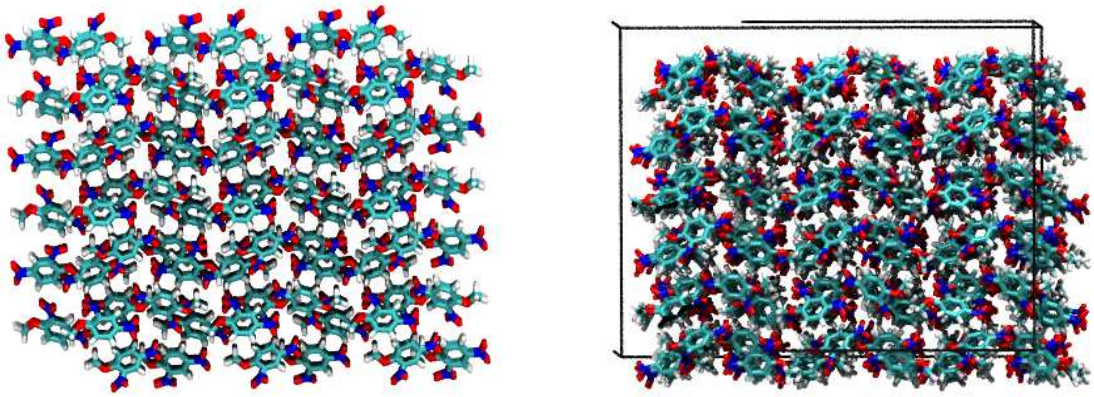

Figure 6.1: Crystal structure of DNAN before(left) and after(right) NPT MD simulation at 0 bar and 298 K.

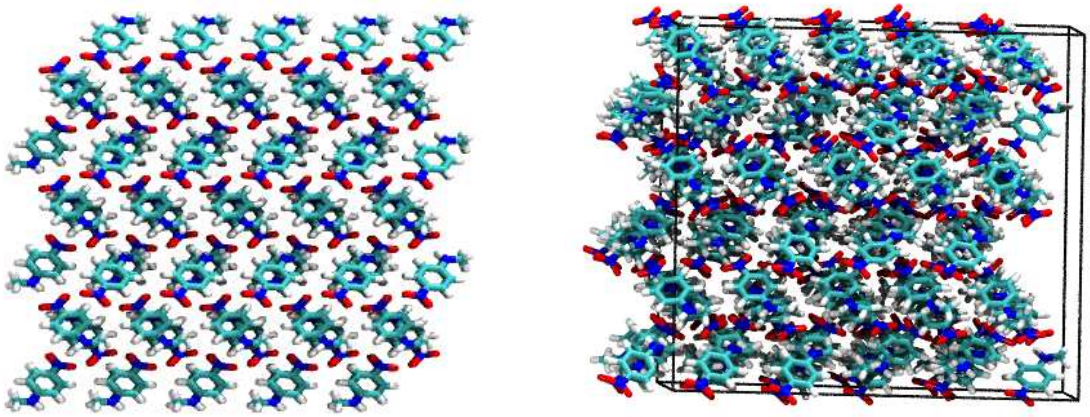

Figure 6.2: Crystal structure of MNA (3x5x3 matrix) before(left) and after(right) NPT MD simulation at 0 bar and 298 K.

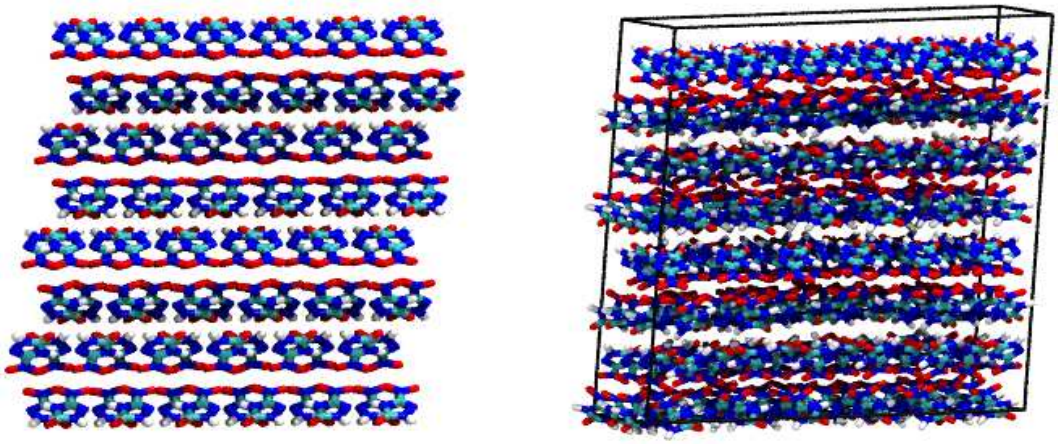

Figure 6.3: Crystal structure of NTO (6x3x2 matrix) before(left) and after(right) NPT MD simulation at 0 bar and 298 K.

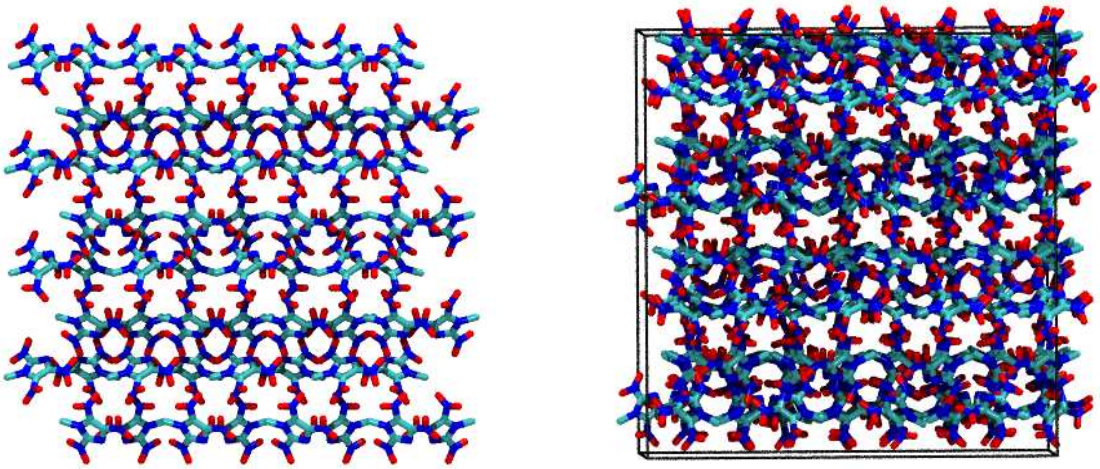

Figure 6.4: Crystal structure of MTNI (4x2x3 matrix) before(left) and after(right) NPT MD simulation at 0 bar and 298 K.

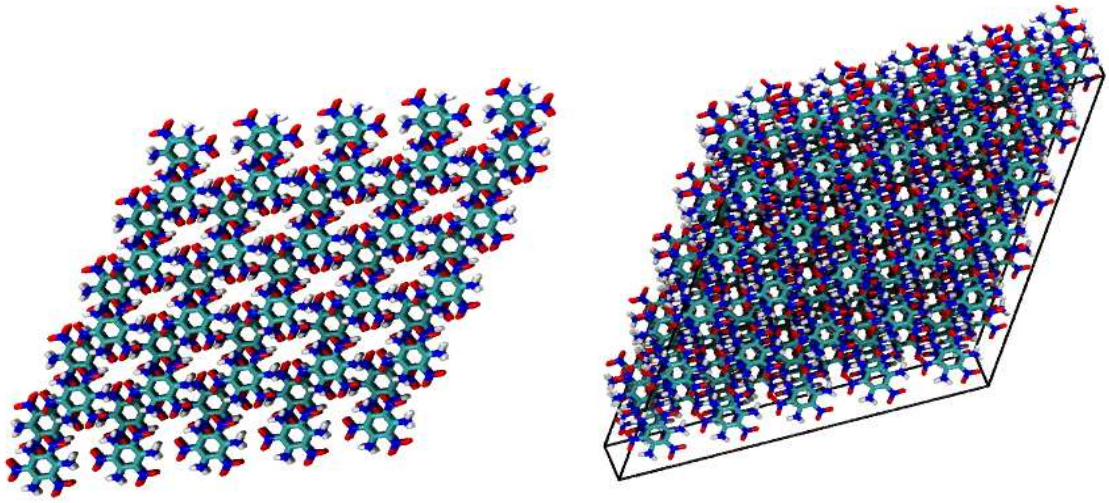

Figure 6.5: Crystal structure of TATB before(left) and after(right) NPT MD simulation at 0 bar and 298 K.

6.4.3 Melting Point

A solid-liquid interface method based on the work of Watt *et al.* [250] and Morris *et al.* [251] was used to determine the melting point of NTO. A solid-liquid interfacial system was prepared as follows: in the original supercell, 33% of the molecules were constrained to fixed coordinates and the rest of the molecules were allowed to move. A few molecules were permanently removed from the movable region to create solid-liquid interface. The structure is then subjected to MD simulations in the NVT ensemble around 1000 K for 200 ps to create liquid regions adjacent to the fixed zone. The final configuration of this run is then used for NPT simulation at temperatures close to the experimental melting point.

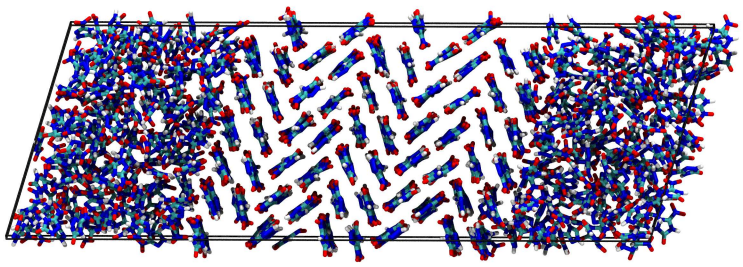

Figure 6.6: Snapshot of solid-liquid interface used for NVE simulations

Subsequent to this, molecular dynamics simulations in the NVE ensemble are used for equilibration and sampling of temperature and pressure. This final step is repeated several times by changing the volume of the cell. The resulting temperatures and pressures are plotted and a linear regression fit is made. The temperature corresponding to the atmospheric pressure is the melting point. A snapshot of the initial configuration used to simulate the melting transition in the NVE ensemble is shown in Figure 6.6.

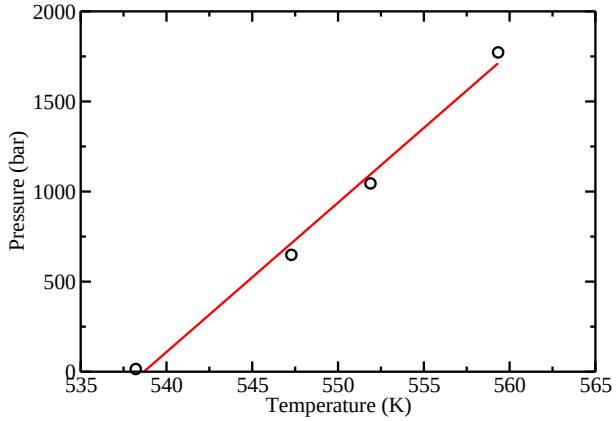

Figure 6.7: Temperature vs Pressure plot for solid-liquid interface

The temperature-pressure plot from the melting point simulations are presented in Fig-

ure 6.7. Although pressure and temperature do not have a linear relation, the small range of temperatures (530-560 K) covered allows assumption of linear dependence. The temperature corresponding to the atmospheric pressure is the melting point of NTO. The melting point predicted is 538.69 K which is in excellent agreement with the experimental value of 539.35 K [252]. A variant to the above two phase method has also been investigated for estimation of melting point. This method is based on the work of Vega *et al.* [253] and also simulates a solid-liquid interfacial configuration.

A coexisting solid-liquid configuration was generated as discussed in the previous method. This two phase structure is then subjected to a series of NPT simulations around the experimental melting point of a compound at 1 atm pressure. The energy of the system is monitored with respect to time. If the temperature is above the melting point, the solid region will melt leading to increase in energy over time while the liquid region will freeze if it is below the melting point. If the energy value is fluctuating around a constant value, the temperature is almost at the melting point. Although an accurate melting point could not be determined through this method, an upper and lower limit for the solid-liquid transition was observed. For NTO, the calculations suggested the melting point lies between 530 K and 550 K which is in good agreement with the experimental melting point of 539.35 K.

The method of Vega *et al.* was continued for MTNI and MNA for predicting the melting point range. A solid-liquid interfacial configuration was generated by constraining 50% of the molecules in the original supercell to fixed positions, allowing rest of the system to move freely by removing few molecules and running a NVT simulation at high temperature such as 1000K. Series of NPT simulations were run at different temperatures around the experimental melting point of each compound at 1 atm pressure. For MNA, the original

supercell was a 3x5x6 matrix and the simulations were carried out at 435, 425, 415 and 410 K since the melting point of MNA measured from experiment is 425.15 K [239]. At each of these temperatures, the solid structure melted indicating all the temperatures were above the melting point. This suggests a clear underprediction of the melting temperature. For MTNI, the original supercell was a 4x2x6 matrix and the melting point available from experiment is 355.15 K [254]. NPT simulations were run at 300, 350, 360 and 380 K. It was observed that none of the simulations resulted in melting of the solid portion indicating an overprediction of the melting temperature range. For DNAN and TATB, a stable coexisting solid-liquid structure could not be constructed and hence no melting points were predicted for them.

6.5 Conclusion

The force fields developed to predict condensed phase properties were able to reproduce the crystal density and lattice parameters for all the energetic materials except for DNAN and MNA. Separate explicit atom force fields were developed for DNAN and MNA which predicted lattice parameters and crystal density in good agreement with the experiment. This demonstrates the sensitivity of the solid state properties to the molecular representation of atom moieties. Most of the molecules in the solid state are held together by hydrogen bonding. So inaccurate crystal densities and lattice parameters may result from missing hydrogen atoms in the force field.

Chapter 7

Chemical Warfare Agents

7.1 Introdution

The two chemical warfare agents studied in this work are *O*-isopropyl methylphosphonofluoridate (sarin) and *O*-Pinacolyl methylphosphonofluoridate (soman). Due to the toxicity of chemical warfare agents, majority of experimental studies are performed with relatively non-toxic simulants. An ideal simulant would mimic relevant chemical and physical properties of the agent except for its toxicity. Since, no simulant can satisfactorily represent all thermophysical properties of a nerve agent, developing molecular models would help in studying these nerve agents without being exposed to them during experiments. Before constructing force fields for the nerve agents sarin and soman, a force field was developed for dimethylmethylphosphonate (DMMP), the most common simulant of sarin. Non-bonded parameters can then be derived for sarin and soman from functionally similar atom moieties of DMMP without any additional parametrization. A schematic of DMMP, sarin and soman are shown in Figure 7.1.

Numerous experimental and a very few theoretical studies have been reported for measuring or predicting physical properties of DMMP, sarin and soman. Cuisset *et al.* [255] measured the vapor pressure for DMMP using gas-phase chromatography and Tevault *et al.* [256] measured the volatility of DMMP in the presence of water to determine the effect of humidity on DMMP's vapor pressure. Recently Butrow *et al.* [257] published vapor pressures measured for several organophosphorus nerve agent simulant compounds. Vapor pressures have also been reported for sarin and soman [258, 259]. Some theoretical studies

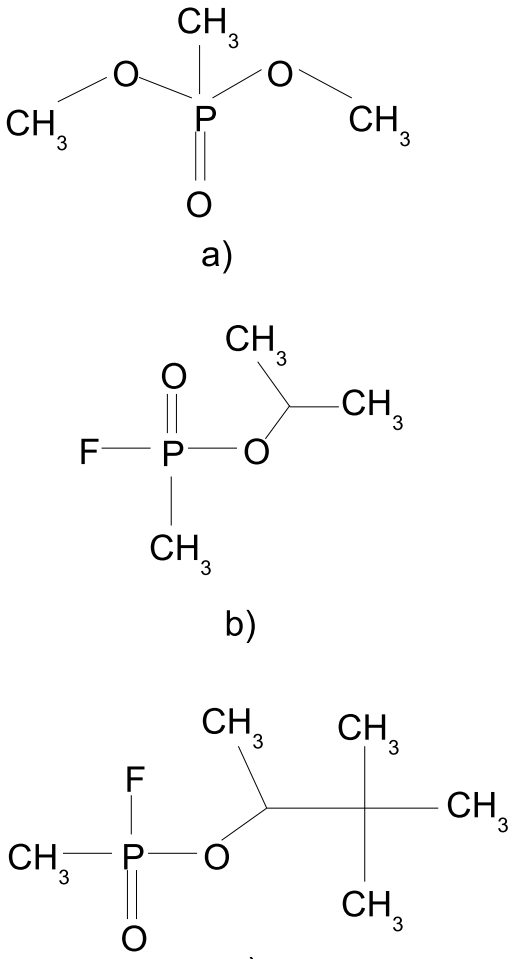

Figure 7.1: Molecular Structures of a)DMMP; b)Sarin & c)Soman

on DMMP [260], sarin [261] and soman [262] discuss various conformers and the rotational barriers associated with these compounds. Although various condensed phase properties of CWAs have been measured experimentally, molecular models would aid in developing detection or removal techniques which is difficult through experiments. In this context, the molecular models would be used in simulating the adsorption in carbon pores. The available properties from experiments are used to validate the force field. In the following section, force fields used for the molecules of interest and the carbon pore are presented

7.2 Force Field

7.2.1 Fluid-fluid interactions

Two forcefields, the Vishnyakov and Neimark force field (VN) [263] and the new force field developed by our group were utilized in this work. Non-bonded interactions for both forcefields are given by pairwise additive Lennard-Jones 12-6 (LJ) potentials with Coulombic interactions for partial charges. The partial charges in the new force field were determined through CHELPG analysis of the electrostatic potential energy surface calculated at HF/6-31+G(d,p) level of theory and basis sets in Gaussian 03 [109].

The Lennard-Jones parameters for all the functional groups except for P in DMMP were taken directly from TraPPE-UA force field. Parameters for CH_3 comes from TraPPE-UA force field for alkanes [86], oxygen in O-CH_3 from oxygen in ethers [111] and oxygen in O=P from carboxylic acid [96]. The parameters for phosphorous were tuned to reproduce the vapor pressure of DMMP over the temperature range 325-408 K [264, 265] and the liquid densities at 303 and 373 K [266, 267]. For sarin and soman, LJ parameters for functionally similar pseudo atoms were taken from the DMMP model. Fluorine parameters were taken from the OPLS-AA forcefield [268]. The additional alkyl groups in soman were assigned LJ parameters from TraPPE-UA force field for branched alkanes [88]. Water was simulated using SPC/E force field [269]. The LJ parameters and the partial charges for all functional groups for both force fields are listed in Table 7.1.

Fixed bond lengths were used in the new force field while the VN force field utilizes a covalent-bond-stretching potential between all interaction sites. A simple harmonic potential describes angle bending in both force fields. All the bond lengths, bond angles and the bending force constants are listed in Table 7.2. The torsional potential for the new force

Table 7.1: Parameters for non-bonded interactions. Parentheses denote functional group attached to the atom of interest

DMMP	ε [K]	σ [Å]	q [e]
CH_3	98.0	3.75	0.28[a]/-0.14[b]
O-(CH_3)	55.0	2.80	-0.53
O=(P)	79.0	3.05	-0.80
P	86.0	4.00	1.44
Sarin			
CH_3	98.0	3.75	-0.08[b]/-0.10[c]
CH-(O)	10.0	4.68	0.62
O-(CH)	55.0	2.80	-0.63
O=(P)	79.0	3.05	-0.77
P	86.0	4.00	1.40
F	26.7	2.95	-0.34
Soman			
CH_3	98.0	3.75	-0.08[b]/-0.10[c]/-0.15[d]
CH	10.0	4.33	0.43
C	0.5	6.40	0.54
O-(CH)	55.0	2.80	-0.63
O=(P)	79.0	3.05	-0.77
P	86.0	4.00	1.40
F	26.7	2.95	-0.34
VN Force field			
CH_3	104.04	3.80	0.131[a]/-0.021[b]
O-(CH_3)	80.23	3.03	-0.36
O=(P)	80.23	2.93	-0.691
P	174.5	3.83	1.17

[a] Site adjacent to oxygen. [b] Site adjacent to phosphorous.
[c] Site adjacent to CH group. [d] Site adjacent to C.

Table 7.2: Vibration and bending parameters for DMMP, Sarin and Soman

Vibration	Bond length [Å]	Bending	Bond angle [deg]	k_θ/k_b [K]
P=O	1.458 1.495	∠O=P-CH_3	116.3	80586
P-CH_3	1.79	∠O=P-O	116.5	100794
P-O	1.58	∠CH_3-P-O	104.3	40894
O-CH_3	1.41	∠CH_3-O-P	121	80586
CH_3-CH	1.54	∠O-P-O	106.5	62500
CH-O	1.41	∠CH_3-CH-O	106.0	62500
CH-C	1.54	∠CH_3-CH-CH_3	114	62500
CH_3-C	1.54	∠CH_3-C-CH_3	109.4	62500
F-P	1.58	∠CH_3-P-F	104.3	40894

Table 7.3: Torsional parameters for DMMP, Sarin and Soman

Dihedral	c_0	c_1	c_2	c_3	f
O=P-O-CH_3	1534.91	-1102.11	291.88	397.57	-0.15
CH_3-CH-O-P	1041.22	-753.00	432.00	227.00	1.88
CH_3-P-O-CH	57.48	1476.00	184.10	0.00	-0.34
O=P-O-CH	2996.00	-1467.00	215.00	-31.60	0.44
CH_3-C-CH-O	0.00	176.60	-53.30	769.90	0.00
CH_3-C-CH-CH_3	0.00	355.00	-68.20	791.30	0.00

field is characterized by the following cosine series

$$U_{tors} = c_0 + c_1[1 + cos(\phi + f)] + c_2[1 - cos(2\phi + f)] + c_3[1 + cos(3\phi + f)] \tag{7.1}$$

where ϕ is the dihedral angle and c_i are the Fourier constants which are listed in Table 7.3. These coefficients were determined by fitting Equation 7.1 to the potential energy surfaces generated from HF/6-31G+(d,p) calculations.

The conformational behavior of DMMP has been studied extensively with ab initio methods [270–272]. Low-energy conformers and rotational barriers for the P-O-C-C dihedral in sarin and soman have also been determined from quantum chemical calculations [273]. In this work, the focus is on developing a reliable approximation of the rotational barriers for use in the development of the TraPPE force field. Structures optimized with HF/6-31G+(d,p) compare favorably with the B3LYP results [271], predicting the lowest energy conformer for DMMP with dihedral angles of -46.93 and -24.81 for the O1=P-O3-C3 and O1=P-O2-C2 dihedrals, respectively. Energetic barriers to dihedral rotation for the O=P-O-CH_3 dihedral in DMMP and the CH_3-CH-O-P dihedral in sarin are shown in Figures 7.2 and 7.3, respectively. For DMMP, additional calculations were performed at the MP2/6-31G+(d,p) level to determine the effect of theory level on the predicted rotational barriers. As shown in Figure 7.2, MP2 and HF theories yield similar values for the O=P-

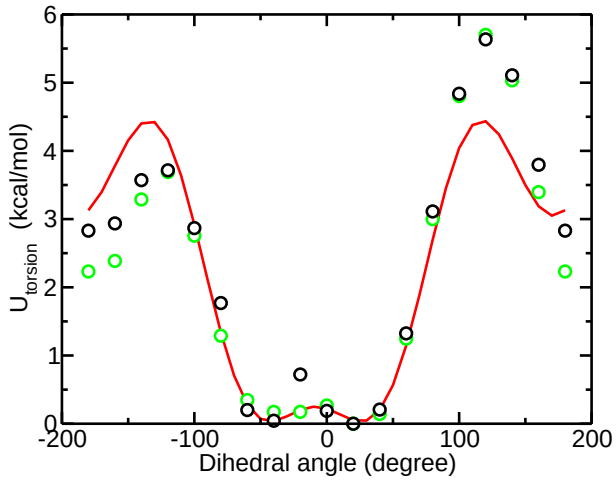

Figure 7.2: Torsional barrier for O=P-O-CH_3 dihedral in DMMP. Prediction of HF/6-31G+(d,p) calculations (black), MP2/6-31G+(d,p) (green) and fit of Equation 7.1 to data (line).

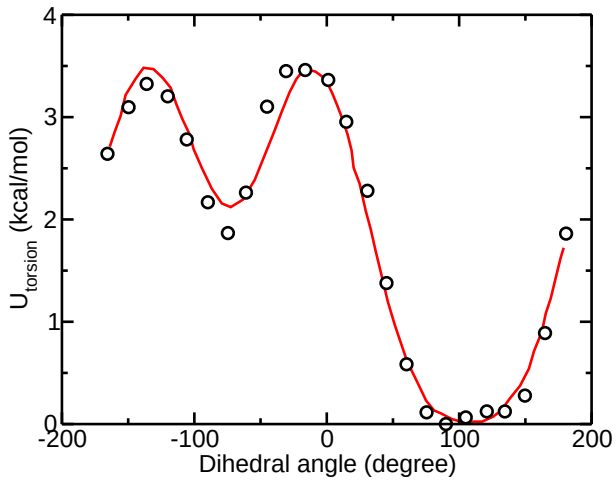

Figure 7.3: Torsional barrier for CH_3-CH-O-P dihedral in sarin. Circles represent the results of HF/6-31G+(d,p) ab inito calculations, while a solid line is used to represent the fit of Equation 7.1 to the ab initio data.

O-CH_3 rotational barriers, which is consistent with similar calculations performed for other phosphorous containing compounds [274]. These combined results demonstrate the inclusion of electron correlation has little effect on the predicted energy minima or rotational barriers. Therfore, scanning dihedral angles with higher level theories and larger basis sets

is not expected to improve the predictive capabilities for the force field. The VN force field uses a slightly different cosine series to describe the torsional behavior

$$U_{torsion} = \sum_{i=1}^{6} V_i(1 + \cos(i\phi)). \tag{7.2}$$

where V_i are the fourier coefficients.

7.2.2 Fluid-solid interactions

Carbon slit pore was used as the adsorbent to simulate the adsorption of DMMP, sarin and soman. The carbon slit pore model consists of two infinite parallel graphitic slab walls separated by a slit shaped pore. Each wall is made up of Lennard-Jones carbon atoms with diameter σ_s and well depth ε_s and treated as a continuum. The wall surfaces are assumed to be homogeneous. The potential of the walls is characterized by the 10-4-3 Steele potential [275].

$$U = 2\pi\rho_s\varepsilon\sigma^2\Delta\left[\frac{2}{5}\left(\frac{\sigma}{z}\right)^{10} - \left(\frac{\sigma}{z}\right)^{4} - \left(\frac{\sigma^4}{3\Delta(z+0.61\Delta)^3}\right)\right] \tag{7.3}$$

where $\rho_s = 0.114$ Å^{-3} is the density of carbon, $\Delta = 3.354$ Å is the spacing between two adjacent graphene layers, z is the perpendicular distance of an adsorbate molecule from the wall, $\varepsilon_s = 28$ K is the well depth and $\sigma_s = 3.4$ Å is the collision diameter of the carbon atom. The solid-fluid cross interaction parameters σ and ε are calculated using the Lorentz-Berthelot combining rules. The carbon slit pore has two carbon walls separated by a width H and the net potential between an adsorbate molecule and the solid walls is given by,

$$\phi(z) = \phi(z) + \phi(H - z) \tag{7.4}$$

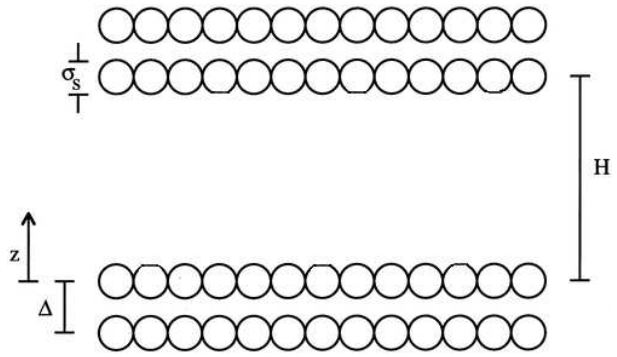

Figure 7.4: Schematic of a carbon slit pore with pore width H

A schematic of the carbon slit pore is given in Figure 7.4.

7.3 Simulation Details

7.3.1 Bulk Fluid Properties

Vapor-liquid coexistence curves, vapor pressures, heats of vaporization, and second virial coefficients were obtained from histogram reweighting Monte Carlo simulations in the grand canonical ensemble [61,64,117]. Insertion of molecules were enhanced through the use of the coupled-decoupled configurational-bias Monte Carlo method [88]. For DMMP and sarin, 10 trial insertions were used for the first atom and 8 trial insertions per site were used for all remaining sites. For soman, 14 trial insertions for the first atom, and 12 trial insertions per site were used for all remaining sites. Increasing the number of attempted trial insertions beyond this was found to have a negligible effect on the fraction of accepted particle transfers. The ratios of attempted moves were set to 60% particle insertions/deletions, 10% configurational-bias regrowths, 15% translations and 15% rotations. A boxlength of 30 Å was used for DMMP and sarin while 35 Å was used for soman.

Lennard-Jones interactions were truncated at 14 Å and standard long-range corrections were applied [276, 277]. Electrostatic interactions were calculated using an Ewald sum with

Table 7.4: Simulation details for VLE calculations

Molecule	T (K)	μ
DMMP	580	3710
	630	4410
	680	4580
	630	4670
	580	4710
	530	4685
	480	4365
	430	3910
	380	3490
Sarin	540	15420
	590	16520
	640	16960
	590	16880
	540	16850
	490	16700
	440	16550
Soman	600	-10500
	650	-8800
	700	-7750
	650	-8500
	600	-9300
	550	-10000
	500	-11000
	450	-11700

tin-foil boundary conditions [112, 123]. All calculations were equilibrated for 1×10^6 Monte Carlo Steps (MCS) followed by production runs of 5×10^7 MCS in the liquid phase and 1×10^7 MCS in the vapor phase. Histograms of number of particles and the energy were collected every 250 MCS during each simulation. Run conditions for all the histograms collected for each compound are listed in Table 7.4. Statistical uncertainties were determined from the standard deviation of results produced by three separate simulations started from different initial configurations and given different random number seeds.

Radial distribution functions and liquid densities at 1 atm at various temperatures were determined with NPT Monte Carlo simulations. Simulations were performed with

250 molecules. The ratio of moves were 1% volume changes, 14% configurational-bias regrowths, 70% translations and 15% rotations. Simulations were equilibrated for 2.5×10^7 MCS, and run statistics were recorded for an additional 2.5×10^7 MCS. All calculations in this work were performed with the Monte Carlo simulation engine Towhee [278].

7.3.2 Adsorption

Grand Canonical Monte Carlo simulation was used to obtain pure adsorption isotherms (pressure vs pore density) of DMMP, sarin and soman for the new force field. In GCMC, the chemical potential, temperature and the volume are fixed. At equilibrium,the chemical potential of the pore and the imaginary particle reservoir (bulk phase) are equal. Each MCS has three attempted moves: displacement of a particle, configurational bias growth and particle swap. The effect of temperature on the adsorption process is also studied by running pure adsorption isotherms at four different temperatures, 300K, 375K, 425K and 475K. For desorption isotherms, the final configuration of a completely filled pore for each compound is used as the initial configuration and pressure is gradually decreased.

Fixed pressure Gibbs ensemble Monte Carlo simulation [122, 214] was used to generate organophosphate-water mixture adsorption isotherms at 300K. In GEMC technique, two simulation cells were used, one representing the pore and the other the coexisting bulk phase. The number of particles , volume of the pore and the temperature were fixed. Unlike GCMC, the pressure of the bulk was fixed. Three types of moves were attempted: displacement or reorientation of a particle, particle interchange between bulk and pore and volume change of the bulk. The ratio of the moves were 0.5% for volume change, 30% for particle interchange and rest for displacement or reorientation. The acceptance rate used for paticle displacement and volume change was 50%. This method allows direct

calculation of the adsorption isotherm and do not require bulk simulations for computing the pressure. A bulk fluid molefraction of 0.5 with 200 molecules of water and 200 molecules of organophosphate was simulated. The system was allowed to equilibrate before any particle interchange moves were attempted.

The simulation cell was bound by the pore walls in the z-direction. A pore width of 20 Å was used for both the mixture and pure component simulations considering the size of the molecules. The x and y dimensions of the cell were 50 Å each. Periodic boundary conditions were applied in the x and y direction. A non-bonded and electrostatic cutoff equal to half the simulation box length with long-range corrections were used in the x-y plane. Coulombic interactions between the adsorbate molecules were determined by the ewald sum technique. The system was equilibrated for 10 million MCS followed by 15 million MCS of sampling.

7.4 Results and Discussion

7.4.1 Condensed Phase Properties

In the case of DMMP, sarin and soman, limited experimental physical property data are available in the open literature [264, 266, 267, 279]. In Table 7.5, the predictions of the TraPPE force field for liquid densities at 1 atm and 298 K for sarin and soman, and 303 and 373 K for DMMP, are listed in comparison with experiment. The maximum deviation from experiment was found for soman, where the liquid density is over-predicted by 4.5%. For DMMP, the TraPPE force field predicts liquid densities at 303 and 373 K that are within 1% of experimental values. At these conditions, the VN force field also provides a reliable estimate of the liquid densities for DMMP.

Vapor-liquid coexistence curves predicted by the TraPPE force field are shown in Fig-

Table 7.5: Liquid densities predicted for DMMP, sarin and soman

Compound	ρ_l(kg/m^3)	Expt ρ_l(kg/m^3)
DMMP (303 K)	1145.6, [1156.2][a]	1150.7 [266]
DMMP (373 K)	1078.0, [1085.3][a]	1071.7 [267]
Sarin (298 K)	1123.4	1088.7 [280]
Soman (298 K)	1067	1022 [280]

[a] Predictions of the VN force field.

ure 7.5, with the predictions of the VN force field for DMMP included for comparison. The phase diagrams for sarin and soman should be considered "hypothetical," since these compounds are known to decompose at temperatures near their normal boiling points. DMMP, sarin and soman are found to exhibit similar phase behavior, but quantitative differences are clearly apparent. Critical temperatures and densities were computed by fitting the saturated liquid and vapor densities to the density scaling law for critical temperature [228]

$$\rho_{liq} - \rho_{vap} = B(T - T_c)^{\beta} \tag{7.5}$$

and the law of rectilinear diameters [229]

$$\frac{\rho_{liq} + \rho_{vap}}{2} = \rho_c + A(T - T_c) \tag{7.6}$$

where $\beta = 0.325$ is the critical exponent for Ising-type fluids in three dimensions [230] and A and B are constants fit to simulation data. The results of these calculations are listed in Table 7.6.

Although the TraPPE and VN force fields yield similar liquid densities at 303 K, the VN force field predicts a T_c that is 100 K higher than TraPPE, illustrating how small

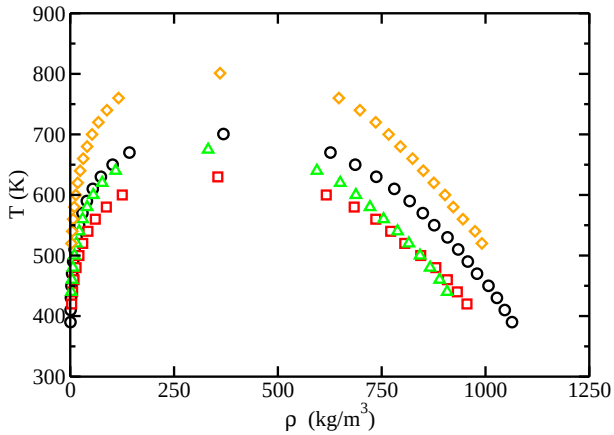

Figure 7.5: Vapor Liquid Equilibria for pure DMMP (circle), DMMP-VN (diamond), sarin (square) and soman (triangle).

Table 7.6: Predicted critical parameters and normal boiling points for DMMP, sarin and soman

Compound	T_c (K)	P_c (bar)	ρ_c (kg/m^3)	T_b (K)	Expt T_b (K)	ω
DMMP	700.6±0.1	49.7±0.1	368.8±0.1	458.4±0.2	454 [264]	0.39
DMMP-VN	801.1±0.2	52.1±0.1	360.7±0.2	515.2±0.8	454 [264]	0.32
Sarin	629.8±0.9	36.1±0.1	355.4±0.1	427.0±0.3	431 [280]	0.40
Soman	674.9±0.3	29.2±0.1	332.0±0.3	467.6±0.6	471 [280]	0.41

differences in force field parameters can have large effects on predicted phase diagrams. Comparison of T_c for DMMP, sarin and soman shows DMMP with a critical temperature 70 K greater than that of sarin, while being only 25 K higher than soman's. Based on these results, DMMP is expected to provide reasonable qualitative, but not quantitative, estimates of sarin and soman phase behavior. Experimental vapor pressures for DMMP are available for $325 \leq T \leq 408$ K and were used in the refinement of the DMMP force field. In Figure 7.6, Clausius-Clapeyron plots for DMMP, sarin and soman are presented along with the experimental vapor pressures.

Through optimization of only the Lennard-Jones ε and σ for the P atom, in DMMP, it was possible to match closely experimental vapor pressures. The vapor pressures from

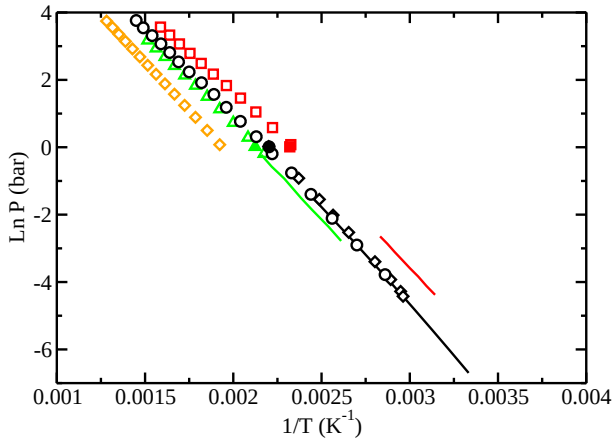

Figure 7.6: Clausius-Clapeyron plot for pure DMMP (circle), DMMP-VN (diamond), sarin (square) and soman (triangle). Line reperesents the experimental vapor pressure of pure DMMP (black) [264, 279], sarin (red) [258] and soman (green) [259]. Black diamonds correspond to new set of experimental vapor pressure of pure DMMP [257] and filled symbols to experimental boiling points [264, 280].

simulation for sarin and soman can be extrapolated to match the experimental values. Normal boiling points were calculated for each molecule. All normal boiling points (see Table 7.6) were within 1.5% of experiment, which is remarkable considering that no additional parameter optimization was performed for sarin or soman. The normal boiling point for DMMP-VN was found to be 515.2, which is a 61.2 K over-prediction compared to experiment. Heats of vaporization were calculated for each molecule as a function of temperature using histogram data collected for the vapor-liquid equilibria calculations and Equation 7.7

$$\Delta H_v = U_v - U_l + p(V_v - V_l) \tag{7.7}$$

where subscripts v and l refer to the vapor and liquid phases, respectively. U is the internal energy per mol and V is the molar volume. The results of these calculations are shown in Figure 7.7. Near 450 K, DMMP and soman were found to have similar heats of vaporization, while ΔH_v for sarin at 450 K was approximately 10 kJ/mol lower. Heats of

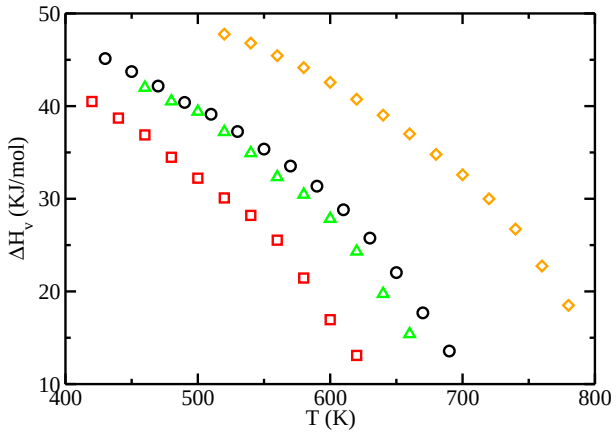

Figure 7.7: Heat of vaporization for DMMP (circle), DMMP-VN (diamond), Sarin (square) and soman (triangle)

Table 7.7: Predicted heats of vaporization for DMMP, sarin and soman

Compound	Temp(K)	Sim (kJ/mol)	Expt (kJ/mol)
DMMP	303	54.27±0.7	52.25 [266, 267]
DMMP (VN)	303	50.11 [263]	
Sarin	298	49.50±0.5	46.89 [280]
Soman	298	53.93±0.3	55.18 [280]

vaporization predicted by the DMMP-VN force field were significantly higher than those predicted by TraPPE, which was due in large part to having a critical temperature 100 K greater than the TraPPE force field. We also computed heats of vaporization at low temperatures where experimental data is available through NVT Gibbs Ensemble Monte Carlo simulation. Histogram reweighting methods were not used for generating this data since the acceptance rate for the insertion move was very low at those temperatures. The values determined are reported in Table 7.7 along with the experimental data. The predicted heats of vaporization are in good agreement with the experiment.

Second virial coefficients were calculated for the TraPPE force field and are listed in

Table 7.8: Second virial coefficients for DMMP, sarin and soman. Units are cm^3/mol

T (K)	650	550	450
DMMP	-455.05	-785.44	-1524.00
Sarin	-424.81	-699.19	-1363.7
Soman	-641.70	-1116.70	-2177.30

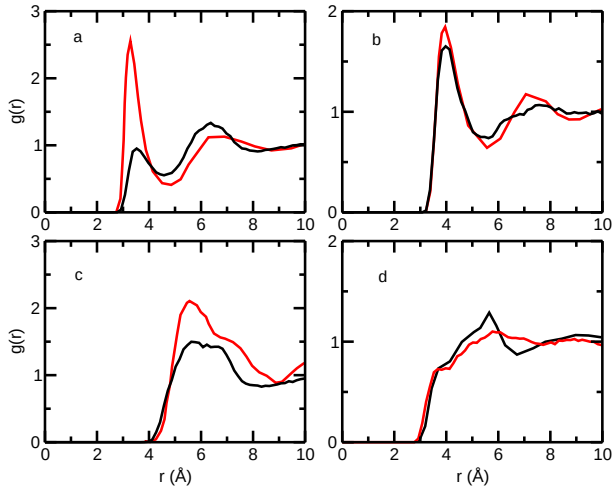

Figure 7.8: Radial distribution function for liquid DMMP at 303 K. New force field (black) and VN force field (red). a)O1-C1 b)C3-C3 c)P-P d)C1-O2.

Table 7.8. The truncated virial expression is given by

$$Z = 1 + \left(\frac{B}{V}\right) \tag{7.8}$$

where $Z = \frac{PV}{RT}$ is the compressibility factor,B is the second virial coefficient and V is the specific volume. Histograms were reweighted for a series of chemical potentials to determine the PVT behavior of the compounds at 450, 550 and 650 K. The resulting data were plotted as $Z - 1$ vs $1/V$. The second virial coefficients were determined by taking the slope of the regression line fit to data. The magnitude of the second virial coefficients, especially near the normal boiling point, illustrates non-ideal behavior in the gas phase.

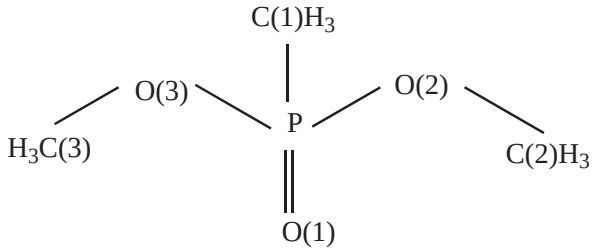

Figure 7.9: Schematic of DMMP

NPT Monte Carlo simulations were used to investigate the liquid phase structure of the TraPPE and VN force fields for DMMP at 303 K and 1.01 bar. Radial distribution functions for various interactions are shown in Figure 7.8 and a schematic of DMMP is presented in Figure 7.9 for reference. Both force fields provided similar results for the C3-C3 and C1-O2 interactions, while significant differences were observed in the O1-C1 interaction. The VN force field predicted a slightly more ordered liquid phase, where DMMP molecules were able to orient themselves to create O1-C1 nearest neighbor interactions. The difference in the O1-C1 rdf predicted by the VN and TraPPE force field was likely due to differences in the bonded interactions, which in the case of the TraPPE force field sterically hinder the formation of O1-C1 nearest neighbor pairs. In the absence of experimental x-ray or neutron scattering data, it is not possible to determine which force field provides a more accurate picture of microscopic structure in DMMP.

7.4.2 Adsorption

Having predicted the bulk condensed phase properties with good accuracy, our next task was to study the physical adsorption characteristics. The pore density was calculated by

$$\rho_{pore} = \frac{< N >}{L_x L_y (H - \sigma_s)} \tag{7.9}$$

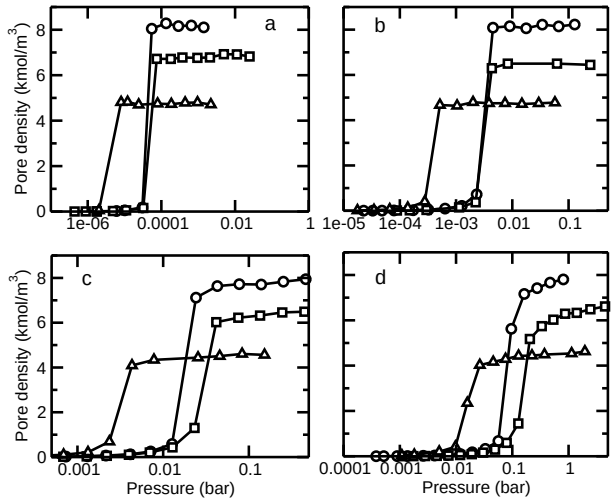

Figure 7.10: Adsorption isotherms of pure DMMP (circle),sarin (square) and soman (triangle) for a 20 Å pore. a) 300 K b) 375 K c) 425 K d) 475K

where $< N >$ is the ensemble average of number of molecules adsorbed in the pore, L_x and L_y are the x and y dimensions of the simulation respectively, H is the pore width and σ_s is the collision diameter of the carbon atom of the adsorbate and has a value of 3.4 Å . Figure 7.10 shows the pure adsorption isotherms of each compound at four different temperatures. DMMP and sarin adsorb almost in the same pressure range whereas soman adsorbs at a lower pressure range. Figure 7.10 clearly shows this behavior. This may be due to the presence of additional methyl groups in soman. The maximum amount adsorbed follows a decreasing order from DMMP to sarin and then soman. This can be attributed to the increase in molecule size (number of functional groups) from DMMP to soman.

Very little adsorption occurs at low pressures (Henry's law region) followed by significant adsorption at high pressures through capillary condensation at temperatures 300 K and 375 K. The vapors of the compounds get adsorbed at low densities and then spontaneously get condensed to a dense liquid state inside the pore. The sudden jump in the pore density occurs at a pressure lower than the saturated vapor pressure. Capillary condensation is a

phenomena in which the bulk vapor-liquid equilibria is altered by confinement in a porous solid. The pore densities have densities similar to the actual bulk liquid densities. For DMMP, the maximum pore density is 8.28 kmol/m^3 at 300 K which is close to the bulk liquid density of 9.27 kmol/m^3 at 303 K. Similarly, for sarin, the maximum pore density at 298 K is 6.92 kmol/m^3 and the bulk liquid density is 7.77 kmol/m^3 at 298 K.

At high temperatures, the adsorption occurs by continuous pore filling starting from low pressures. Visual inspection of the snapshots recorded during the course of the simulation shown in Figure 7.11 and Figure 7.12 for sarin at 300 K and 475 K support this behavior. At 300 K, the pore fills completely in a single step while at 475 K the pore starts to fill gradually from low to high pressures. The molecules are adsorbed on the walls first followed by filling of the volume between the walls. The snapshots presented for sarin are representative of DMMP and soman since similar behavior was observed for them too. Desorption was also carried out for DMMP and sarin at 300 K. Figure 7.13 and 7.14 show desorption isotherms of DMMP and sarin respectively at 300 K. Significant hysteresis which is evident from the asymmetric paths of adsorption and desorption was observed at 300 K for both DMMP and sarin. Hysteresis is a result of capillary condensation and is caused by the metastability in the pore [281, 282]. The desorption curve extends into the liquid region for a wider pressure range and then drops to almost zero pore densities. The maximum pore density decreases while temperature increases indicating there would be no capillary condensation at high temperatures and hysteresis eventually disappears. This has also been demonstrated with an adsorption and desorption simulation of DMMP in a 10 Å pore width at 525 K. Adsorption and desorption isotherms from these simulations are presented in Figure 7.15. There was no deviation of the desorption isotherm from the adsorption curve indicating no

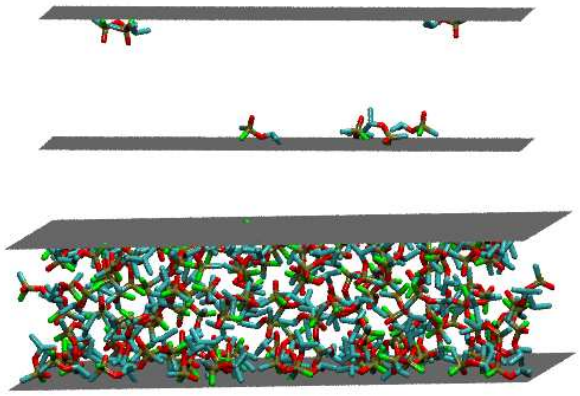

Figure 7.11: Snapshots of adsorption of sarin in 20 Å pore at 300 K. $3x10^{-5}$ bar (top); $5.4x10^{-5}$ bar (bottom).

hysteresis at high temperatures.

It is necessary that we also investigate the adsorption of the compounds in mixture with water since it is more likely that the contaminated air is moist around room temperature. Mixture adsorption isotherms of the organophosphates with water at 300 K are presented in figure 7.16. The figures show that the adsorption of the organophosphates is slightly delayed by the presence of water compared to the pure organophosphate adsorption. The organophosphate is preferentially adsorbed over water at low pressures followed by adsorption of water at high pressures due to high dispersion interactions among the phosphate molecules. Once water molecules starts adsorbing, it forms clusters through hydrogen bonding displacing the phosphate molecules out of the pore resulting in a decreasing trend for phosphate pore density. A snapshot of water-soman adsorption presented in Figure 7.17 shows formation of clusters of water in the pore. Soman molecules are not shown in the figure; the bottom adsorbate wall in gray is shown for reference. So at high pressures, water adsorbs selectively over organophosphates. Instances of hydrogen bonding between the oxygen double bonded to phosphorous atom and the hydrogens of water in the adsorp-

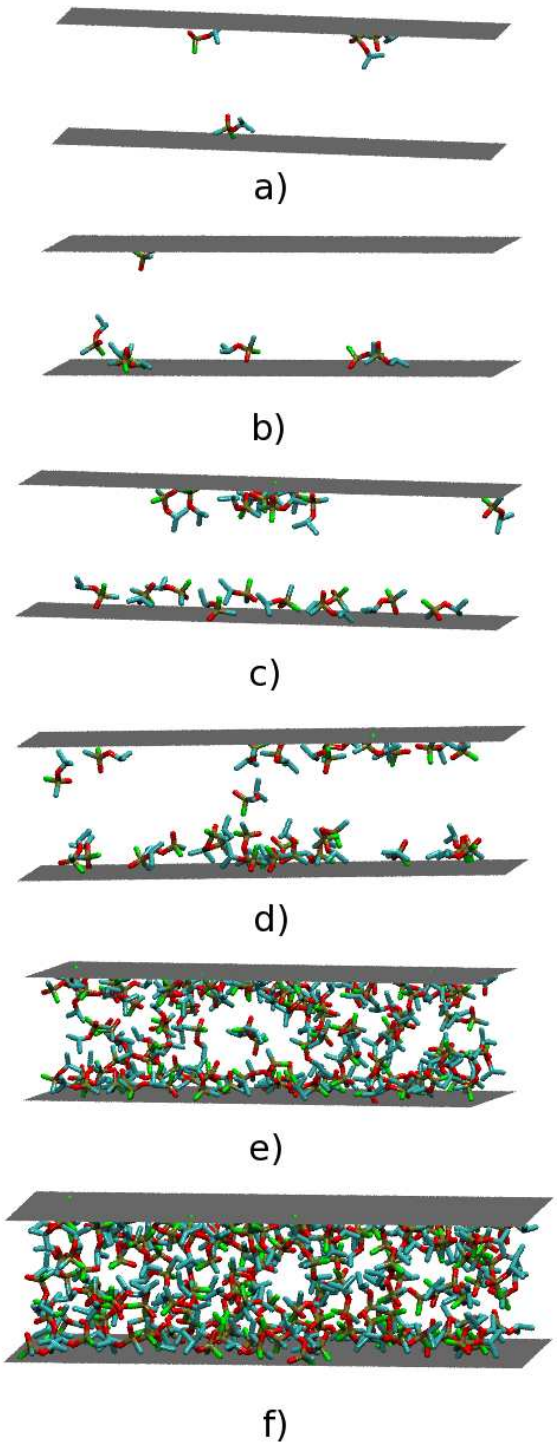

Figure 7.12: Snapshots of adsorption of sarin in 20 Å pore at 475 K. a)1.8x10^{-2} bar; b)4.9x10^{-2} bar; c)7.9x10^{-2} bar; d)12.7x10^{-2} bar; e)20.5x10^{-2} bar; f)86.8x10^{-2} bar.

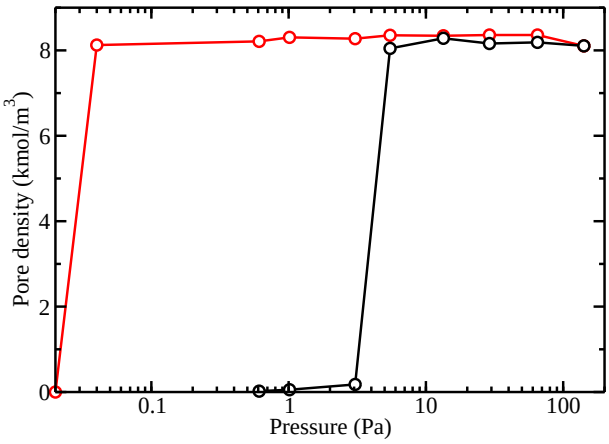

Figure 7.13: Adsorption (black) and desorption (red) isotherms of DMMP in 20 Å pore at 300 K.

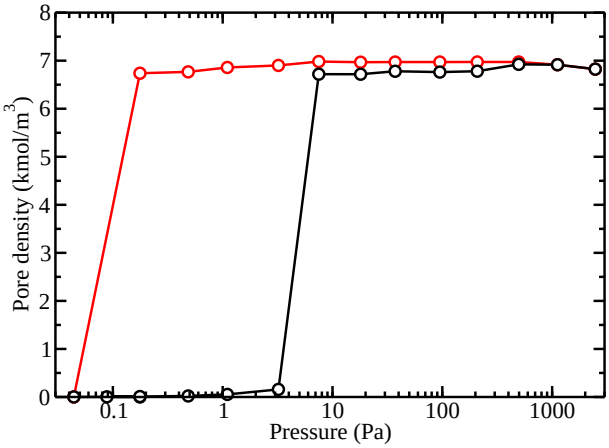

Figure 7.14: Adsorption (black) and desorption (red) isotherms of sarin in 20 Å pore at 300 K.

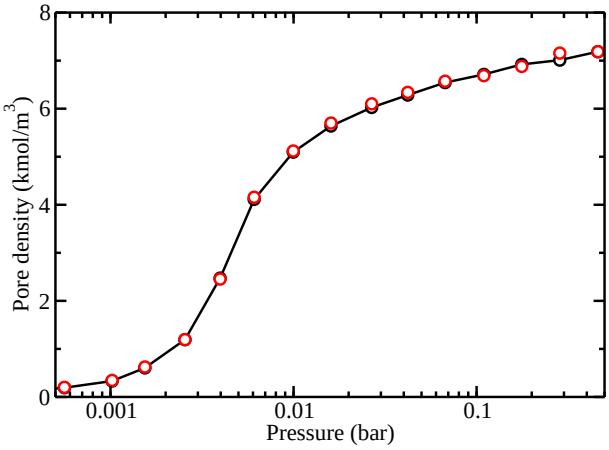

Figure 7.15: Adsorption (black) and desorption (red) isotherms of DMMP in a 10 Åpore at 525 K.

tion of all three compunds were also observed. A snapshot of hydrogen bonding in mixture (soman-water) adsorption at 300 K is shown in Figure 7.18. All molecules are not displayed in the figure to clearly view the bonding sequence.

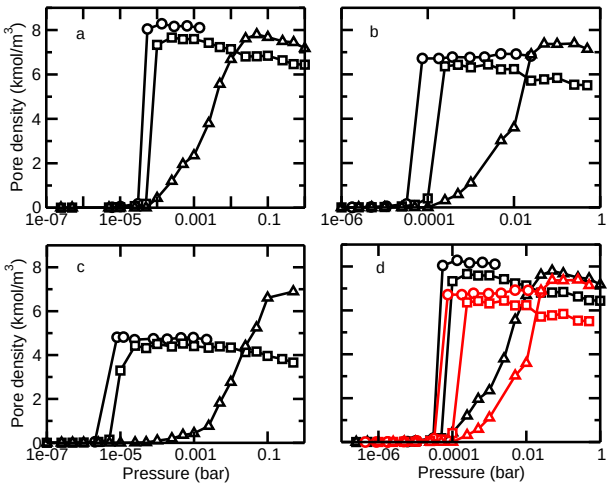

Figure 7.16: Adsorption isotherms of organophosphate-water mixture for a 20 Å pore at 300 K. Pure component (circle); organophosphate from organophosphate-water mixture (square); water from organophosphate-water mixture (triangle). a) DMMP K b) Sarin c) Soman d) DMMP (black) and sarin (red) comparison.

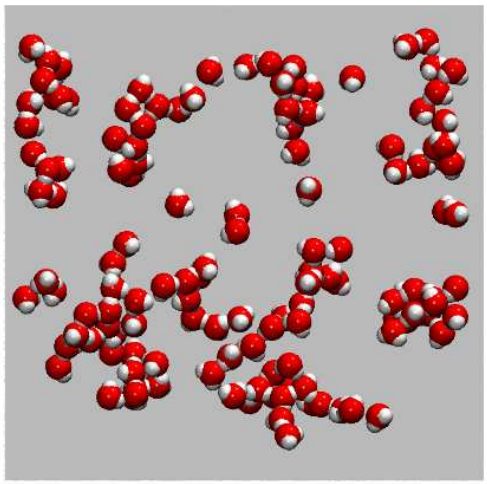

Figure 7.17: Cluster formation of water in adsorption of soman-water mixture in a pore of width 20 Å at 300 K and 0.05 bar seen through the top adsorbate wall in the x-y dimension.

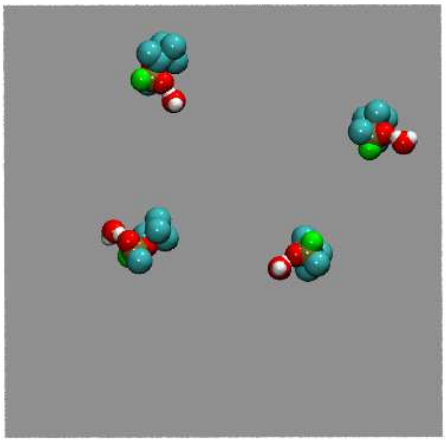

Figure 7.18: Few Hydrogen bonding instances in adsorption of soman-water mixture in a pore of width 20 Å at 300 K and 0.05 bar (Top view of the pore in the x-y dimension).

7.5 Conclusions

The TraPPE force field has been extended to DMMP, sarin and soman. Excellent reproduction of limited experimental data was achieved through the introduction of two additional parameters; the Lennard-Jones σ and ε for the phosphorous atom in DMMP. Although the VN model predicts liquid densities and heat of vaporization in excellent agreement with the experiment, it fails to reproduce the boiling point and vapor pressure. So TraPPE force field for DMMP is better than VN force field considering all the condensed phase properties. Calculations for sarin and soman were performed in predictive mode (with no additional parametrization of the force field), and yielded liquid densities and normal boiling points within 1% of experiment. The hypothetical vapor-liquid coexistence curves and critical parameters are expected to be of use for equation of state modeling of these compounds, which generally rely on knowledge of the critical properties and acentric factor. Pure and mixture adsorption isotherms were also generated. Simulating adsorption has provided molecular level insights into the interactions under confinement. The force fields themselves may be used to study a wide range of topics from adsorption and decomposition in metal oxide substrates to transport and partitioning of chemical agents.

Chapter 8

Conclusions and Future Work

Molecular models or force fields have been developed for extremely hazardous materials such as energetic materials and chemical warfare agents. Major advances in the field of molecular simulation in terms of computer hardware and simulation techniques have made simulation of complex materials and processes a reality which otherwise would have been impossible a decade earlier. Computer simulation has served as a valuable alternative tool for prediction of properties of compounds for which experimental studies are not quite feasible or difficult to carry out. Some simulation methods are used as a preliminary evaluation, screening or testing method before any major experimental process are undergone saving a considerable amount of time and cost. A wide variety of thermophysical properties have been predicted which are in good agreement with the available experimental data. Also, simulations have provided useful insights into the molecular-level interactions and phenomena.

8.1 Energetic Materials

For energetic materials, various condensed phase properties were predicted with the developed force fields. Also, the environmental impact of these compounds was also assessed from the knowledge of partition coefficients. The developed force fields were validated by prediction of solid state properties such as crystal density and lattice parameters since these properties were measured experimentally for all the compounds of interest. The predicted thermophysical properties were in good agreement with the corresponding experimental values.

In this research, all the explosive materials of interest are predicted to be ground-water contaminants. The usage of these compounds may increase in the future leading to severe contamination of the environment. It is necessary to devise mechanisms or techniques for effective removal of these contaminants before they cause major health or ecological problems. Numerous experimental studies have been reported about removal of explosives from the contaminated environment [283–295]. These studies generally focus on different methods for environmental remediation to remove the contaminant explosives. Promising methodologies discussed in these references include adsorption, biodegradation, caltalytic oxidation and alkaline hydrolysis. Recently, experimental studies on adsorption of DNAN in activated carbon has been published [296]. It was demonstrated that 99% of DNAN was removed from the contaminated water. So adsorption is one of the effective methods to treat contaminated water. Also, theoretically adsorption is a well established technique in molecular simulation to selectively remove contaminants from an aqueous solution. So with the developed force field for each explosive and an appropriate model for activated carbon, it is possible to simulate adsorption of these ground-water contaminants.

Gibbs Ensemble technique [121] can be used to adsorb an aqueous solution of the explosive to generate mixture adsorption isotherms. The predicted partition coefficients can also be used as an indicator of adsorption efficiency. The partition coefficients are related to the physical adsorption on solids such as graphitic carbon. The affinity of a compound to adsorb on a solid surface is directly related to its aqueous solubility or octanol-water partition coefficient [297]. When two compounds are in question, the one with a higher hydrophobicity (high octanol-water partition coefficient) have more tendency to adsorb onto the surface from an aqueous solution at a given concentration. Also, diffusion and

transport of the explosives in the aqueous medium can be studied with the developed force fields.

8.2 Chemical Warfare Agents

For chemical warfare agents sarin and soman, the force fields developed were used to predict various condensed phase properties such as phase coexistence properties and liquid densities. The predicted properties were in very good agreement with the available experimental data. The results from this work suggest, DMMP is a very good simulant for sarin. In addition to the condensed phase calculations, adsorption of the CWAs in carbon slit pore was modeled. Pure adsorption isotherms of DMMP, sarin and soman and mixture isotherms of an aqueous solution of the agents were determined.

An interesting follow-up for this research is to do extensive theoretical adsorption studies of the warfare agents. Looking at the effect of pore size and temperature by running simulation for different slit pore widths and temperatures will aid in selecting the optimum pore size and temperature for maximum adsorption of the agents. The effect of adding active functional group sites to homogeneous carbon wall can be studied by simulating adsorption in activated carbon. Adsorption of nerve agents in carbon pores or activated carbon is the preliminary step of prefiltration or concentration prior to their decomposition on metal oxide substrates. Physiosorption is the fundamental phenomena in adsorption through carbon adsorbents.

The nerve agents can be effectively removed from contaminated water or air by decomposing them in metal oxide substrates such as TiO_2, MgO, Al_2O_3 and ZnO to non toxic compounds. With an appropriate model for a metal oxide substrate, mixture adsorption of the contaminated water on the substrate can be simulated. Also, partition coefficients

can be determined for sarin and soman by free energy perturbation and the environmental fate predicitive capability of the force field can be assessed by comparing to the available experimental data. In addition to sarin and soman, force field development can be extended to other nerve agents such as VX.

Appendix A

Table A.1: Parameters for non-bonded interactions for Explicit hydrogen DNAN. Parentheses denote functional group attached to the atom of interest.

Site	σ [Å]	ε [K]	q [e]
C-(O)	3.60	30.7	0.150
C-(N)	3.60	30.7	0.090,0.142
C-(H)	3.60	30.7	-0.165,-0.165,-0.189
H-(C)	2.36	25.45	0.165,0.165,0.189
C-(H_3)	3.60	47	0.132
H(methyl)	2.50	10	0.041
O-(C)	2.80	55	-0.407
N-(O)	2.90	30	0.774,0.723
O-(N)	2.70	42	-0.432

Table A.2: Parameters for non-bonded interactions for Explicit hydrogen MNA. Parentheses denote functional group attached to the atom of interest.

Site	σ [Å]	ε [K]	q [e]
C-(NO)	3.60	30.7	0.194
C-(NH)	3.60	30.7	0.133
C-(H)	3.60	30.7	-0.154,-0.135,-0.135,-0.151
H-(C)	2.36	25.45	0.151,0.135,0.135,0.151
C-(H_3)	3.60	47	0.197
H(methyl)	2.50	10	0.012
N-(O)	2.90	30	0.715
N-(H)	3.26	160	-0.736
O-(N)	2.70	42	-0.454
H-(N)	0.50	12	0.369

Table A.3: Vibration parameters for DNAN and MNA

Bond	Molecule	Bond length [Å]	$k_b/2$ [kcal/mol]
C-C	DNAN,MNA	1.40	528.27,529.35
C-NO	DNAN,MNA	1.45	363.08,361.61
O-N	DNAN,MNA	1.22	866.45,872.54
C-O	DNAN	1.32	480.35
O-CH_3	DNAN	1.41	289.56
C-NH	MNA	1.35	528.94
N-H	MNA	0.99	614.35
N-CH_3	MNA	1.44	413.41

Table A.4: Parameters for non-bonded interactions for United atom DNAN and MNA. Parentheses denote functional group attached to the atom of interest.

Site	σ [Å]	ε [K]	q [e]
CH-(aro)	3.74	48	0
C-(O)	4.50	15	0.150
O-(CH_3)	2.80	55	-0.402
C-(NH)	4.50	15	0.187
N-(CH_3)	3.52	58	-0.730
H-(N)	0	0	0.365
CH_3	3.75	98	0.252^a/0.234^b
C-(NO_2)	4.50	15	0.112^a/0.131^b
N-(O)	3.31	40	0.768^a/0.711^b
O-(N)	2.90	80	-0.440^a/-0.449^b

^{a} DNAN. ^{b} MNA.

Table A.5: Bending parameters for DNAN and MNA

Angle	Molecule	Bond Angle [degree]	$k_\theta/2$ [kcal/mol]
C-C-C	DNAN & MNA	120	189.40
C-C-NO	DNAN & MNA	120	154.80
O-N-C	DNAN & MNA	111.50	167.90
O-N-O	DNAN & MNA	125	181.10
C-C-O	DNAN	120	138.72
C-O-C	DNAN	112	97.94
C-C-NH	MNA	120	145.40
C-NH-C	MNA	112.90	73.90
H-N-CH_3	MNA	112.90	72.90

Table A.6: Torsional parameters for DNAN and MNA

Dihedral	Molecule	n	ψ_0	k_ψ [kcal/mol]
C-C-C-C	DNAN & MNA	2	180	15.230
C-O-C-C	DNAN	1,2	180,180	1.467,0.663
O-N-C-C(ortho)	DNAN	1,2,3,4	0,0,0,0	0.065,-0.202,0.085,0.571
O-N-C-C	DNAN & MNA	1,2	180,180	-0.136,4.351
C-N-C-C	MNA	2,4	180,180	3.003,-0.308

Table A.7: Parameters for non-bonded interactions for DNP. Parentheses denote functional group attached to the atom of interest

Site	σ [Å]	ε [K]	q [e]
C-(H)	3.60	30.7	-0.309
C-(NO_2)	3.60	30.7	0.354
N (ring)	3.20	57	-0.396
N-(H)	3.40	141	-0.023
H-(C)	2.36	25.45	0.206
H-(N)	0.50	12	0.321
N-(O)	2.90	30	0.702
O-(N)	2.70	30	-0.414

Table A.8: Parameters for non-bonded interactions for NTO. Parentheses denote functional group attached to the atom of interest

Site	σ [Å]	ε [K]	q [e]
C-(NO_2)	3.60	30.7	0.408
C-(O)	3.60	30.7	1.689
N (ring)	3.20	57	-0.387
N1-(C)	3.40	141	-0.476
N2-(C)	3.40	141	-0.187
O-(C)	3.05	79	-0.601
H-(N1)	0.50	12	0.349
H-(N2)	0.50	12	0.315
N-(O)	2.90	30	0.722
O-(N)	2.70	42	-0.416

Table A.9: Vibration parameters for DNP

Bond	Bond length [Å]	k_b [Kcal/mol]
C-C	1.40	485.9
C=N	1.30	646.2
N-N	1.30	557.8
N-C	1.34	566.2
C=C	1.35	636.4
C-H	1.07	461.1
C-N(O)	1.43	409.6
N-H	0.99	601.8
N-O	1.18	956.5

Table A.10: Bending parameters for DNP

Bond Angle	Angle [degree]	$k_\theta/2$ [Kcal/mol]
N-C=N	113.43	290.5
C=N-N	111.97	322.8
N-N-C	101.50	317
N-C-N	108.77	296
C-N-C	128.38	75.6
H-N-C	125.73	123.2
N(O)-C-N	120.49	122
O-N-C	117.16	144.8
O-N-O	126.70	182.2

Table A.11: Vibration parameters for NTO

Bond	Bond length [Å]	k_b [Kcal/mol]
N-C	1.35	459.7
C=N	1.25	932
N-N	1.35	435.9
N-C(O)	1.37	428.8
H-N	0.99	611.6
C-N(O)	1.44	377.1
C=O	1.19	1061
N-O	1.18	1041

Table A.12: Bending parameters for NTO

Bond Angle	Angle [degree]	$k_\theta/2$ [Kcal/mol]
N-C=N	121.55	149.8
C=N-N	103.74	2401.5
N-N-C	113.62	314
N-C-N	101.77	1347.1
C-N-C	106.88	2514.4
H-N-C	127.18	73.3
N(O)-C-N	124.47	149.8
O=C-N	129	136.3
O-N-C	118.10	231.2
O-N-O	127.18	182.2

Table A.13: Torsional parameters for DNP and NTO

Dihedral	Molecule	n	ψ_0	k_ψ [Kcal/mol]
C=C-N-N	DNP	1	180	111.60
C-N-N=C				
N-N=C-C	DNP	1	0	134.40
N=C-C=C				
C-C=C-N	DNP	1	180	144.00
C-C=N-N	NTO	1	180	50.62
C=N-N-C	NTO	1	180	69.83
N-C-N-C				
C-N-C=N				
N-NC-N	NTO	1	180	104.60
O-N-C-C	DNP & NTO	1,2	180,180	-0.08,3.29

Table A.14: Parameters for non-bonded interactions for MTNI. Parentheses denote functional group attached to the atom of interest

Site	σ [Å]	ε [K]	q [e]
N-(O)	2.90	30	0.742
O-(N)	2.70	42	-0.404
N(sp2)	3.20	57	-0.529
C(methyl)	3.75	98	0.236
N(ring)	3.40	141	-0.047
C-(NO)	3.60	30.7	0.403,-0.199,0.334

Table A.15: Vibration parameters for MTNI

Bond	Bond length [Å]	k_b [Kcal/mol]
N-O	1.17	1007
C-N(O)	1.44	388.30
C=C	1.35	621.20
C=N	1.27	723.70
C-N	1.34	535.40
C-N(sp2)	1.35	514.10
N-C(sp2)	1.33	529.40
N-C(H_3)	1.47	325.30

Table A.16: Bending parameters for MTNI

Bond Angle	Angle [degree]	$k_\theta/2$ [Kcal/mol]
O-N-O	126.70	182.20
O-N-C	117.12,116.47,118.01	148.50,116.50,140.20
N-C=C	131.50	110.80
N-C-N	123.13	160.40
C=C-N	107.37	296.70
C-N-C	103.50	337.70
C-N-C(H_3)	130.60	130.60
N-C=N	114.46	283.70

Table A.17: Torsional parameters for MTNI

Dihedral	n	ψ_0	k_ψ [Kcal/mol]
N=C-N-C	1	180	123.40
C-N-C=C	1	180	143.80
N-C=C-N	1	180	125.30
C=C-N=C	1	180	134.80
C-N=C-N	1	180	126.20
O-N-C-N	1,2	180,180	-0.059,1.218
O-N-C=C	1,2,3	0,0,0	0.065,0.584,-0.070

Table A.18: Parameters for non-bonded interactions for TATB. Parentheses denote functional group attached to the atom of interest

Site	σ [Å]	ε [K]	q [e]
C-N(O)	3.60	30.7	0.061
C-N(H)	3.60	30.7	0.076
N-(O)	2.90	30	1.131
N-(H)	3.26	160	-1.110
O-(N)	2.70	42	-0.548
H-(N)	0.50	12	0.519

Table A.19: Vibration parameters for TATB

Bond	Bond length [Å]	k_b [Kcal/mol]
O-N	1.20	872.66
N-H	1.01	614.44
C-N(O)	1.43	361.66
C-N(H)	1.32	529.23
C-C	1.43	529.43

Table A.20: Bending parameters for TATB

Bond Angle	Angle [degree]	$k_\theta/2$ [Kcal/mol]
H-N-C	119.80	73.86
O-N-O	125.00	181.13
H-N-H	120.4	72.9
O-N-C	117.5	167.91
C-C-C	120	189.41
N(H)-C-C	120	145.43
N(O)-C-C	120	154.81

Table A.21: Torsional parameters for TATB

Dihedral	n	ψ_0	k_ψ [Kcal/mol]
C-C-C-C	2	180	15.230
O-N-C-C	1,2,3,4	180,180,180,180	0.023,4,755,0.017,-1.014
H-N-C-C	1,2,3,4	0,180,0,180	0.023,3.015,-0.451,0.119

References

[1] Pennington, J. C.; Brannon, J. M. *Thermochim. Acta*, **2002**, 384, 163.

[2] Best, E. P. H.; Sprecher, S. L.; Larson, S.; Fredrickson, H. L.; Bader, D. F. *Chemosphere*, **1999**, 39, 2057.

[3] Sheremata, T. W.; Halasz, A.; Paquet, L.; Thiboutot, S.; Ampleman, G.; Hawari, J. *Environ. Sci. Technol.*, **2001**, 35, 1037.

[4] Gong, P.; Sunahara, G.; Rocheleau, S.; Dodard, S. G.; Robidoux, Y.; Hawari, J. *Chemosphere*, **2004**, 56, 653.

[5] Brodman, B. W.; Lee, S. *Bioremediation of nitrogenous contaminants*, **2005**, US Patent No. 6936456.

[6] Yang, Y. -C.; Baker, J. A.; Ward, J. R. *Chem. Rev.*, **1992**, 92, 1729.

[7] Kingery, A. F.; Allen, H. E. *Toxicol. Environ. Chem.*, **1995**, 47, 155.

[8] Bartelt-Hunt, S. L.; Barlaz, M. A.; Knappe, D. R. U.; Kjeldsen, P. *Environ. Sci. Technol.*, **2006**, 40, 4219.

[9] Akhavan, J. *The Chemistry of Explosives*, **1998**, Springer: New York.

[10] Urbanski, T. *Chemistry and Technology o Explosives*, **1964**, The Macmillan Company: New York.

[11] *Report of the Defense Science Board Task Force on Unexploded Ordnance*, **2003**, Office of the Under Secretary of Defense for Acquisition, Technology and Logistics: Washington, DC.

[12] Sangster, J. *Octanol-Water Partition Coefficients: Fundamentals and Physical Chemistry*, **1997**, Vol.2 of Wiley Series in Solution Chemistry, John Wiley & Sons Ltd.

[13] Leo, A.; Hansch, C.; Elkins, D. *Chem. Rev.*, **1971**, 71, 525.

[14] Leo, A. *CLOGP*, Daylight Chemical Information Systems, Mission Viejo, CA.

[15] Leo, A. *Chem. Rev.*,**1993**, 30, 1283.

[16] Klopman, G.; Iroff, L. D. *J. Comput. Chem.*, **1981**, 2, 157.

[17] Rekker, R. F.; Manhold, R. *Calculation of Drug Lipophilicity*, **1992**, VCH: New York.

[18] Suzuki, T.; Kudo, Y. *J. Comput. Aided Mol. Des.*, **1990**, 4, 155.

[19] Rekker, R. F.; De Kort, H. M. *Eur. J. Med. Chem. - Chim. Ther.*, **1979**, 14, 479.

[20] Broto, P.; Moreau, G.; Vandycke, C. *Eur. J. Med. Chem. Chim. Ther.*, **1984**, 19, 71.

[21] Ghose, A. K.; Crippen, G. M. *J. Comput. Chem.*, **1986**, 7, 565.

[22] Hansch, C.; Anderson, S. M. *J. Org. Chem.*, **1967**, 32, 2583.

[23] Hansch, C.; Leo, A. *Exploring QSAR Fundamentals and Applications in Chemistry and Biology*, **1995**, ACS: Washington DC.

[24] Bodor, N.; Gabanyi, Z.; Wong, C. *J. Am. Chem. Soc.*, **1989**, 111, 3783.

[25] Kantola, A.; Villar, H. O.; Loew, G. H. *J. Comput. Chem.*, **1991**, 12, 681.

[26] Famini, G. R.; Penski, C. A.; Wilson, L. Y. *J. Phys. Org. Chem.*, **1992**, 5, 395.

[27] Moriguchi, I.; Hirono, S.; Liu, Q.; Nakagome, I.; Matsushita, Y. *Chem. Pharm. Bull.*, **1992**, 40, 127.

[28] Ghasemi, J.; Saaidpour, S. *Anal. Chim. Acta*, **2007**, 604, 99.

[29] Doweyko, A.M. *J. Comput.-Aided Mol. Des.*, **2004**, 18, 587.

[30] Hughes, L.D.; Palmer, D.S.; Nigsch, F.; Mitchell, J.B. *J. Chem. Inf. Model.*, **2008**, 48, 220.

[31] Still, W. C.; Tempczyk, A.; Hawley, R .C.; Hendrickson, T. F. *J. Am. Chem. Soc.*, **1990**, 112, 6127.

[32] Jean-Charles, A.; Nicholls, A.; Sharp, K.; Honig, B.; Tempczyk, A.; Hendrickson, T. F.; Still, W. C. *J. Am. Chem. Soc.*, **1991**, 113, 1454.

[33] Hawkins, G. D.; Liotard, D. A.; Cramer, C. J.; Truhlar, D. G. *J. Org. Chem.*, **1998**, 63, 4305.

[34] Klamt, A.; Jonas, V.; Buerger, T.; Lohrenz, J. C. W. *J. Phys. Chem. A*, **1998**, 102, 5074.

[35] Giesen, D. J.; Gu, M. Z.; Cramer, C. J.; Truhlar, D. G. *J. Org. Chem.*, **1996**, 61, 8720.

[36] Best, S. A.; Merz Jr., K. M.; Reynolds, C. H. *J. Phys. Chem. B*, **1997**, 101, 10479.

[37] Kollman, P. *Chem. Rev.*, **1993**, 93, 2395.

[38] Straatsma, T. P.; McCammon, J. A. *Annu. Rev. Phys. Chem.*, **1992**, 43, 407.

[39] Duffy, E. M.; Jorgensen, W. L. *J. Am. Chem. Soc.*, **2000**, 122, 2878.

[40] Marrs, T. C.; Maynard, R. L.; Sidell, F. R. *Chemical Warfare Agents - Toxicology and Treatment*, **1996**, John Wiley & Sons Ltd: England.

[41] Noort, D.; Hulst, A. G.; Jansen, R. *Arch. Toxicol.*, **2002**, 76, 83.

[42] Benschop, H. P.; De Jong, L. P. A. *Neurosci. Biobehav. Rev.*, **1991**, 15, 73.

[43] Zhou, T.; Yu, B.; Shiu, E.; Levon, K. *Anal. Chem.* **2004**, 76, 2689.

[44] Prathish, K. P.; Prasad, K.; Prasada Rao, T.; Suryanarayana, M. V. S. *Talanta*, **2007**, 71, 1976.

[45] Hopkins, A. R.; Lewis, N. S. *Anal. Chem.*, **2001**, 73, 884.

[46] Arduini, F.; Amine, A.; Moscone, D.; Ricci, F.; Palleschi, G. *Anal. Bioanal. Chem.* **2007**, 388, 1049.

[47] Oh, S.W.; Kim, Y. H.; Yoo, D. J.; Oh, S. M.; Park, S. J. *Sens. Actuators B* **1993**, 13/14, 400.

[48] Tomchenko, A. A.; Harmer, G. P.; Marquis, B. T. *Sens. Actuators B* **2005**, 108, 41.

[49] Brunol, E.; Berger, F.; Fromm, M.; Planade, R. *Sens. Actuators B* **2006**, 120, 35.

[50] Zuo, G.; Li, X.; Li, P.; Yang, T.; Wang, Y.; Cheng, Z.; Feng, S. *Analytica Chimica Acta* **2006**, 580, 123.

[51] Ponzoni, A.; Baratto, C.; Bianchi, S.; Comini, E.; Ferroni, M.; Pardo, M.; Vezzoli, M.; Vomiero, A.; Faglia, G.; Sberverglieri. G. *IEEE Sensors Journal* **2008**, 8, 735.

[52] Guo, X.; Yoshinobu, J.; Yates Jr., J. T. *J. Phys. Chem.* **1990**, 94, 6839.

[53] Templeton, M. K.; Weinberg, W. H. *J. Amer. Chem. Soc.* **1985**, 107, 97.

[54] Mitchell, M. B.; Sheinker, V. N.; Mintz, E. A. *J. Phys. Chem. B* **1997**, 101, 11192.

[55] Rusu, C. N.; Yates Jr., J. T. *J. Phys. Chem. B* **2000**, 104, 12292.

[56] Kim, C. S.; Lad, R. J.; Tripp, C. P. *Sens and Actuators B* **2001**, 442.

[57] Kanan, S. M.; Tripp, C. P. *Langmuir* **2001**, 2213.

[58] Kanan, S. M.; Tripp, C. P. *Langmuir* **2002**, 722.

[59] Karwacki, C.J.; Tevault, D.E.; Mahle, J.J.; Buchanan, J.H.; Buettner, L.C. *Langmuir*, **1999**, 15, 6343.

[60] Panagiotopoulos, A.Z.; Quirke, N.; Stapleton, M.; Tildesley, D.J. *Mol. Phys.*, **1988**, 63, 527.

[61] Potoff, J.J.; Panagiotopoulos, A.Z. *J. Chem. Phys.*, **1998**, 109, 10914.

[62] Kofke, D.A. *J. Chem. Phys.*, **1993**, 98, 4149.

[63] Fern, J.T.; Keffer, D.J.; Steele, W.V. *J. Phys. Chem. B*, **2007**, 111, 3469.

[64] Ferrenberg, A.M.; Swendsen, R.H. *Phys. Rev. Lett.*, **1988**, 61, 2635.

[65] Ferrenberg, A.M.; Landau, D.P.; Swendsen, R.H. *Phys. Rev. E*, **1995**, 51, 5092.

[66] Damm, W.; Frontera, A.; TiradoRives, J.; Jorgensen, W.L. *J. Comput. Chem.* **1997**, 18, 1955.

[67] Damm, W.; Halgren, T.A.; Murphy, R.B.; Smondyrev, A.M.; Friesner, R.A.; Jorgensen, W.L. *Abstr. Paper Am. Chem. Soc.*, **2002**, 224, U471.

[68] Halgren, T.A.; Murphy, R.B.; Jorgensen, W.L.; Friesner, R.A. *Abstr. Paper Am. Chem. Soc.*, **2000**, 220, U227.

[69] Jorgensen, W.L.; McDonald, N.A. *Theochem-J. Mol.Struct.*, **1998**, 424, 145.

[70] Jorgensen, W.L.; Tirado-Rives, J. *Abstr. Paper Am. Chem. Soc.*, **1998**, 216, U696.

[71] Kaminski, G.A.; Friesner, R.A.; Tirado-Rives, J.; Jorgensen, W.L. *J. Phys. Chem. B*, **2001**, 105, 6474.

[72] Kaminski, G.A.; Friesner, R.A.; Tirado-Rives, J.; Jorgensen, W.L. *Abstr. Paper Am. Chem. Soc.*, **2000**, 220, U279.

[73] Mcdonald, N.A.; Jorgensen, W.L. *J. Phys. Chem. B*, **1998**, 102, 8049.

[74] Price, M.L.P.; Ostrovsky, D.; Jorgensen, W.L. *J. Comput. Chem*, **2001**, 22, 1340.

[75] Rizzo, R.C.; Jorgensen, W.L. *J. Am. Chem. Soc.*, **1999**, 121, 4827.

[76] Luo, R.; Wang, J.M.; Kollman, P.A. *Abstr. Paper Am. Chem. Soc.*, **2002**, 224, U470.

[77] Wang, J.M.; Wolf, R.M.; Caldwell, J.W.; Kollman, P.A.; Case, D.A. *J. Comput. Chem.*, **2005**, 26, 114.

[78] Yang, L.J.; Tan, C.H.; Hsieh, M.J.; Wang, J.M.; Duan, Y.; Cieplak, P.; Caldwell, J.; Kollman, P.A.; Luo, R. *J. Phys. Chem. B*, **2006**, 110, 13166.

[79] Foloppe, N.; Mackerell, A.D. *J. Comput. Chem.*, **2000**, 21, 86.

[80] Foloppe, N.; Mackerell, A.D. *Abstr. Paper Am. Chem. Soc.*, **1997**, 214, 236.

[81] Guvench, O.; Greene, S.N.; Kamath, G.; Brady, J.W.; Venable, R.M.; Pastor, R.W.; MacKerell, A.D. *J. Comput. Chem.*, **2008**, 29, 2543.

[82] Kamath, G.; Greene, S.; Guvench, O.; Pastor, R.; Brady, J.; MacKerell, A.D. *Biophys. J.*, **2007**, 566a.

[83] Kamath, G.; Guvench, O.; MacKerell, A.D. *J. Chem. Theory Comput.*, **2008**, 4, 765.

[84] Oostenbrink, C.; Villa, A.; Mark, A.E.; Van Gunsteren, W.F. *J. Comput. Chem.*, **2004**, 25, 1656.

[85] Delhommelle, J.; Tschirwitz, C.; Ungerer, P.; Granucci, G.; Millie, P.; Pattou, D.; Fuchs, A.H. *J. Phys. Chem. B*, **2000**, 104, 4745.

[86] Martin M. G.; Siepmann, J. I.; *J. Phys. Chem. B*, **1998**, 102, 2569.

[87] Chen, B.; Siepmann, J. I.; *J. Phys. Chem. B*, **1999**, 103, 5370.

[88] Martin M. G.; Siepmann, J. I.; *J. Phys. Chem. B*, **1999**, 103, 4508.

[89] Wick, C. D.; Martin, M. G.; Siepmann, J. I.; *J. Phys. Chem. B*, **2000**, 104, 8008.

[90] Chen, B.; Potoff, J. J.; Siepmann, J. I.; *J. Phys. Chem. B*, **2001**, 105, 3093.

[91] Stubbs, J. M.; Potoff, J. J.; Siepmann, J. I.; *J. Phys. Chem. B*, **2004**, 108, 17596.

[92] Wick, C. D.; Stubbs, J. M.; Rai, N.; Siepmann, J. I.; *J. Phys. Chem. B*, **2005**, 109, 18974.

[93] Lubna, N.; Kamath, G.; Potoff, J. J.; Rai, N.; Siepmann, J. I.; *J. Phys. Chem. B*, **2005** 109, 24100.

[94] Rai, N.; Siepmman, J. I.; *J. Phys. Chem. B*, **2007**, 111, 10790.

[95] Zhang, L.; Siepmann, J. I.; *J. Phys. Chem. B*, **2005**, 109, 2911.

[96] Kamath, G.; Cao, F.; Potoff, J.J. *J. Phys. Chem. B*, **2004**, 108, 14130.

[97] Kamath, G.; Georfiev, G. Potoff, J.J. *J. Phys. Chem. B*, **2005**, 109, 19463.

[98] Potoff, J.J.; Siepmann, J.I. *AIChE J.*, **2001**, 47, 1676.

[99] Kamath, G.; Lubna, N.; Potoff, J.J. *J. Chem. Phys.*, **2005**, 123, 124505.

[100] Lorentz, H. A. *Ann. Phys.*, **1881**, 12, 127.

[101] Berthelot, D. C. *R. Hebd. Seanc. Acad. Sci. (Paris)*, **1898**, 126, 1703.

[102] Mulliken, R.S. *J. Chem. Phys.*, **1955**, 23, 1833.

[103] Reed, A.E.; Weinstock, R.B.; Weinhold, F. *J. Chem. Phys.*, **1985**, 83, 735.

[104] Kar, T.; Sannigrahi, A.B. *Theochem-J. Mol. Struct.*, **1988**, 42, 47.

[105] Besler, B.H.; Merz, K.M.; Kollman, P.A. *J. Comput. Chem*, **1990**, 11, 431.

[106] Chirlian, L.E.; Francl, M.M. *J. Comput. Chem.*, **1987**, 8, 894.

[107] Breneman, C.M.; Wilberg, K.B. *J. Comput. Chem*, **1990**, 11, 361.

[108] Woods, R.J.; Khalil, M.; Pell, W.; Moffat, S.H.; Smith, V.H. *J. Comput. Chem.*, **1990**, 11,297.

[109] Gaussian 03, Revision A.1 , Frisch, M. J.; Trucks, G. W.; Schlegel, H. B.; Scuseria, G. E.; Robb, M. A.; Cheeseman, J. R.; Montgomery, Jr., J. A.; Vreven,Englewood Cliffs, NJ, T.; Kudin, K. N.; Burant, J. C.; Millam, J. M.; Iyengar, S. S.; Tomasi, J.; Barone, V.; Mennucci, B.; Cossi, M.; Scalmani, G.; Rega, N.; Petersson, G. A.; Nakatsuji, H.; Hada, M.; Ehara, M.; Toyota, K.; Fukuda, R.; Hasegawa, J.; Ishida, M.; Nakajima, T.; Honda, Y.; Kitao, O.; Nakai, H.; Klene, M.; Li, X.; Knox, J. E.; Hratchian, H. P.; Cross, J. B.; Adamo, C.; Jaramillo, J.; Gomperts, R.; Stratmann, R. E.; Yazyev, O.; Austin, A. J.; Cammi, R.; Pomelli, C.; Ochterski, J. W.; Ayala, P.

Y.; Morokuma, K.; Voth, G. A.; Salvador, P.; Dannenberg, J. J.; Zakrzewski, V. G.; Dapprich, S.; Daniels, A. D.; Strain, M. C.; Farkas, O.; Malick, D. K.; Rabuck, A. D.; Raghavachari, K.; Foresman, J. B.; Ortiz, J. V.; Cui, Q.; Baboul, A. G.; Clifford, S.; Cioslowski, J.; Stefanov, B. B.; Liu, G.; Liashenko, A.; Piskorz, P.; Komaromi, I.; Martin, R. L.; Fox, D. J.; Keith, T.; Al-Laham, M. A.; Peng, C. Y.; Nanayakkara, A.; Challacombe, M.; Gill, P. M. W.; Johnson, B.; Chen, W.; Wong, M. W.; Gonzalez, C.; and Pople, J. A.; Gaussian, Inc., Pittsburgh PA, 2003.

[110] Yin, D.X.; MacKerell, A.D. *J. Comput. Chem.*, **1998**, 19,334.

[111] Ketko, M.H.; Potoff, J.J. *Molec. Sim.*, **2007**, 33, 769.

[112] Allen, M.P.; Tildesley, D.J. *Computer Simulation of Liquids*, **1987**, Clarendon Press: Oxford.

[113] Martin M. G.; Siepmann, J. I. *J. Phys. Chem. B*, **1999**, 103, 4508.

[114] Zwanzig, R.W. *J. Chem. Phys.*, **1954**, 22, 1420.

[115] Straatsma, T.P.; McCammon, J.A. *J. Chem. Phys.*, **1991**, 95, 1175.

[116] Postma, J.P.M.; Berendsen, H.J.C.; Haak, J.R. *Faraday Symp. Chem. Soc.*, **1982**, 17,55.

[117] Ferrenberg, A.M.; Swendsen, R.H. *Phys. Rev. Lett.*, **1989**, 63, 1195.

[118] Phillips, J. C.; Braun, R.; Wang, W.; Gumbart, J.; Tajkhorshid, E.; Villa, E.; Chipot, C.; Skeel, R. D.; Kale, L.; Schulten, K. *J. Comp. Chem.*, **2005**, 26, 1781.

[119] Martyna, G. J.; Tobias, D. J.; Klein, M. L. Constant pressure molecular dynamics algorithms *J. Chem. Phys.*, **1994**, 101, 4177.

[120] Feller, S. W.; Zhang, Y.; Pastor, R. W.; Brooks, B. R. *J. Chem. Phys.*, **1995**, 103, 4613.

[121] Panagiotopoulos, A.Z. *Mol. Phys.*, **1987**, 62, 701.

[122] Mcgrother, S.C.; Gubbins, K.E. *Mol. Phys.*, **1999**, 97, 955.

[123] Ewald, P.P. *Ann. Phys.*, **1921**, 64, 253.

[124] Toukmaji, A.Y.; Board, Jr. J.A. *Comput. Phys. Commun.*, **1996**, 95, 73.

[125] Eastwood, J.W.; Hockney, R.W. *J. Comp. Phys.*, **1974**, 16, 342.

[126] Lunazzi, L.; Magagnoli, C.; Macciantelli, D. *J. Chem. Soc. Perkin Trans. 2* **1980**, 1704.

[127] Spellmeyer, D.C.; Grootenhuis, J.; Miller, M.D.; Kuyper, L.F.; Kollman, P.A. *J. Phys. Chem.* **1990**, 94, 4483.

[128] Head-Gordon, M.; Pople, J.A. *Chem. Phys. Lett.* **1990**, 173, 585.

[129] Birkett, H.E.; Cherryman, J.C, Chippendale, A.M.; Hazendonk, P.; Harris, R.K. *J. Mol. Struct.* **2002**, 602-603, 59.

[130] Bzhezovskii, V.M.; Kapustin, E.G.; Il'chenko, N.N. *Russ. J. Gen. Chem.* **2003**, 73, 1585.

[131] Høg, J.N.; Nygaard, L.; Sorensen, G.O. *J. Mol. Struct.* **1971**, 7, 111.

[132] Correl, T.; Larsen, N.W.; Pedersen, T. *J. Mol. Struct.* **1980**, 65, 43.

[133] Carreira, L.A.; Towns, T.G. *J. Mol. Struct.* **1977**, 41, 1.

[134] Glenewinkel-Meyer, Th.; Crim, F.F. *J. Mol. Struct.* **1995**, 337, 209.

[135] Domenicano, A.; Schultz, G.; Hargittai, I.; Colapietro, M.; Portalone, G.; George, P.; Bock, C.W. *Struct. Chem* **1990**, 1, 107.

[136] Borisenko, K.B.; Bock, C.W.; Hargittai, I. *J. Phys. Chem.* **1994**, 98, 1442.

[137] Borisenko, K.B.; Hargittai, I. *J. Mol. Struct.* **1996**, 382, 171.

[138] Leavell, S.; Curt, R.F. Jr. *J. Mol. Spectrosc.* **1975**, 45, 428.

[139] Quack, M.; Stockburger, M. *J. Mol. Spectrosc.* **1972**, 43, 87.

[140] Larsen, N.W.; Hansen, E.L.; Nicolaisen, F.M. *Chem. Phys. Lett.* **1976**, 43, 1976.

[141] Allen, G.; Fewster, S. *Internal rotations in Molecules* Wiley: New York **1974**, Chapter 8.

[142] Buchanan, G; Montaudo, G.; Finocchiaro, P. *Can. J. Chem.* **1974**, 52, 767.

[143] Contreras, R.H.; Ferraro, M.B.; de Kowalewski, D.G. *Magn. Reson. Chem.* **1985**, 23, 296.

[144] Biekofsky, R.R.; Pomilio, A.B.; Contreras, R.H.; de Kowalewski, D.G.; Facelli, J.C. *Magn. reson. Chem.* **1989**, 27, 158.

[145] Crecely, R.W.; McCracken, K.W.; Goldstein, J.H. *Tetrahedron* **1969**, 25, 877.

[146] Punte G.; Rivero, B.E.; Cerdeira, S.; Nudelman, N.S. *Can. J. Chem.* **1990**, 68, 298.

[147] Manaa, M.R.; Gee, R.H.; Fried, L.E. *J. Phys. Chem.* **2002**, 106, 8806.

[148] Owens, F.J. *J. Mol. Struct. (Theochem)*, **1996**, 370, 11.

[149] Murray, J.S.; Politzer, P. *Chemistry and Physics of Energetic Materials*, **1990**, Kluwer: Dordrecht, The Netherlands.

[150] Politzer, P.; Murray, J.S. *J. Mol. Struct.*, **1996**, 376, 419.

[151] Xiao, H.-M.; Fan, J.-F.; Gu, Z.-M.; Dong, H.-S. *J. Chem. Phys.*, **1998**, 226, 15.

[152] Rice, B.M.; Sahu, S.; Owens, F.J. *J. Mol. Struct. (Theochem)*, **2002**, 583, 69.

[153] Brill, T.B.; James, K.J. *J. Phys. Chem.*, **1993**, 97, 8752.

[154] Brill, T.B.; James, K.J. *Chem. Rev.*, **1993**, 93, 2667.

[155] Brill, T.B.in Bulusu, S.N. (ed) *Chemistry and Physics of Energetic Materials*, **1990**, ch. 13, Kluwer: Dordrecht, The Netherlands.

[156] Adams, G.F.; Shaw, Jr., R.W. *Annu. Rev. Phys. Chem.*, **1992**, 43, 311.

[157] Botcher, T.R.; Wight, C.A. *J. Phys. Chem.*, **1994**, 98, 5441.

[158] Oxley, J.C.; Smith, J.L.; Ye, H.; McKenney, R.L.; Bolduc, P.R. *J. Phys. Chem.*, **1995**, 99, 9593.

[159] Dobratz, B.M. Report No. LA-13014-H, **1995**.

[160] Nyburg, S.C.; Faerman, C.H.; Prasad, L.; Palleros, D.; Nudelman, N. *Acta Cryst.* **1987**, C43, 686.

[161] Spellmeyer, D.C.; Grootenhius, P.D.J.; Miller, M.D.; Kuyper, L.F.; Kollman, P.A *J. Phys. Chem*, 1990, 94, 4483.

[162] Panunto, T.W.; Urbánczyck-Lipkowska.; Johnson, R.; Etter, M.C. *J. Am. Chem. Soc.* **1987**, 109, 7786.

[163] Lister, D.G.; Lister, J.K. *Chem. Commun.* **1966**, 6, 152.

[164] Lister, D.J.; Tyler, J.K.; Hog, J.H.; Larsen, N.W. *J. Mol. Struct.* **1974**, 23, 253.

[165] Fukuyo, M.; Hirotsu, K.; Higuchi, T. *Acta Crystallogr.* **1982**, 38, 643.

[166] Wang, Y.; Saebo, S.; Pittman Jr., C.U. *J. Mol. Struct.* **1993**, 281, 91.

[167] Cervellati, R.; Esposti, A.D.; Lister, D.G.; Palmeri, P. *J. Mol. Struct.(Theochem)* **1985**, 122, 173.

[168] Nakagaki, R.; Aoyama, I.; Shimizu, K.; Akagi, M. *J. Phys. Org. Chem.* **1993**, 6, 261.

[169] Domenicano, A.; Schultz, G.; Hargittai, I.; Colapietro, M.; Portalone, G.; George, P.; Bock, C. W. *Struct. Chem.* **1990**, 1, 107.

[170] Borisenko, K. B.; Hargittai, I. *J Mol Struct* **1996**, 382, 171.

[171] Schaefer, T.; Penner, G.H.; Marat, K.; Sebastian, R. *Can. J. Chem* **1984**, 62, 2686.

[172] Anet, F.A.L.; Ghiaci, M. *J. Am. Chem. Soc.* **1983**, 101, 6857.

[173] Bolotina, N. B.; Kirschbaum, K.; Pinkerton, A. A. *Acta Cryst. Sect B. Struct Sci*, **2005**, 61, 577.

[174] Fedoroff, B. T. *Encyclopedia of Explosives and Related items*, Picatinny Arsenal, Dover, New Jersey **1960**, Vol.3, C616.

[175] Fedoroff, B. T. *Dictionary of Explosives,Ammunition and Weapons (German Section)*, Picatinny Arsenal Technical Report 2510, **1958**.

[176] Doll, D. W.; Hanks, J. M.; Allred, A. G.; Niles, J. B. *Melt-pourable explosive compositions, with reduced sensitivity and decreased toxicity for TNT substitutes*, US Patent No.2003005988, **2003**.

[177] Doll, D. W.; Hanks, J. M.; Allred, A. G.; Niles, J. B. *Reduced-sensitivity, melt-pourable explosives based on non-TNT nitroaromatic compounds as replacements for Tritonal*, US Patent No.2003140993, **2003**.

[178] Report on Shelf Life and the Determination of Stabilizer Concentrations in Double-Base Propellants by Army Missile Command Redstone Arsenal AL Propulsion Directorate, No. AMSMI-TR-RD-PR-90-9 XA-AMSMI **1990**, August 06.

[179] Cooper, P.W. *Explosives Engineering*, New York:Wiley-VCH, **1996**.

[180] Agrawal, J. P. *Organic Chemistry of Explosives*, **2007**, John Wiley & Sons, Ltd.

[181] Agrawal, J. P. *Prog. Energy. Combust. Sci*, **1998**, 24, 1.

[182] Damavarapu, R.; Surapaneni, C.R.; Gelber, N.; Duddu, G.R.; Zhang, M.; Dave, P.R. *Melt-cast explosive material*, US Patent No.7304164, **2001**.

[183] Phil, J.D.; Provatas, A. *Characterisation of 2,4-Dinitroanisole: An Ingredient for use in Low Sensitivity Melt Cast Formulations*, DSTO-TR-1904, **2006**.

[184] Monteil-Rivera, F.; Paquet, L.; Deschamps, S.; Balakrishnan, V.K.; Beaulieu, C.; Hawari, J. *J. Chromatogr.*, **2004**, 1025, 125.

[185] Lynch, J.C.; Myers, K.F.; Brannon, J.M.; Delfino, J.J. *J. Chem. Eng. Data*, **2001**, 46, 1549.

[186] Karakaya, P.; Sidhoum, M.; Christodoulatos, C.; Nicolich, S.; Balas, W. *J. Hazard. Mater.*, **2005**, 120, 183.

[187] Maksimov, Y.Y. *J. Phys. Chem.*, **1992**, 66, 280.

[188] Leggett, D.C. *J. Chromatogr.*, **1977**, 133, 83.

[189] Pella, P.A. *J. Chem. Thermodyn.*, **1977**, 9, 301.

[190] Dionee, B.C. *J. Energetic Mater.*, **1986**, 4, 447.

[191] Cundall, R.B.; Palmer, T.F.; Wood, C.E.C. *J. Chem. Soc., Faraday Trans.*, **1978**, 74, 1339.

[192] Lenchitz, C.; Velicky, R.W. *J. Chem. Eng. Data*, **1970**, 15, 401.

[193] Hansch, C.; Leo, A. *Substituent Constants for Correlation Analysis in Chemistry and Biology*, **1979**, John Wiley & Sons: New York, NY.

[194] Talmage, S.S.; Opresko, D.M.; Maxwell, C.J.; Welsh, C.J.; Cretella, F.M.; Reno, P.H.; Daniel, F.B. *Rev. Environ. Contam. Toxicol.*, **1999**, 161, 1.

[195] Ro, K.S.; Venugopal, A.; Adrian, D.D.; Constant, D.; Qaisi, K.; Valsaraj, K.T.; Thibodeaux, L.J.; Roy, D. *J. Chem. Eng. Data*, **1996**, 41, 758.

[196] Boddu, V.; Abburi, K.; Maloney, S.; Reddy, D. *J. Chem. Eng. Data*, **2008**, 53, 1120.

[197] Boddu, V.; Abburi, K.; Maloney, S.; Reddy, D. *J. Chem. Eng. Data*, **2008**, 155, 288.

[198] Kim, K.J.; Kim, M.J.; Lee, J.M.; Kim, S.H.; Kim, H.S.; Park, B.S. *J. Chem. Eng. Data*, **1998**, 43, 65.

[199] Martin, M. G.; Siepmann, J. I. *J. Phys. Chem. B*, Transferable potentials for phase equilibria. 1. United-atom description of n-alkanes **1998**, 102, 2569-2577.

[200] Wick, C. D.; Martin, M. G.; Siepmann, J. I. *J. Phys. Chem. B*, **2000**, 104, 8008.

[201] Stubbs, J. M.; Potoff, J. J.; Siepmann, J. I. *J. Phys. Chem. B*, **2004**, 108, 17596.

[202] Wick, C. D.; Stubbs, J. M.; Rai, N.; Siepmann, J. I. *J. Phys. Chem. B*, **2005**, 109, 18974.

[203] Rai, N.; Bhatt, D.; Siepmann, J. I.; Fried, L. E. *J. Chem. Phys.*, **2008**, 129, 194510.

[204] Rai, N.; Siepmann, J.I. *J. Chem. Phys. B*, **2007**, 111, 10790.

[205] Martin, M. G.; Siepmann, J. I. *J. Am. Chem. Soc.*, **1997**, 119, 8921.

[206] Lin, S-T.; Sandler, S. I. *Chem. Engg. Sci.*, **2002**, 57, 2727.

[207] Gao, J.; Kuczera, K.; Tidor, B.; Karplus, M. *Science*, **1989**, 244, 1069.

[208] Pearlman, D. A. *J. Phys. Chem.*, **1994**, 98, 14873.

[209] DeBolt, S. E.; Kollman, P. A. *J. Am. Chem. Soc.*, **1995**, 117, 5316.

[210] Beutler, T. C.; Mark, A. E.; van Schaik, R. C.; Gerber, P. R.; van Gunsteren, W. F. *Chem. Phys. Lett.*, **1994**, 222, 529.

[211] Pitera, J. W.; van Gunsteren, W. F. *Mol. Sim.*, **2002**, 28, 45.

[212] Essmann, U.; Perera, L.; Berkowitz, M. L. *J. Chem. Phys.*, **1995**, 103, 8577.

[213] Jorgensen, W. L.; Ravimohan, C. *J. Chem. Phys.*, **1985**, 83, 3050.

[214] Panagiotopoulos, A.Z. *Mol. Phys.*, **1987**, 61, 813.

[215] CRC Handbook of Chemistry and Physics, 89th Ed., **2008-2009**, CRC Press/Taylor and Francis, Boca Raton, FL.

[216] Schultz, T.W. *Chem. Res. Toxicol.*, **1999**, 12, 1262.

[217] Jimenez, P.; Roux, M. V.; Turrion, C. *J. Chem. Therm.*, **1987**, 19, 985.

[218] Wiley, R. H. *Pyrazoles, pyrazolines, pyrazolidines, indazoles and condensed rings*, **1967**, Interscience Publishers, New York.

[219] Hine, J.; Mookerjee, P. K. *J. Org. Chem.*, **1975**, 40, 292.

[220] Schultz, T. W.; Cajina-Quezada, M. *Arch. Environ. Contam. Toxicol.*, **1982**, 11, 353.

[221] *SIDS Initial Assessment Report*, **2003**, SIAM 17, Italy.

[222] Toghiani, R. K.; Toghiani, H.; Maloney, S. W.; Boddu, V. M. *Fluid Phase equilibria*, **2008**, 264, 86.

[223] Estimation Programs Interface Suite^{TM} for Microsoft Windows, v 4.00, US EPA, Washington DC, USA, **2009**.

[224] Meylan, W. M. and Howard, P. H. *J. Pharm. Sci.*, **1995**, 84, 83.

[225] Montgomery, J. H. *Groundwater chemicals desk reference*, **2000**, 3rd edn.,CRC Press.

[226] Gillett, J. W. *Environmental Toxicology and Chemistry* **1983**, 2, 463.

[227] Staudinger, J.; Roberts, P. *Crit. Rev. Environ. Sci. Tech.*, **1996**, 26, 205.

[228] Rowlinson, J. S.; Widom, B. *Molecular Theory of Capillarity*, **1982**, Clarendon Press, Oxford.

[229] Rowlinson, J. S.; Swinton, F. L. *Liquids and Liquid Mixtures*, **1982**, 3rd edn., Butterworth, London.

[230] Privman, V.; Trigg, G. L. *Encyclopedia of Applied Physics*, **1998**, vol.23, Wiley-VCH, Berlin, p.41.

[231] Stein, S. E.; Brown, R. L. *J. Chem. Inf. Comput.Sci.*, **1994**, 34, 581.

[232] Sorescu, D. C.; Rice, B. M.; Thompson, D. L. *J. Phys. Chem. B*, **1997**, 101, 798.

[233] Wang, J.; Wolf, R. M.; Caldwell, J. W.; Kollman, P. A.; Case, D. A. *J. Comput. Chem*, **2004**, 25, 1157.

[234] Agrawal, P. M.; Rice, B. M.; Zheng, L.; Thompson, D. L. *J. Phys. Chem. B*, **2006**, 110, 26185.

[235] Gee, R. H.; Roszak, S.; Balasubramanian, K.; Fried, L. E. *J. Chem. Phys.*, **2004**, 120, 7059.

[236] Peguin, R.P.S.; Kamath, G.; Potoff, J.J.; da Rocha, S.R.P. *J. Phys. Chem. B*, **2009**, 113, 178.

[237] Bruno, I. J.; Cole, J. C.; Edgington, P. R.; Kessler, M. K.; Macrae, C. F.; Mccabe, P.; Pearson, J.; Taylor, R. *Acta Cryst.*, **2002**, B58, 389.

[238] Cady, H.H.; Larson, A.C. *Acta Cryst.*, **1965**, 18, 485.

[239] Cho, J.R.; Kim, K.J.; Cho, S.G.; Kim, J.K. *J. Heterocycl. Chem.*, 39, 141.

[240] Sorescu, D.C.; Alavi, S.; Thompson, D.L. *Chemistry at Extreme Conditions*, **2005**, Elsevier, Amsterdam, The Netherlands.

[241] Luo, S.N.; Stratchan, A.; Swift, D.C. *J. Chem. Phys.*, **2004**, 120, 11640.

[242] Frenkel, D.; Smit, B. *Understanding Molecular Simulation: From Algorithms to Applications*, **1996**, Academic Press, Chestnut Hill, MA.

[243] Grochola, G.J. *J. Chem. Phys.*, **2004**, 120, 2122.

[244] Eike, D.M.; Brennecke, J.F.; Maginn, E.J. *J. Chem. Phys.*, **2005**, 122, 014115.

[245] Phillpot, S.R.; Lutsko, J.F.; Wolf, D.; Yip, S. *Phys. Rev. B*, **1989**, 40,2831.

[246] Solca, J.; dyson, A.J.; Steinebrunner, G.; Kirchner, B.; Huber, H. *J. Chem. Phys.*, **1998**, 108, 4107.

[247] Agrawal, P.M.; Rice, B.M.; Thompson, D.L. *J. Chem. Phys.*, **2003**, 118, 9680.

[248] Morris, J.R.; Wang, C.Z.; Ho, K.M.; Chan, C.T. *Phys. Rev. B*, **1994**, 49, 3109.

[249] Belonoshko, A.B.; Ahuja, R.; Johansson, B. *Phys. Rev. Lett.*, **2000**, 84, 3638.

[250] Watt, S. W.; Chisholm, J. A.; Jones, W.; Motherwell, S. *J. Chem. Phys.*, **2004**, 121, 9565.

[251] Morris, J. R.; Song, X. *J. Chem. Phys.*, **2002**, 116, 9352.

[252] Liu, Z. R.; Shao, Y. H.; Yin, C. M.; Kong, Y. H. *Thermochim. Acta*, **1995**, 250, 65.

[253] Fernández, R.G.; Abascal, J.L.F.; Vega, C. *J. Chem. Phys.*, **2006**, 124, 144506.

[254] MSDS for N-methyl-4-nitroaniline, http://ptcl.chem.ox.ac.uk/MSDS/MEN/N-methyl-4-nitroaniline.html.

[255] Cuisset, A.; Mouret, G.; Pirali, O.; Roy, P.; Cazier, F.; Nouali, H.; Demaison, J.; *J. Phys. Chem. B* **2008**, 112, 12516.

[256] Tevault, D. E.; Buchanan, J. H.; Buettner, L. C.; *Int. J. Thermophys.* **2006**, 27, 486.

[257] Butrow, A. B.; Buchanan, J. H.; Tevault, D. E.; *J. Chem. Eng. Data* **2009**, submitted.

[258] Belkin, F.; Brown, Jr., H. A.; *Vapor Pressure Measurements of Some Chemical Agents using Differential Thermal Analysis. Part III* **1975**, EC-TR-75032; Edgewood Arsenal: Edgewood, MD, UNCLASSIFIED Report (AD-A010 666).

[259] Buchanan, J. H.; Sumpter, K. B.; Abercrombie, P. L.; Tevault, D. E.; *Vapor Pressure of GB* **2009**, ECBC-TR-xyz; Edgewood, MD, UNCLASSIFIED Report (HP-5890 GC).

[260] Ault, B. S.; Balboa, A.; Tevault, D.; Hurley, M.; *J. Phys. Chem. A* **2004**, 108, 10094.

[261] Kaczmarek, A.; *Struc. Chem.* **2004**, 15, 517.

[262] Majumdar, D.; Roszak, S.; Leszczynski, J.; *Mol. Phys.* **2007**, 105, 2551.

[263] Vishnyakov, A.; Neimark, A.V. *J. Phys. Chem. A*, **2004**, 108, 1435.

[264] Kosolapoff, G.M. *J. Chem. Soc.*, **1955**, 2964.

[265] D.E. Tevault, J. Keller, J. Parson. ERDEC. U.S Army Technical Report.

[266] Kosolapoff, G.M. *J. Chem. Soc.*, **1954**, 3222.

[267] Kosolapoff, G.M. *J. Chem. Soc.* **1954**, 76, 615.

[268] Chandrasekhar, J.; Spellmeyer, D.; Jorgensen, W.L.; *J. Am. Chem. Soc*, **1984**, 106, 903.

[269] Berendsen, H.J.C.; Grigera, J.R.; Straatsma, T.P. *J. Phys. Chem.*, **1987**, 91, 6269.

[270] Ault, B.S.; Balboa, A.; Tevault, D.; Hurley, M. *J. Phys. Chem. A*, **2004**, 108, 10094.

[271] Cuisset, A.; Mouret, G.; Pirali, O.; Roy, P.; Cazier, F.; Nouali, H.; Demaison, J. *J. Phys. Chem. B*, **2008**, 112, 12516.

[272] Suenram, R.D.; Lovas, F.J.; Plusquellic, D.F.; Lesarri, A.; Kawashima, Y.; Jensen, J.O.; Samuels, A.C. *J. Mol. Spectrosc.*, **2002**, 211, 110.

[273] kaczmarek, A.; Gorb, L.; Sadlej, A.J.; Leszczynski, J. *J. Struct. Chem.*, **2004**, 15, 517.

[274] Stewart, E.L.; Norman, N.N,; Allinger, N.L.; Bowen, J.P. *J. Org. Chem.*, **1997**, 62, 5198.

[275] Muller, E.A.; Rull, L.F.; Gubbins, K.E. *J. Phys. Chem.*, **1996**, 100, 1189.

[276] Wood, W.W. *J. Chem. Phys.*, **1968**, 415, 48

[277] McDonald, I.R. *Mol. Phys.* **1972**, 41, 23.

[278] Martin, M. G.; http://towhee.sourceforge.net/

[279] D.E. Tevault, J. Keller, J. Parson. ERDEC. U.S Army Technical Report.

[280] Langford, R. E. *Introduction to Weapons of Mass Destruction- Radiological, Chemical and Biological* **2004**, John Wiley & Sons, New Jersey.

[281] Evans, R.; Marconi, U.M.B.; Tarazona, P. *J. Chem. Soc. Faraday Trans. 2*, **1986**, 82, 1763.

[282] Peterson, B.K.; Gubbins, K.E. *Mol. Phys.*, **1987**, 62, 215.

[283] Wujcik, W.J.; Lowe, W.L.; Marks, P.J. *Environ. Progr.*, **1992**, 11, 178.

[284] Freedman, D.L.; Stanley, R.S.; Schulz, R.J. *J. Hazard. Mater.*, **1996**, 49, 1.

[285] Hundal, L.S.; Singh, J.; Bier, E.L.; Shea, P.J.; Comfort, S.D. *Environ. Pollut.*, **1997**, 97, 55.

[286] Raafat, A.; Aydin, A. *Wat. Res.*, **1999**, 33, 2021.

[287] Medina, V.F.; Larson, S.L.; Bergstedt, A.E.; Mccutcheon, S.C. *Wat. Res.*, **2000**, 713.

[288] Rajagopal, C.; Kapoor, J.C. *J. Hazard. Mater.*, **2001**, 87, 73.

[289] Rodgers, J.D.; Bruce, N.J. *Wat. Res.*, **2001**, 35, 2101.

[290] Maloney, S.W.; Adrian, N.R.; Hickey, R.F.; Heine, R.L. *J. Hazard. Mater.*, **2002**, 92, 77.

[291] Doppalapudi, R.B.; Sorial, R.B.; Maloney, S.W. *Environ. Engng Eci.*, **2000**, 19, 115.

[292] Liou, M.; Lu, M.; Chen, J. *Wat. Res.*, **2003**, 37, 3172.

[293] Marinovic, V.; Ristic, M.; Dostanic, M. *J. Hazard. Mater.*, **2005**, 117, 121.

[294] Lee, J.; Yang, T.; Shim, W.; Kwon, T.; Moon, I.L. *J. Hazard. Mater.*, **2007**, 141, 185.

[295] Davis, J.L.; Brooks, M.C.; Larson, S.L.; Nester, C.C.; Field, D.R. *Soil Sediment Contam.*, **2006**, 15, 565.

[296] Boddu, V.M.; Abburi, K.; Fredricksen, A.J.; Maloney, S.W.; Damavarapu, R. *Environ. Tech.*, **2009**, 30, 173.

[297] Chiou, C.T.; Free, V.H.; Schmedding, D.W.; Kohnert, R.L. *Environ. Sci. Tech.*, **1977**, 11, 475.

ABSTRACT

MOLECULAR MODELING OF ENERGETIC MATERIALS AND CHEMICAL WARFARE AGENTS

by

NANDHINI SOKKALINGAM

AUGUST 2010

Advisor: Dr. Jeffrey J. Potoff

Major: Chemical Engineering

Degree: Doctor of Philosophy

Contamination of military sites by energetic materials and chemical warfare agents is a growing problem. To avoid health hazards associated with these compounds, it is necessary to decontaminate or remediate the contaminated sites. Effective decontamination requires knowledge of environmental fate of contaminants and the appropriate remediation methodologies. While the fate of chemical warfare agents are well studied, the impact of certain energetic materials in the environment is relatively unknown. So the current focus is determining environmental fate of Insensitive Munitions (IM) which are energetic materials that have low shock sensitivity and high thermal stability and developing detection schemes for identifying chemical warfare agents. For energetic materials, the environmental fate can be assessed by determining the partition coefficients, especially the octanol-water and Henry's law constants (air-water partition coefficient). For chemical warfare agents, the most important criteria for developing sensors is the detection selectivity. Carbon adsorbents are a simple and effective way of increasing the sensor selectivity for the contaminants by concentration or prefiltration through physical adsorption. So it is essential to study the

adsorption behavior of the contaminants in carbon slit pores as a preliminary step to the sensing process.

In this work, molecular modeling or simulation is proposed as a theoretical tool to determine thermophysical properties that aid in understanding how certain energetic materials behave in the environment and developing techniques for detecting chemical warfare agents. Molecular modeling is a promising alternative to experiments due to the hazardous nature of these compounds and the long experimental time scales involved in their testing. Molecular models or force fields are developed to predict various thermophysical properties. For energetic materials, atomistic molecular dynamics simulations are used to predict properties such as octanol-water partition coefficients, Henry's law constant and also critical parameters, vapor pressure, boiling points, lattice parameters, crystal density, melting points. For chemical warfare agents, the developed force fields are used to determine their phase coexistence properties, vapor pressures, critical parameters, pure and water-compound mixture adsorption isotherms over carbon slit pore using atomistic monte carlo simulations.

The thermophysical properties predicted for both energetic materials and chemical warfare agents are in good agreement with the available experimental data. The partition coefficients determined for the energetic materials of interest categorize them as ground water contaminants. The simulation methods presented in this work can be used as preliminary evaluation, screening or testing routines before any major experimental process is undergone saving a considerable amount of time and cost.

AUTOBIOGRAPHICAL STATEMENT

I was born on May 10, 1982 in the state of Tamilnadu, India. I studied at the Central Electrochemical Research Institute (CECRI) where I earned a B.Tech (Bachelors in Technology) in Chemical & Electrochemical Engineering in 2003. Then I started working towards my M.S and Ph.D in Chemical Engineering at Wayne State University in 2004.